APPLICATION OF SINGLE OPTICALLY HEATED GOLD NANOPARTICLES TO SENSING AND ACTUATION

Von der Fakultät für Physik und Geowissenschaften

der Universität Leipzig

genehmigte

DISSERTATION

zur Erlangung des akademischen Grades

doctor rerum naturalium

Dr. rer. nat.

vorgelegt

von André Heber, M.Sc.

geboren am 26.06.1987 in Berlin

Gutachter:
Prof. Dr. Frank Cichos, Universität Leipzig
Prof. Dr. Michel A. G. J. Orrit, University Leiden

Tag der Verleihung: 27.11.2017

Contents

Bibliographic description

Heber, André
Application of Single Optically Heated Gold Nanoparticles to Sensing and Actuation
Universität Leipzig, Dissertation
115 pages, 180 references, 29 figures, 2 tables, 4 appendices

Abstract

This dissertation demonstrates the use of individual optically heated gold nanoparticles as sensors for investigations of heat transport and intensity modulation of light. The experiments employ the photothermal effect, which allows the selective detection and investigation of individual absorbers. The photothermal contrast is based on absorbing particles that are optically excited and relax via nonradiative processes. The absorbers act as nanosources of heat. The local temperature elevation leads to a local refractive index change due to thermal expansion which then acts as a lens. This thermal lens alters the propagation of a second non-absorbed beam of light. As the refractive index change with temperature is minuscule, the transmission changes of the detection are tiny as well. The photothermal signal is amplified by the use of a modulated detection scheme which enables the methods high sensitivity and provides a time scale for the measurement of thermal transport.

The heating laser beam is intensity-modulated and thereby produces a small modulation of the beam waist of the detection laser beam and thus the transmitted power through an aperture. This modulation amplitude and phase are detected by a lock-in amplifier. Amplitude and phase depend on the modulation frequency and the thermal diffusivity of the material surrounding the nanoparticle. The frequency-resolved measurement of the two observables and their modeling using a generalized Lorenz–Mie theory allows the measurement of thermal diffusivities. In the second variant, the spread of heat into space is observed. A nanoparticle is optically heated, and the extended thermal lens is characterized by the deflection of a second laser beam. The deflection signal is modeled using ray optics to determine the thermal diffusivity of the material surrounding the nanoparticle.

In a further experiment, the great potential of optically heated nanoparticles is demonstrated. Individual gold nanoparticles are embedded in a thin nematic liquid-crystal layer acting as a half-wave plate. The gold particles are optically heated. They control the transmission of a detection laser set up in polarization contrast. The intensity of the detection beam is modulated by up to 100 %.

Bibliographische Beschreibung

Heber, André
Application of Single Optically Heated Gold Nanoparticles to Sensing and Actuation
Universität Leipzig, Dissertation
115 Seiten, 180 Literaturangaben, 29 Abbildungen, 2 Tabellen, 4 Anhänge

Referat
Diese Dissertation demonstriert die Nutzung von einzelnen optisch geheizten Goldnanopartikeln als Sensoren für die Untersuchung von Wärmetransport und als Intensitätsmodulator für Licht. Die beschriebenen Experimente basieren auf der photothermischen Mikroskopie, die die selektive Abbildung and Untersuchung von einzelnen absorbierenden Objekten ermöglicht. Goldnanopartikel werden optisch angeregt. Die Relaxation erfolgt durch nichtstrahlende Prozesse, die zu einer lokalen Erhöhung der Temperatur führen. Die Erwärmung führt zu einer Verringerung der Brechzahl, die als thermische Linse wirkt und dadurch die Ausbreitung eines zweiten nicht absorbierten Lichtstrahls verändert. Da die thermische Änderung der Brechzahl sehr gering ist, wird das photothermische Signal durch das moduliertes Detektionsverfahren verstärkt.

Der Heizlaserstrahl wird intensitätsmoduliert und erzeugt dadurch eine geringe Modulation der Strahlbreite des Detektionslaserstahls. Damit verändert sich die Leistung, die durch eine Blende transmittiert wird. Diese Modulationsamplitude and Phaseverzögerung werden mittels eines phasenempfindlichen Gleichrichters detektiert. Amplitude und Phase hängen von Modulationsfrequenz und thermischer Diffusivität ab. Die frequenzaufgelöste Messung der beiden Größen und deren Modellierung mittels einer verallgemeinerten Lorenz–Mie Theorie ermöglicht die Messung von der thermischen Diffusivität des Mediums, das das Goldnanopartikel umgibt. In der zweiten Variante wird die Ausbreitung der Wärme beobachtet. Ein Nanopartikel wird optisch geheizt und die ausgedehnte thermische Linse wird mit Hilfe der Ablenkung eines zweiten Laserstrahls vermessen. Das Ablenkungssignal wird mittels eines strahlenoptischen Models berechnet, um die thermische Diffusivität des Materials zu bestimmen, das das Nanopartikel umgibt.

In einem weiteren Experiment wird das große Potential von optisch geheizten Nanopartikeln verdeutlicht. Einzelne Goldnanopartikel werden in eine dünne nematische Flüssigkristallschicht eingebettet, deren Dicke darauf abgestimmt ist, dass die Schicht eine $\lambda/2$-Platte darstellt. Die Goldnanopartikel werden optisch geheizt und steuern damit den Phasenübergang von der nematischen zur isotropen Phase. Damit wird die Transmission eines zweiten Laserstrahls im Polarisationskontrast geändert. Mit Hilfe dieser Anordnung kann die Intensität eines Lichtstrahls um bis zu 100 % moduliert werden.

Abbreviations

5CB	4-Cyano-4’-pentylbiphenyl
8CB	4-Cyano-4’-octylbiphenyl
APTMS	(3-Aminopropyl)trimethoxysilane
CCD	charge-coupled device
DDA	discrete dipole approximation
e.g.	exempli gratia – for example
eq.	equation
et al.	et alia – and others
FDTD	finite difference time domain
fig.	figure
GLMT	generalized Lorenz–Mie theory
i.e.	id est – that is
iScat	Interference scattering
PDMS	Polydimethylsiloxane
PVA	polyvinyl alcohol
ref.	reference
SMS	single molecule spectroscopy
TL	thermal lens

Chapter 1

Introduction

Thermal energy can be transferred by thermal convection, thermal radiation, and thermal conduction. Convection is the transport of heat due to the movement of matter. On macroscopic length scales, heat is applied whenever large amounts of heat shall be transferred. In this case, it is the most efficient mode of heat transfer. On the nanoscale, the contribution of convection to heat transfer is negligible as fluid convections are immediately damped due to the dominant role of viscous forces.[1] Thermal radiation between two bodies is the transfer of heat due to photons, which is usually important in the vacuum only as the heat conduction and convection are much more efficient at ambient temperatures. However, thermal radiation is significantly enhanced once the particle separation decreases below the thermal wavelength. Then, photons can tunnel between two bodies.[2] Last but not least, there is heat conduction which is the transport of heat inside a material mostly due to mechanic vibrations of molecules or atoms and also due to the movement of free electrons.[3] This thesis focuses on heat conduction.

During the transfer of the thermal energy from the hot segment of a body to the cold one, the heat carriers are scattered multiple times making heat conduction a diffusive process. Therefore, the rate at which the thermal energy is transported is proportional to the temperature gradient. The thermal conductivity κ is the proportionality constant. This dependence is also known as Fourier's law and has been validated for numerous systems. Fourier's law becomes invalid once the mean free path of the collective lattice vibrations called phonons is smaller than the dimension of the material.[4] Using far-field optical control, heat conduction is studied for macroscopic samples,[5] at interfaces,[6] or for particle ensembles.[7–9] Thermal transport measurements in single nanostructures typically require physical contact with the sample. Examples are scanning thermal microscopy,[10,11] and heat transfer between two heat reservoirs.[12] Thermal transport measurements are not routinely done with methods that study thermal transport with single particles using far-field optical readout. There are various scientific questions which cannot be addressed thoroughly with the existing techniques including thermal transport in cells and polymers.

Temperature measurements in cells gave temperature elevations that exceed theoretical estimates by orders of magnitude.[13,14] These measurements are unlikely to be artifacts due to the wide validation by many research groups using different methods including quantum dots,[13] fluorophores,[15] or thermocouples.[16] Studying thermal transport in cells could provide an answer to the asked question. Cells are highly heterogeneous. Therefore, thermal transport inside cells is expected to be heterogeneous. The study of thermal transport in cells requires the localized resolution of thermal transport phenomena using far-field optical readout to disturb the cell as little as possible.

The heat conduction in polymers depends strongly on their morphology. In bulk, polymers consist of randomly entangled macromolecules. The thermal conductivity along the chain is very large and supposedly orders of magnitude larger than the bulk one.[17] Along the chain, the atoms are strongly coupled and can transfer thermal energy very efficiently. The coupling between different chains and chain segments is much weaker leading to a lower thermal conductivity. The thermal conductivity of polyethylene can be as small as $0.31\,\mathrm{W\,m^{-1}\,K^{-1}}$ in the bulk[18] or as large as $104\,\mathrm{W\,m^{-1}\,K^{-1}}$ for drawn polymer fibers.[19] As the thermal conductivity shows such strong dependencies on the morphology,[20] which might change within the sample,[21] local single particle-resolved thermal transport measurements are required to obtain a throughout understanding of the underlying microscopic mechanisms. An additional question is the thermal transport of elastic polymers under mechanical load.

This topic is still largely unexplored experimentally due to limitations of the existing measurement schemes. Molecular dynamic simulations predict that the thermal conduction will increase with the strain along the direction of the elongation.[22,23] Local thermal transport studies in spider silk could help to uncover its peculiar mechanic[24] and phonon properties[25] which are based on its complex nanostructure.

In this thesis, the aim is to develop a technique that can study thermal transport on the single particle level, has far-field optical readout, and requires only small temperature increases for the measurement. Single gold nanoparticles are used. They are optically excited at their plasmon resonance to induce local temperature elevations. The nanoparticle relaxes via nonradiative pathways increasing its temperature. This heat is released into the environment of the nanoparticle creating a localized temperature profile. The local temperature increase results in a change of the refractive index due to thermal expansion. The local refractive index change acts as a thermal lens and is detected by a second non-absorbed laser beam and is used as the sensor for the temperature measurement. The thermal lens changes the divergence of the focused detection laser beam, which results in a transmission change through an aperture.[26–28] If the detection laser passes the thermal lens offset to the optical axis the detection laser beam is deflected, which can be detected by a quadrant photodiode.[29,30] Photothermal lensing is the mechanism typically employed in single particle photothermal microscopy. It is already a well-established technique for the study of absorption cross sections of single molecules,[31,32] quantum dots,[33] carbon nanotubes,[34] metallic nanoparticles[26] and nanostructures.[35] It also allows the measurement of absorption spectra.[33,36–39] Like fluorophores, gold nanoparticles can be used as contrast agents to label proteins[40,41] and track their movement in cells.[42] Compared to fluorophores, plasmonic nanoparticles neither bleach nor blink.[43] Photothermal correlation spectroscopy is the counterpart of fluorescence correlation spectroscopy and allows studying dynamics of gold nanoparticles in nonequilibrium.[44–48]

The photothermal signal Φ is the transmission change upon optical heating and is proportional to the temperature elevation at the nanoparticle's surface $\Delta T = \frac{\sigma_{\mathrm{abs}} I}{4\pi\kappa R}$ depending on the intensity of the heating laser I, the absorption cross section σ_{abs}, the thermal conductivity κ, and the particle radius R. However, the measurement of the thermal conductivity requires the exact value of σ_{abs} which is proportional to R^3. Gold nanoparticles usually have size dispersions of about 10 %[49,50] leading to variations in the absorption cross section of 30 %. This uncertainty would limit the accuracy of the thermal conductivity measurement using a single nanoparticle. Nevertheless, this measurement has been used to quantify the effective thermal conductivity around a single heated nanoparticle positioned at interfaces.[51,52] However, this approach requires large temperature increases at the particle surface and the measured thermal conductivities have large uncertainties.

If the temperature profile is modulated, one can also measure the thermal diffusivity $\alpha = \kappa / c_{\mathrm{p}}\rho$, which is the quotient of thermal conductivity and heat capacity at constant pressure c_{p} times density ρ. While κ quantifies the rate of thermal energy transport, α is the rate at which temperature profiles are built up. In photothermal microscopy, a modulated detection scheme is routinely utilized. The repeated transmission measurement while the nanoparticle is heated and not heated is the basis of the sensitivity of photothermal microscopy and the time scale for the measurement of thermal transport. The intensity of the heating laser is harmonically modulated leading to a modulation of the refractive index field, which is detected by a second non-absorbed laser beam. As the frequency of the modulation is known, and the modulation amplitude of the transmission is very small, a lock-in amplifier processes the signal. It measures the modulation amplitude and phase delay between optical heating and the detection signal.

The amplitude of the photothermal signal is known to depend on the modulation frequency and the thermal diffusivity. At low modulation frequencies the temperature profile is completely modulated, and at high ones, the modulation is diminished. Therefore, the amplitude of the photothermal signal is found to decrease with the modulation frequency.[43,53] The previous approaches to extract thermal diffusivities in the vicinity of the nanoparticle from the frequency dependence of the photothermal lensing signal have yielded unrealistic results due to a simplified model.[53,54]

As already outlined, single particle photothermal microscopy is chosen as it is sensitive to the thermal diffusivity in the vicinity of an absorber. The nanoparticle acts as a heat source, and the local refractive index change is the temperature sensor. The thermal diffusivity measurement is performed in the frequency domain where the heating laser is intensity-modulated and the detection laser senses fluctuations at that particular frequency. A lock-in amplifier measures amplitude and phase delay of the intensity modulated detection signal. Single particle thermal transport measurements are demonstrated for two different variants of single particle photothermal microscopy. The first implementation utilizes the frequency-dependent photothermal lensing signal. The photothermal lensing signal has an amplitude that drops with the modulation frequency and a phase delay that increases. The phase delay accounts for the fact that the maximal temperature elevation and maximal heating intensity are not in phase at high modulation frequencies. The optically detected phase delay is an average of the phase delays induced by thermal transport. The averaging is caused by the diffraction limited detection laser which is much larger than the nanoparticle. To extract the thermal diffusivity from this measurement, the interaction between the focused detection laser and the gold nanoparticle surrounded by the time-dependent refractive index field is calculated by a generalized Lorenz–Mie theory.[26] The second implementation is based on single particle photothermal deflection where the heating laser remains focused on the nanoparticle. The detection laser is scanned to probe the extended thermal lens. The thermal diffusivity is measured by following the propagation of heat away from the particle. The deflection intensity decreases with distance and the phase delay increases linearly for large distances. A simple ray optics model based on Fermat's principle is used to extract the thermal diffusivity.

Finally, photothermal effects are studied in the liquid crystal 4-Cyano-4'-pentylbiphenyl (5CB). At room temperature, 5CB is a birefringent material that changes the polarization of transmitted light. The liquid crystal also features a nematic to isotropic phase transition where the optical anisotropy is lost. To enhance the signal by using the phase transition and the birefringence of the liquid crystal, a half-wave plate is produced from the liquid crystal, and gold nanoparticles are embedded. Upon optical heating of the nanoparticle the phase composition is changed, which affects the polarization of the transmitted light. The detection laser is set up in a polarization contrast configuration. In that manner, local phase transitions induced by a single optically heated gold nanoparticle can be detected. Using this setup the detection laser can be modulated by 100 % making the gold nanoparticle a simple yet efficient intensity modulator for light.

The manuscript is arranged in the following way. Chapter 2 discusses physical concepts required for the interpretation of the photothermal microscopy measurements, gives details on the state-of-the-art in thermal transport measurements and photothermal microscopy. Chapter 3 gives detailed information required for the execution and evaluation of the experiments. Chapter 4 presents and discusses the experimental investigations. In particular, the applicability of photothermal microscopy to the study of thermal transport is demonstrated and examined in detail. The chapter closes by showing an all-optical modulation scheme using a single gold nanoparticle embedded into a liquid crystal matrix. Chapter 5 summarizes the manuscript and gives perspectives for the application of single gold nanoparticles to sensing of thermal transport and photothermal microscopy in liquid crystals.

Chapter 2

Theoretical Background

This chapter will shortly establish the theoretical background required for the understanding of the experimental results and the simulations conducted during this thesis. First, the interactions between metallic nanoparticles and light are discussed. Then, discussions on thermal transport and liquid crystals follow. This chapter closes with an overview of methods employed for the photothermal detection of single absorbing nano-objects.

2.1 Interactions Between Metallic Nanoparticles and Light

The most elementary interaction between light and matter is the polarization of a single hydrogen atom by a plane wave. The atom consists of a positively charged proton and a negatively charged electron. The incident electromagnetic radiation polarizes the atom and results in an oscillation of the dipole at the frequency of the light wave. The electric dipole reradiates the electromagnetic energy as a Hertzian dipole. This process is also known as scattering. The superposition of many scattering atoms leads to the refractive index. For many materials like glasses, polymers or liquids scattering is the dominant interaction with visible light. In materials, scattering is visible whenever there is a mismatch in the refractive index, for example at interfaces between different materials.

Metallic nanostructures interact much stronger with visible light, which is rooted in their atomic structure. In a first approximation, metals are treated as a free electron gas that moves freely against the positively charged metal ion core. This simple model explains many phenomena observed for metal nanoparticles interacting with light. For metal nanostructures, absorption and scattering processes are significant at the same time. Absorption and scattering are quantified by the respective cross sections for absorption σ_{abs} and scattering σ_{sca}. The absorption cross section σ_{abs} is of particular interest as it determines the strength of the photothermal effect. Using the Rayleigh approximation, the interaction cross sections are derived for a spherical nanoparticle interacting with a plane wave where the particle radius is smaller than the wavelength. This section closes with considerations regarding more general incident electromagnetic fields and particle shapes.

2.1.1 Dielectric Function of Metals

The simplest treatment of metals is the free electron gas also called Drude model.[55] The electrons are assumed to move freely against the positively charged core metal ions that are fixed in space and form the backbone of the metal. An individual electron with the mass m_{e} and charge e is accelerated by the time-harmonic electric field $\mathbf{E}(t) = \mathbf{E}_0 \exp(i\omega t)$ at the angular frequency ω,

$$m_{\text{e}}\frac{\partial^2}{\partial t^2}\mathbf{r} + m_{\text{e}}\Gamma\frac{\partial}{\partial t}\mathbf{r} = -e\mathbf{E}(t), \tag{2.1}$$

where $\mathbf{r}$ is the position vector of the electron and E_0 the electric field amplitude. The motion of the electron is damped depending on the collision rate Γ. The solution to eq. 2.1 gives the driving of a single free electron. Assuming that all electrons are driven independently by the external field, the polarization $\mathbf{P} = -Ne\mathbf{r}$ of the metal becomes[55]

$$\mathbf{P} = -\frac{Ne^2}{m(\omega^2 + i\Gamma\omega)}\mathbf{E}, \tag{2.2}$$

where N is the free electron density. On the other hand, the polarization is connected to the dielectric displacement $\mathbf{D} = \varepsilon_0 \varepsilon \mathbf{E} = \varepsilon_0 (\mathbf{E} + \mathbf{P})$ via the dielectric function ε. Including the plasma frequency $\omega_\mathrm{p} = \frac{Ne^2}{\varepsilon_0 m_e}$ the dielectric function of the free electron gas from eq. 2.2 is derived as

$$\varepsilon(\omega) = 1 - \frac{\omega_\mathrm{p}^2}{\omega^2 - i\Gamma\omega} = 1 - \frac{\omega_\mathrm{p}}{\omega + \Gamma^2} + i\frac{\omega_\mathrm{p}^2}{\omega(\omega^2 + \Gamma^2)}. \tag{2.3}$$

If the damping constant Γ is small with respect to plasma ω_p and driving frequency ω, the dielectric function is well approximated by

$$\varepsilon(\omega) = 1 - \frac{\omega_\mathrm{p}}{\omega} + i\frac{\omega_\mathrm{p}^2}{\omega^3}. \tag{2.4}$$

For the remainder of the section, the focus is on the dielectric function of gold as the used nanoparticles consist of this material. In the long wavelength limit of the electromagnetic radiation the free electron gas eq. 2.3 approximates the dielectric function of gold very well. Starting at 750 nm the agreement between experimental data and equation 2.3 deteriorates (see fig. 2.1). In the optical wavelength regime, interband transitions from the d-electrons to the conduction band contribute significantly to the dielectric function. These contributions can be included by solving the Hamiltonian for interactions between bound electrons and photons.[56] Alternatively, the addition of a Lorentz oscillator to the dielectric function can phenomenologically capture the contribution of the bound electrons,[57]

$$\varepsilon_\mathrm{DL}(\omega) = \varepsilon_\infty - \frac{\omega_\mathrm{p}^2}{\omega^2 + i\Gamma\omega} - \frac{\Delta\varepsilon\, \Omega_\mathrm{L}^2}{(\omega^2 - \Omega_\mathrm{L}) + i\Gamma_\mathrm{L}\omega}, \tag{2.5}$$

where $\Delta\varepsilon$ is a weighting factor, Ω_L the oscillator strength and Γ_L the spectral width. The dielectric function at infinite frequency ε_∞ differs from 1 as the backbone has an electric susceptibility as well. The Drude–Lorentz model approximates the dielectric function of gold up to 500 nm fairly well. In the wavelength regime between 300 nm and 500 nm a single Lorentz oscillator describes the dielectric function of gold insufficiently (see fig. 2.1).

To calculate the interaction cross sections between light and the metallic nanoparticle, a model for the dielectric function as described above or an experimentally determined dielectric function can be used. To model and understand experiments in plasmonics the accurate knowledge of the dielectric function is of high significance. The most frequently used dielectric function is the one measured by Johnson and Christy (see fig. 2.1).[59] Their data are obtained from transmission and reflection measurements at the normal and p-polarized incidence at 60° of thin gold films. Over the years large variations of the dielectric function of gold have been observed. The deviations have been attributed to the sample preparation which may result in differences of the surface roughness. This standard interpretation was recently challenged by Olmon et alia.[58] They investigated the dielectric function of gold samples significantly exceeding the skin depth using ellipsometry (see fig. 2.1). The gold films were a single crystalline gold crystal, an evaporated and a template-stripped gold film which has a reduced surface roughness. The latter dielectric function is shown in fig. 2.1. The result of the ellipsometry measurement is that the dielectric functions of different samples deviate less than the dielectric functions reported in the literature. Possible reasons for deviations between

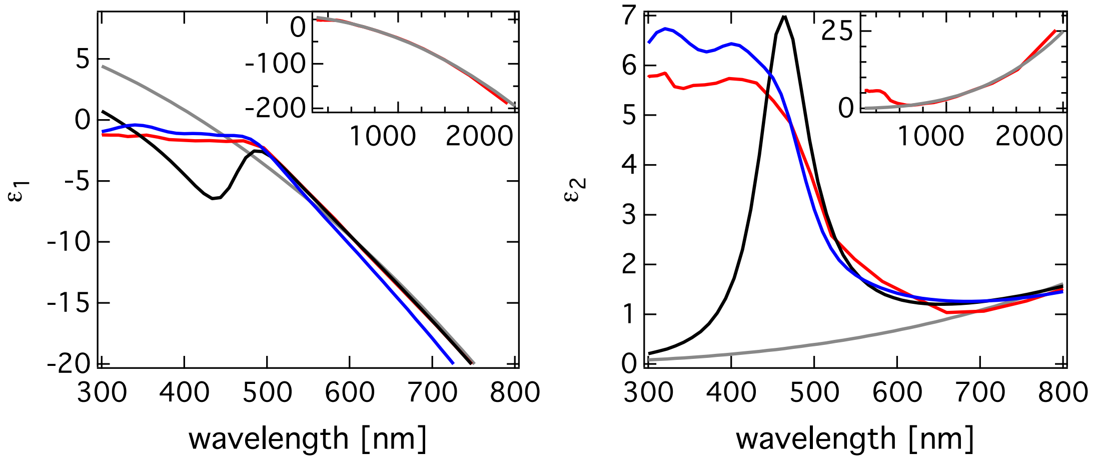

Figure 2.1: (left) Real part of the dielectric function and (right) imaginary part of the dielectric function. Drude model (gray), Drude–Lorentz model (black); parameters taken from ref. [57]. Experimental dielectric function of a template-stripped gold film from Olmon et al.[58] (blue), from Johnson and Christy[59] (red).

separate publications are systematic errors caused by the instrumentation, coarse assumption for the data analysis, and are not rooted in the sample preparation.[58]

If at least one dimension of the gold structure becomes smaller than the mean free path of the free electrons the dielectric function becomes size-dependent.[33,60–62] The mean free path of the electrons in gold is about 25 nm. In bulk gold the electrons are subject to the damping at the rate $\Gamma_{\text{bulk}} = 1.1 \cdot 10^{-14}\,\text{Hz}$. If the mean free path of the electron becomes smaller than the dimension of the nanostructure, the electrons are scattered at the interface to the environment. For a spherical particle the damping rate Γ_{NP} becomes[60]

$$\Gamma_{\text{NP}}(R) = \Gamma + C\frac{v_{\text{F}}}{R}, \tag{2.6}$$

where v_{F} is the Fermi velocity and C the efficiency of the surface scattering. The increase of the damping rate reduces the coherence time of the electron oscillations. Size effects become significant for nanoparticles with radii of less than 5 nm broadening and reducing the plasmon resonance.[36,60,63]

2.1.2 The Rayleigh Approximation

Using electrostatics the polarizability a of a sphere with the radius R gives[55]

$$a = 4\pi\varepsilon_0 R^3 \frac{\varepsilon - \varepsilon_{\text{m}}}{\varepsilon + 2\varepsilon_{\text{m}}}. \tag{2.7}$$

Herein, ε is the dielectric function of the sphere's material, ε_m the dielectric constant of the surrounding medium and ε_0 the dielectric permittivity of the vacuum. The polarizability of the sphere is proportional to its volume. In metals, the positively charged core ions are fixed in space whereas the conduction band electrons move freely and follow the external field. Therefore, metals shield their internal volume from the external field. In the static regime $\omega = 0$ the internal field becomes $E_{\text{i}} = 0$ implying a dielectric constant of $\varepsilon = -\infty$ giving the static polarizability $a = 4\pi\varepsilon_0 R^3$ of a metallic sphere.

If the electromagnetic field is approximately constant over the extent of the sphere, eq. 2.7 is also applicable if the electric field changes over time, also called quasi-static or Rayleigh approximation. The dielectric function $\varepsilon(\omega) = \varepsilon_1(\omega) + i\varepsilon_2(\omega)$ becomes frequency-dependent as the electrons do not follow changes of the electric field instantly. From eq. 2.7 it becomes evident that the polarizability becomes maximal if $\varepsilon_1(\omega) = -2\varepsilon_\mathrm{m}$ which can be fulfilled for metals. The so-called plasmon resonance is observed if $\varepsilon_2(\omega)$ is small and the denominator is minimized.

In the following the interaction cross sections between a plane wave with the wavelength λ and a spherical particle much smaller than λ are derived. This case is equivalent to a dipole.[64] The dipole moment $\mathbf{p} = a\varepsilon_m\mathbf{E}_\mathrm{inc}$ is located at $z = 0$ and irradiated by a plane wave $\mathbf{E}_\mathrm{inc} = E_\mathrm{inc}e^{i(kz-\omega t)}\mathbf{e}_\mathrm{x}$. E_inc is the electric field amplitude, $k = n\omega/\lambda$ the wavenumber, ω the angular frequency of the plane wave, n the refractive index. Using Poynting's theorem the power extinct by a dipole P_ext is calculated,[65]

$$P_\mathrm{ext} = \frac{1}{2}\mathrm{Re}\left(\int_V \mathbf{J}^* \cdot \boldsymbol{\varepsilon}_\mathbf{m}\mathbf{E}_\mathbf{inc}\mathbf{dV}\right) = \frac{1}{2}\varepsilon_m E_\mathrm{inc}\,\mathrm{Re}\left(\int_V \mathbf{J}^* \cdot \hat{\mathbf{e}}_\mathrm{x}\,\mathbf{e}^{-\mathbf{i\omega t}}\mathbf{dV}\right). \tag{2.8}$$

The incident electric field is assumed to be constant over the extent of the dipole. Using the relation[66][a)]

$$\int_V \mathbf{J}dV = \frac{d\mathbf{p}}{dt} = a\varepsilon_m E_\mathrm{inc}e^{i\omega t}\hat{\mathbf{e}}_\mathrm{x} \tag{2.9}$$

between current density $\mathbf{J}$ and the time derivative of the dipole moment, the volume integral is evaluated. The power extinct by the dipole simplifies to

$$P_\mathrm{ext} = \frac{1}{2}\varepsilon_m E_\mathrm{inc}\,\mathrm{Re}(-i\omega a\varepsilon_m E_\mathrm{inc}) = -\frac{\omega}{2}\mathrm{Im}(a)\varepsilon_m^2 E_\mathrm{inc}^2. \tag{2.10}$$

The extinction cross section is the fraction of extinct power and intensity $I_\mathrm{inc} = \frac{1}{2\eta}\varepsilon_m^2 E_\mathrm{inc}^2$ of the plane wave, where $\eta = \sqrt{\frac{\mu_0}{\varepsilon_0}}$ is the characteristic impedance of the vacuum,

$$\frac{P_\mathrm{ext}}{I_\mathrm{inc}} = \sigma_\mathrm{ext} = -\frac{k}{\varepsilon_0}\mathrm{Im}(a) = -4\pi k R^3 \mathrm{Im}\left(\frac{\varepsilon(\omega) - \varepsilon_m}{\varepsilon(\omega) + 2\varepsilon_m}\right). \tag{2.11}$$

The scattering cross section is calculated from the integrated Poynting vector of the reradiated field through a closed surface. The plane wave excites the dipole. The dipole reradiates the excitation energy. This process is called scattering. The details can be found in many textbooks like Bohren and Huffman.[64] The scattering cross section reads

$$\sigma_\mathrm{sca} = \frac{k^4}{6\pi\varepsilon_0^2}|a|^2 = \frac{8\pi}{3}k^4R^6\left(\frac{\varepsilon(\omega) - \varepsilon_m}{\varepsilon(\omega) + 2\varepsilon_m}\right)^2. \tag{2.12}$$

The difference between extinction cross section and scattering cross section yields the absorption cross section

$$\sigma_\mathrm{abs} = \sigma_\mathrm{ext} - \sigma_\mathrm{sca}. \tag{2.13}$$

For Rayleigh particles consisting of gold, absorption and extinction cross sections are approximately equal. The extinction cross section scales with the volume of the particle and the scattering one with

---

[a)] Private communication with Markus Selmke the volume squared. With reducing particle radius nanoparticles become very hard to detect by their scattering. Therefore, techniques that detect absorption seem to be superior for the detection of very small nanoparticles. However, many particles of interest like most biological materials do not absorb in the visible regime.

Interference scattering (iScat) has been shown to overcome the unfavorable size-dependence of the scattering. It has proven to image single biological macromolecules without any label. It does not image the scattering only like dark-field microscopy, but the interference between the scattered light and a reference field. A laser beam illuminates a sample consisting of particles located at an interface through an objective. A part of the incident light is reflected at the interface. The particle scatters another fraction. The illumination objective collects both parts and images them onto a photodetector. The detected signal is the interference between reflected field $\mathbf{E}_\mathrm{r}$ and scattered field $\mathbf{E}_\mathrm{s}$,[67,68]

$$I_\mathrm{det} = |\mathbf{E}_\mathrm{r} + \mathbf{E}_\mathrm{s}| = E^2_\mathrm{inc}(r^2 + |s|^2 - 2r|s|\sin\phi). \tag{2.14}$$

The interference signal depends on the reflectivity of the interface r, the scattering amplitude of the nano-object s and the interference term with the phase delay ϕ. The scattering amplitude is proportional to the particle's volume. The interference term scales with the particle's volume. For small particles the relative iScat signal is

$$\frac{I_\mathrm{det}}{I_\mathrm{bg}} \approx 1 - 2\frac{|s|}{r}\sin\phi. \tag{2.15}$$

Using this detection scheme, 45 nm sized bio-particles[69] have been detected at high frame rates and the detection of single proteins has been demonstrated.[70] The relative iScat signal can be significantly enhanced if the amplitude of the reflected light is reduced. This is achieved by a spatial transmission mask which transmits nearly all scattered light and only a small amount of the reflected light.[68,71]

2.1.3 Beyond the Rayleigh Approximation

The Rayleigh approximation is limited to spherical objects that are small compared to the wavelength. Mie theory gives the exact solution to Maxwell's equations where a spherical particle of arbitrary size is illuminated by a plane wave.[72] In the limit of small particles $R \gg \lambda$ Mie theory approaches the results obtained from Rayleigh scattering.[64] Once the dimension of the particles becomes a sizable fraction of the wavelength, the inner part of the sphere will be screened from the incident radiation and different regions will experience electromagnetic fields with different phases, i.e. the quasistatic approximation breaks down.[73] In the dipole mode opposite charges are approximately separated by one particle diameter and the maximal phase delay of the electromagnetic field in the particle is $4\pi Rn\lambda$. If one oscillation of the electromagnetic field takes place in the particle, higher order modes appear and contribute significantly to the interaction between particle and incident radiation.[73] The retardation of the field inside the particle will red-shift the absorption resonance. For the theoretical treatment of Mie theory and the interaction cross sections see for example Bohren and Huffman.[64]

Over the years, the original framework by Mie has been extended to account for more complex light fields or objects with spherical symmetric geometry and other symmetries.[74] These generalizations are called generalized Lorenz–Mie theories (GLMT). They enable various quantitative descriptions of trapping forces and radiation pressure exerted on particles as well as scattering images of nanoparticles.[75] The generalizations of the Lorenz–Mie theory are still limited to highly symmetric objects. For less symmetric particles, numerical algorithms are typically employed such as discrete dipole approximation (DDA) or finite difference time domain (FDTD).

2.1.4 Time Scales

The incident electromagnetic radiation polarizes the electrons in the conduction band and excites the bound electrons from the valence band into the conduction band. A hot electron gas is created. Within a time scale of 10 fs, the excited electrons are scattered by other electrons.[76] The excited electronic state has a considerably different equilibrium configuration of the lattice. The difference of the equilibrium configuration between cold and hot electrons exerts a pressure from the nanoparticle onto the surrounding medium, named Fermi pressure.[77] The electron gas is thermalized after about 100 fs. Due to the low heat capacity of the electron gas, its temperature can reach thousands of Kelvins.[77] Within a few picoseconds, the hot electron gas relaxes via electron–phonon scattering transferring the excitation energy to the lattice. The increase of the lattice temperature is typically in the order of a few Kelvin.[72] The rise of the lattice temperature results in an expansion of the nanoparticle which excites acoustic vibrations as well. The excitation of acoustic vibrations is typically investigated using femtosecond pulsed laser sources. For a spherical nanoparticle, the radial breathing mode is typically observed in the order of 10 ps. For other shaped particles, higher order acoustic modes can be excited as well.[78] The investigation of acoustic modes for single nanoparticles has unveiled a significant variation of the observed damping times which is caused by differences in the particles' inner structure.[78] For 80 nm-sized spherical gold nanoparticles, the period of the radial breathing mode is 25 ps and has a damping constant of 0.2 ns. The longest time scale is the heat transfer through the nanoparticle interface and the thermal transport outside the nanoparticle which is discussed in the following section.

2.2 Thermal Transport

This section will give a theoretical background on thermal transport. It includes discussions on the carriers of heat and the differential equations that describe the transport of thermal energy. In the second part of the section, it discusses the situations of importance in the thesis: A spherical heat source embedded in a homogeneous material. Finally, measurement techniques are discussed that quantify thermal transport.

2.2.1 Heat Conduction versus Heat Convection

Heat convection is the transport of heat due to the movement of atoms, molecules or particles, whereas heat conduction is the thermal transport inside a medium without mass transport typically due to phonons or conduction-band electrons. In this thesis metal nanoparticles are optically heated creating a local temperature elevation. In combination with thermal expansion the density of the liquid surrounding the heat source is lowered causing the hot liquid to ascend due to buoyancy. For gold nanoparticles as used in this thesis the resulting convection by the heated liquid is negligible. Due to the high localization of the temperature field, the buoyancy is damped on very short length scales. In liquids, the movement of nanometer sized objects is dominated by viscous forces in general. Quantitatively this is expressed by the Rayleigh number which relates the heat transported by conduction and convection,[1]

$$\mathrm{Ra} = \frac{\bar{v}\bar{l}}{\alpha} = \frac{\beta g \Delta T_0 \bar{l}^3}{\alpha \nu}. \tag{2.16}$$

Herein, $\bar{v}$ is the fluid velocity due to thermal buoyancy, $\bar{l} = 60\,\mathrm{nm}$ the characteristic length scale of the heat source, β the thermal expansion coefficient, $g = 9.81\,\mathrm{m\,s^{-1}}$ the gravitational acceleration, $\Delta T_0 = 60\,\mathrm{K}$ the temperature increase at the particle surface, $\alpha = 1.4 \cdot 10^{-7}\,\mathrm{m^2\,s^{-1}}$ the thermal diffusivity, $\nu = 0.9 \cdot 10^{-7}\,\mathrm{m^2\,s^{-1}}$ the kinematic viscosity. Using these values for a 60 nm-sized gold nanoparticle gives $\mathrm{Ra} = 10^{-10}$. This means that the thermal transport in this situation is dominated by heat conduction which is in general the case for $\mathrm{Ra} < 1$.

2.2.2 Fourier's Law

If a hot body is brought in contact with a colder reservoir heat will be transported from the hot to the cold. Over time, the temperature gradients are diminished until the body is in equilibrium with the reservoir. This process is described by Fourier's empirical law

$$\mathbf{q} = -\kappa \nabla T. \tag{2.17}$$

Fourier's law states that a temperature gradient ∇T causes a heat flux q that is proportional to the thermal conductivity κ of the medium. The proportionality between flux and gradient implies that heat conduction is a random process where the carriers of heat are scattered multiple times. In the ballistic regime the flux depends on the temperature difference.[79] Fourier's law has been derived from first principles only for an ideal gas moving between fixed scatterers and more recently for a system of coupled anharmonic oscillators.[80]

Fourier's law has the same shape like Fick's first law which describes the particle in a concentration gradient. In Fick's law the heat flux becomes the diffusion flux, the thermal conductivity becomes the diffusion constant and the temperature the concentration. Indeed, Fourier's law is the consequence of carriers of heat that diffuse freely in a medium. Fourier's law is widely validated in various kinds of systems, but it is limited to cases where the mean free path of the heat carriers is smaller than the dimensions of the system.

The breakdown of Fourier's law has been shown in various systems where the measured length scale is smaller than the phonon mean free path.[4] Nondiffusive thermal transport manifests in the proportionality of the thermal conductivity to the distance over which the heat is transported. The breakdown of Fourier law was for example observed in multiwalled carbon and boron nitride nanotubes,[81] graphene,[82] in silicon membranes,[83] in silicon germanium nanowires[84] and in crystals of several materials.[4]

Plugging the continuity equation $c_\mathrm{p}\rho\frac{dT}{dt} = -\nabla \mathbf{q}$ into Fourier's law, eq. 2.17, yields the heat equation

$$\rho c_\mathrm{p} \frac{\partial}{\partial t} T = \kappa \nabla^2 T + S(\mathbf{r}, t) \tag{2.18}$$

Name	Gold (NP)[86]	Water[86] (m)	PDMS[87]	Unit
density ρ	19.32	1.00	0.97	$\times 10^3\,\mathrm{kg\,m^{-3}}$
specific heat capacity c	129	4.187	1.35 – 1.51	$\mathrm{J\,kg^{-1}\,K^{-1}}$
thermal conductivity κ	317	0.60	0.15 – 0.17	$\mathrm{W\,m{-}1\,K^{-1}}$
thermal diffusivity α	127	0.143	0.102 – 0.132	$\times 10^{-6}\,\mathrm{m^2\,s^{-1}}$

Table 2.1: Material parameters for gold, water, and PDMS.

with a source term $S(\mathbf{r},t)$, the heat capacity at constant pressure c_p and the density ρ. The heat equation is a linear partial differential equation which has the same form as the diffusion equation. The heat equation describes the evolution of an initial temperature distribution and the temperature profile which is established for a heat source. In the following, the calculated temperature profiles are always on top of a constant ambient temperature. In the most general forms of eq. 2.18 the material parameters density ρ and heat capacity at constant pressure c_p can depend on temperature, thermal conductivity κ, and the thermal diffusivity $\alpha = \frac{\kappa}{\rho c_\mathrm{p}}$ can depend on temperature and direction.

2.2.3 Thermal Transport Around a Spherical Heat Source

Under resonant illumination, the nanoparticle absorbs electromagnetic energy. The excitation energy is dissipated as heat into the environment. Therefore, the nanoparticle acts as a remotely controlled nanosource of heat. The aim of this section is to quantify the temperature fields encountered if a spherical heat source is embedded into a homogeneous, isotropic material by solving the heat equation 2.18.

The following discussions follow loosely the publications by Baffou and Rigneault[85] as well as Berto and Baffou.[86] The material parameters are assumed to be constant and isotropic. Two different material domains are considered, one being the gold nanoparticle with (ρ_NP, c_NP, κ_NP, α_NP) and the other one the surrounding material (ρ_m, c_m, κ_m, α_m), which is typically water or a polymer. The gold particle is a sphere with the radius R. The interface has a finite interfacial thermal conductance G. The heat equation with the boundary condition reads[85]

$$\rho_\mathrm{NP} c_\mathrm{NP} \frac{\partial}{\partial t} T(r,t) = \kappa_\mathrm{NP} \nabla^2 T(r,t) + S(r,t), \quad r < R \tag{2.19}$$

$$\rho_\mathrm{m} c_\mathrm{m} \frac{\partial}{\partial t} T(r,t) = \kappa_\mathrm{m} \nabla^2 T(r,t), \quad r > R \tag{2.20}$$

Boundary condition at $r = R$:

$$\kappa_\mathrm{NP} \frac{\partial}{\partial r} T(R^-,t) = \kappa_\mathrm{m} \frac{\partial}{\partial r} T(R^+,t) = -GR[(T(R^-,t) - T(R^+,t)]. \tag{2.21}$$

Equation 2.19 quantifies the thermal transport inside the nanoparticle and includes the source term $S(r,t)$ caused by absorption. Equation 2.20 considers the thermal transport in the surrounding material. The boundary condition 2.21 guarantees the conservation of the heat flux through the interface and contains a finite interfacial thermal conductance G leading to a discontinuity in the temperature profile. Material parameters for some material of interest are given in table 2.1.

Steady State In the steady state the time derivatives in eq. 2.19 and 2.20 become zero which simplifies the solution considerably. The steady state solution is[85]

$$T^{\mathrm{cw}}(r) = \frac{P_{\mathrm{abs}}}{4\pi\kappa_{\mathrm{m}}R}\left[1+\frac{\kappa_{\mathrm{m}}}{2\kappa_{\mathrm{NP}}}\left(1-\frac{r^2}{R^2}\right)+\frac{\kappa_m}{GR}\right], \qquad r<R \tag{2.22}$$

$$T^{\mathrm{cw}}(r) = \frac{P_{\mathrm{abs}}}{4\pi\kappa_{\mathrm{m}}r}, \qquad r>R. \tag{2.23}$$

P_{abs} is the absorbed power caused by the optical heating. Considering the thermal conductivities of $\kappa_{\mathrm{m}} = 1\,\frac{\mathrm{W}}{\mathrm{m\,K}}$ and $\kappa_{\mathrm{NP}} = 317\,\frac{\mathrm{W}}{\mathrm{m\,K}}$ (gold), the fraction $\frac{\kappa_{\mathrm{m}}}{2\kappa_{\mathrm{NP}}}$ is negligible. Therefore, the temperature within the gold nanoparticle is assumed to be constant. Also one might question whether Fourier's law still applies in a gold nanoparticle as the electron mean free path and the phonon mean free path in gold[88] are in the order of the nanoparticle's size. The temperature of the nanoparticle is offset due to the interfacial thermal conductance which takes for water gold interfaces 50 to $150\,\mathrm{MW\,m^{-2}\,K^{-1}}$ depending on the hydrophobicity of the particle's surface functionalization.[89] Therefore, $\frac{\kappa_m}{GR}$ can take values between 0 and 2, which means that the temperature elevation of the nanoparticle can be three times higher than the one of the environment.

The outside temperature profile eq. 2.23 has only a one over r-dependence which is also observed for a point source. The temperature profile is independent of nanoparticle size and thermal interfacial conductance. The magnitude of the temperature elevation only depends on $P_{\mathrm{abs}}/\kappa_{\mathrm{m}}$ which is also observed for a point source.

If the temperature of the gold nanoparticle T_{NP} is assumed constant, the differential equation system 2.19 to 2.21 simplifies to[85,86]

$$\rho_{\mathrm{m}}c_{\mathrm{m}}\frac{\partial}{\partial t}T(r,t) = \kappa_{\mathrm{m}}\nabla^2 T(r,t), \quad r>R \tag{2.24}$$

Boundary conditions at $r=R$:

$$\frac{1}{3}R^3\rho_{\mathrm{NP}}c_{\mathrm{NP}}\frac{\partial}{\partial t}T_{\mathrm{NP}}(t) = \kappa_{\mathrm{m}}R^2\frac{\partial}{\partial r}T(R,t)+\frac{1}{4\pi}S(t) = -GR^2[T_{\mathrm{NP}}(t)-T(R,t)]. \tag{2.25}$$

The boundary condition eq. 2.25 assures that the thermal energy of the nanoparticle is changed by the optical heating and dissipated through the interface.

Harmonically Modulated Heating Assuming a harmonically modulated heat source $e^{-i2\pi ft}$ at the frequency f, the complex solution to the system of differential equations 2.24 and 2.25 gives the temperature elevations inside,[86]

$$T(r<R,t) = \frac{P_{\mathrm{abs}}}{4\pi\kappa_{\mathrm{m}}R}\left(1+\mathrm{Re}\left(\frac{e^{-i2\pi ft}}{\frac{1-ik_{\mathrm{th}}R}{1+\lambda_{\mathrm{K}}(1-ik_{\mathrm{th}}R)}-i\omega\tau_{\mathrm{m}}}\right)\right) \tag{2.26}$$

and outside the particle

$$T(r>R,t) = \frac{P_{\mathrm{abs}}}{4\pi\kappa_{\mathrm{m}}r}\left(1+\mathrm{Re}\left(T^{\omega}\right)\right) \tag{2.27}$$

$$T^{\omega}(r>R,t) = \frac{e^{ik_{\mathrm{th}}(r-R)-i2\pi ft}}{1-ik_{\mathrm{th}}R-i2\pi f\tau_{\mathrm{m}}[1+\lambda_{\mathrm{K}}(1-ik_{\omega}R)]}. \tag{2.28}$$

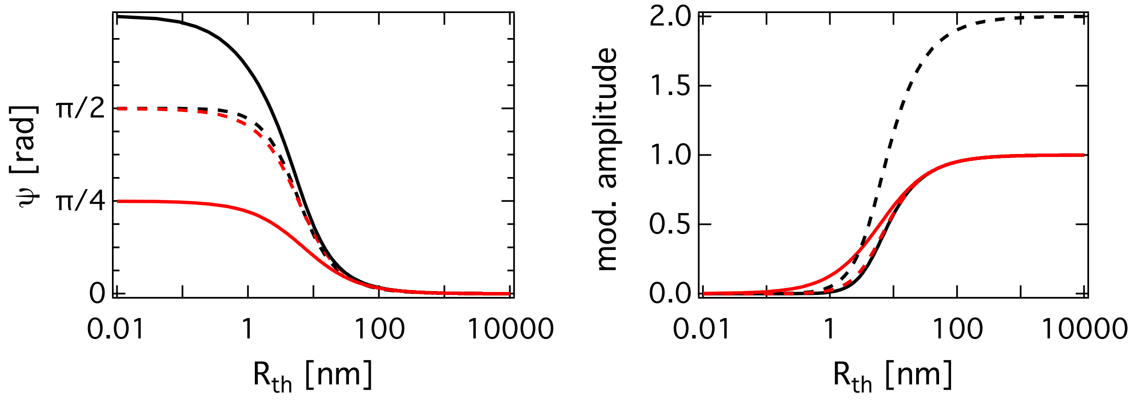

Figure 2.2: (left) Phase delay ψ and (right) normalized modulation amplitude $\Delta T(f;G;R)/\Delta T(f=0;G=\infty;R)$ of the temperature modulation. The solid lines are the temperature modulation amplitudes of the surrounding medium and the dashed ones of the particle. The black lines show ψ and $\Delta T(f)/\Delta T(0)$ without any approximations for a spherical gold particle in PDMS with $R = 5\,\mathrm{nm}$. The following material parameters were assumed: $G = 150\,\mathrm{MW\,K^{-1}\,m^{-2}}$,[89] $\alpha_\mathrm{m} = 1.3\cdot10^{-7}\,\mathrm{m^2\,s^{-1}}$, $\kappa_\mathrm{m} = 0.15\,\mathrm{W\,m^{-1}\,K^{-1}}$. The solid red line corresponds to the approximation $\tau_\mathrm{m} = 0$ (see eq. 2.31). The dashed red line assumes $G = -\infty$. In this case the temperatures inside and outside the particle are identical at $r = 5\,\mathrm{nm}$.

Herein, $k_\mathrm{th} = (1+i)/R_\mathrm{th}$ is the wavevector of the thermal wave, $R_\mathrm{th} = \sqrt{\frac{\alpha}{\pi f}}$ the thermal diffusion length. $\tau_\mathrm{m} = \frac{R^2 \rho_\mathrm{NP} c_\mathrm{NP}}{3\kappa_\mathrm{m}}$ gives the time scale at which the thermal energy of the nanoparticle is dissipated into the surrounding medium. $\lambda_\mathrm{k} = \frac{\kappa_\mathrm{m}}{RG}$ is the normalized Kapitza length. The limit $\tau_\mathrm{m} \to 0$ neglects the heat capacity of the nanoparticle. Then the temperature profile reads[a)]

$$N = \sqrt{(R/R_\mathrm{th})^2 + (1+R/R_\mathrm{th})^2} \tag{2.29}$$

$$\psi(r) = \frac{r-R}{R_\mathrm{th}} + \arctan\left(\frac{R/R_\mathrm{th}}{1+R/R_\mathrm{th}}\right) \tag{2.30}$$

$$\Delta T(r,t) = \Delta T \frac{R}{r}\left(1 + \frac{1}{N} e^{-\frac{r-R}{R_\mathrm{th}}} \cos\left(2\pi f t - \psi(r)\right)\right). \tag{2.31}$$

N and $\psi(r)$ are corrections to the modulation amplitude and the phase delay, respectively. The temperature inside the particle is $T(r<R,t) = T(R,t)$. In the limit of $R \to 0$, the classical thermal wave is obtained,[90]

$$T(r,t) = \frac{P_\mathrm{abs}}{4\pi\kappa_\mathrm{m} r}\left[1 + e^{-\frac{r}{R_\mathrm{th}}} \cos\left(2\pi f t - \frac{r}{R_\mathrm{th}}\right)\right]. \tag{2.32}$$

The functional dependence of the so-called thermal wave looks very similar to spherical waves encountered in optics. However, the physics of both system is very different. The thermal wave is critically damped over one thermal diffusion length. Spatial oscillations in the amplitude are not observed. Therefore, the term thermal wave is rarely used. The temperature profile in eq. 2.32 consists of a stationary part that transports the energy and a time-dependent oscillation that, in contrast to other wave phenomena, does not contribute to the energy transfer.[91]

[a)] Derived by Markus Selmke

radius	5	30	nm
τ_{NP}	0.2	7	ps
τ_{i}	41	250	ps
τ_{m}	33	1200	ps

Table 2.2: Time scales relevant for the thermal transport of gold nanoparticles embedded into water. Assuming an interfacial thermal conductivity of 100 MW m^{-2} K^{-1}. The characteristic times are defined in eq. 2.33–2.35.

Figure 2.2 shows phase delay and amplitude of the temperature modulation for a gold nanoparticle embedded into PDMS. The interfacial thermal resistance doubles the modulation amplitude of the particle's temperature. At thermal diffusion lengths larger than 100 nm the influence of τ_{m} and G on the phase delay is minor. At $R_{\mathrm{th}} = 200\,\mathrm{nm}$ the assumption of $\tau_{\mathrm{m}} = 0$ changes the phase only by 10^{-3} rad.

Time Scales of the Thermal Transport In section 2.1.4 absorption and the relaxation of the electronic excitations were discussed. Here, the focus is on the time scales caused by the thermal transport. From eq. 2.19 to 2.21 three different time scales can be identified. The first time scale is attributed to the thermal transport through the interface caused by the interfacial thermal resistance

$$\tau_{\mathrm{i}} = R\frac{\rho_{\mathrm{NP}} c_{\mathrm{NP}}}{3G}. \tag{2.33}$$

The time scale relevant for the dissipation of the thermal energy in the surrounding medium is

$$\tau_{\mathrm{m}} = R^2\frac{\rho_{\mathrm{NP}} c_{\mathrm{NP}}}{3\kappa_{\mathrm{m}}}. \tag{2.34}$$

The time scale for the thermal transport within the nanoparticle is

$$\tau_{\mathrm{NP}} = R^2\frac{\rho_{\mathrm{NP}} c_{\mathrm{NP}}}{\kappa_{\mathrm{NP}}}. \tag{2.35}$$

The time scale for the thermal transport inside the nanoparticle is three orders of magnitude faster than the thermal transport through the interface and thermal transport inside the surrounding medium. The time scale that is relevant for the thermal transport inside the particle is in the order of picoseconds. The time scale relevant for the thermal transport are in the range of picoseconds to nanoseconds. The time scale for the thermal transport is much larger than the period of the radial breathing mode of spherical nanoparticles which is about 25 ps for a gold nanoparticle with 80 nm in diameter. For sample numbers see table 2.2.

2.2.4 Anisotropic Heat Conduction

The thermal conductivity κ in eq. 2.18 becomes a second rank tensor in case the latter depends on direction. If a point source is embedded into an anisotropic medium, the heat conduction equation is analytically solvable in the steady state. One approach is based on integral transforms that convert the differential equation into an integral expression which is then solved. If the thermal conductivity is diagonal, the temperature profile is given by[92]

$$T(\mathbf{r}=(x,y,z)) = \frac{P_{\mathrm{abs}}}{4\pi\sqrt{\kappa_{11}\kappa_{22}\kappa_{33}}} \frac{1}{\sqrt{\frac{x^2}{\kappa_{11}}+\frac{y^2}{\kappa_{22}}+\frac{z^2}{\kappa_{33}}}}. \tag{2.36}$$

Herein, κ_{ii} are the thermal conductivities along the principal axes. For the general case of symmetric thermal conductivity tensors a solution exists as well.[92] Here, a uniaxial crystal is of interest where only one axis has a deviating thermal conductivity, i.e. $\kappa_{11} = \kappa_{22} = \kappa_{\perp}$ and $\kappa_{33} = \kappa_{\parallel}$. Then the temperature profile 2.36 simplifies to

$$T(\mathbf{r}) = \frac{P_{\mathrm{abs}}}{4\pi\kappa_{\perp}} \frac{1}{\sqrt{\frac{\kappa_{\parallel}}{\kappa_{\perp}}(x^2+y^2)+z^2}}. \tag{2.37}$$

Notably an anisotropy of $\frac{\kappa_{\parallel}}{\kappa_{\perp}} = 2$ in the thermal conductivity results in an anisotropy of $\frac{T(\mathbf{r}=(0,0,1))}{T(\mathbf{r}=(1,0,0))} = \sqrt{2}$ in the temperature profile, which is the fraction of temperature along x and z at the same distance.

2.2.5 Thermal Transport Including Phase Transitions

Phase transitions occur for example in the context of solidification and melting. During these processes the latent heat capacity H_{f} is either released or taken up. Here, one is interested in the time evolution of the phase boundary between liquid and solid phase. For the stated problem only a very limited set of solutions to semi-infinite problems do exist.[93] Most geometries like a point source or a spherical heat source have to be addressed numerically.

Several approaches exist that solve the problem numerically. A simple method that can easily be implemented into existing finite element models is the apparent heat capacity method.[93] The method assumes that the phase transition occurs in a temperature interval $T_{\mathrm{C}} \pm \Delta$ around the phase transition temperature T_{C} where both phases coexist. The heat capacity in the heat conduction equation is then given by[93]

$$c_{\mathrm{app}} = \begin{cases} c_{\mathrm{s}} & T < T_{\mathrm{C}} - \Delta & \text{solid phase} \\ c_{\mathrm{sl}} & T_{\mathrm{C}} - \Delta <= T <= T_{\mathrm{C}} + \Delta & \text{solid/liquid phase} \\ c_{\mathrm{l}} & T_{\mathrm{C}} + \Delta < T & \text{liquid phase.} \end{cases} \tag{2.38}$$

Herein, c_{s} is the specific heat capacity in the solid phase, c_{l} in the liquid phase and

$$c_{\mathrm{sl}} = \frac{1}{2\Delta}\left(\int_{T_{\mathrm{C}}-\Delta}^{T_{\mathrm{C}}+\Delta} C(T)dT + H_{\mathrm{f}}\right) \tag{2.39}$$

in the temperature interval where both phases coexist. Conceptually the method is very simple and can be used in existing numerical simulations. Problems arise if the temperature changes strongly during one calculation step. Then the transformation of latent heat during the phase transition is not captured. To circumvent this problem the temperature change during a time step has to be smaller than Δ. For that reason, the apparent heat capacity method is computationally very demanding. Also, the introduction of the artificial phase coexistence might alter the results of the calculation. Other numerical schemes can overcome the limitations of the simple approach.[93]

2.2.6 Measurement Schemes

The general principle behind all measurements of thermal transport is to induce a thermal perturbation and observe its evolution. The measurement can be performed in the steady state where the rate of heat transport is measured. The dynamic measurement schemes either induce a delta-like temperature elevation in a local region that is dissipated or a time-harmonic temperature variation. In the following, some frequently used measurement schemes are presented shortly.

Steady State Measurement Schemes Scanning thermal microscopy is a probe scanning technique which is typically implemented in an atomic force microscope.[10,11] The atomic force microscope is operated in contact mode where the force between sample and tip is kept constant. The tip is the temperature sensor and heating element at the same time. While moving the tip, the thermal power deposited into the sample is measured. From the measurement, an image is obtained that maps thermal conductivities to locations in the sample.

An approach frequently applied for the study of nano- and microwires is the heat transfer measurement between a heat source and a heat sink.[94] The experiment is set up similar to electrical transport measurements. Two platinum resistors are produced. They are thermally connected by the sample. Applying an electrical current to one resistor a temperature gradient along the wire is created. The measurement of the Ohmic resistance of the platinum structures gives the temperature. In combination with the applied heating power the thermal conductivity of the sample is calculated.[12,84]

Dynamic Measurement Schemes in the Frequency Domain The 3ω or hot wire method can be applied to study thermal transport of electrically isolating materials. It uses, for example, a metal strip that is evaporated onto a substrate. A harmonically modulated voltage at the angular frequency ω is applied to a metal wire which creates a time-harmonic temperature modulation at 2ω. Due to the temperature variation the electric resistance of the metal strip will oscillate at 3ω, which is used as the temperature sensor, and the thermal conductivity is derived with the help of a numerical model.[95]

Using macroscopic photothermal lensing or deflection, thermal conductivities and diffusivities can be detected. The absorber is, in this case, a volume absorber whose size is given by the beam diameter.[96] The working principle is analog to single particle photothermal microscopy which is described in detail in section 2.4.

Dynamic Measurement Schemes in the Time Domain The flash method[5] is one of the classic methods to study the thermal transport of macroscopic samples. Samples consist of even, parallel interfaces and are coated with a light-absorbing material. One interface is the heat plate which is excited by the laser flash. An infrared temperature sensor monitors the temperature of the second interface.

The working principle behind transient reflection is similar to the flash method.[6] Here, a metallic film is evaporated onto the sample. A pulsed laser beam irradiates the metal film, and a part of the incident radiation is absorbed and transformed into thermal energy heating the metal film. This heat is transferred to the sample. A second time-delayed laser pulse monitors the rate of thermal transport. The temperature measurement is based on the assumed proportionality between temperature change and reflectivity change. Modeling the transient response of the reflection allows for the extraction of thermal conductivity and heat capacity.

Conceptually transient absorption is an adaptation of transient reflection for studies of nano-objects. Two time-delayed laser pulses are irradiated onto nano-objects. A pump pulse excites partiles which then relax. In the case of single metallic nanoparticles, the relaxation is predominantly via nonradiative processes. Therefore, the sample is heated. The refractive index changes of nanoparticle and environment are assumed to be proportional to the temperature elevation. This assumption allows the calculation of the thermal conductivity and heat capacity.[7,8] Besides the investigation of the thermal transport, transient absorption allows for studies of the acoustic properties of the nanoparticle. The acoustic vibrations disturb the thermal transport measurement due to oscillations in the transmission signal. These acoustic oscillations do not contribute significantly to the energy dissipation. The oscillations are typically in the order of 10 GHz, whereas the phonons with the largest contribution to heat conduction are typically in the order of 1 THz.[97] The investigations of the acoustic modes can give many details on the internal structure of the nanoparticles.[78]

2.3 Liquid Crystals

The name liquid crystal comprises two contradicting terms. In a crystal, molecules or atoms have long-range positional order. In a liquid on the other hand molecules or atoms can move freely. Only short range particle–particle repulsions restrict the free movement of the particles. The liquid crystalline phase is an intermediate phase between the crystalline and the liquid state of matter occurring for specific types of materials. In particular, liquid crystals are typically formed from elongated molecules which can have an orientational order as well. For these kinds of molecules, the order does not vanish completely during the melting. During the melting process, the elongated molecules loose one or more degrees of positional order, and the orientational one remains. Therefore, the name liquid crystal was chosen. There are two different groups of liquid crystals which are discriminated in the way the phase transition is induced. In the case of thermotropic liquid crystals, phase transitions are induced by temperature changes. For lyotropic liquid crystals changes of the concentration alter the material's phase. Depending on the shape and properties of the molecules different shapes of liquid crystalline phases are observed.[98]

In this thesis, optically heated gold nanoparticles are used as actuators that control the size of the isotropic liquid crystal shell around the particle. Therefore, a thermotropic liquid is chosen that has its nematic–isotropic phase transition close above room temperature. 4-Cyano-4'-pentylbiphenyl (5CB) is employed which melts at 296 K and crosses from the nematic to the isotropic phase at $T_\mathrm{C} = 307.5\,\mathrm{K}$.[99] During the melting process 5CB looses all its positional order and the orientational order is unchanged. The orientational order is lost in the nematic to isotropic phase transition. The liquid crystal becomes isotropic (see fig. 2.3).

5CB is uniaxial. One principal axis has different properties than the other ones. The unique axis is called extraordinary axis and is parallel to the director which is the average orientation of the long molecule axis. In the following, the properties parallel to the director are labeled with $\|$ and $\perp$ for the other ones. In bulk, the orientation of the director is random and changes over the extent of the

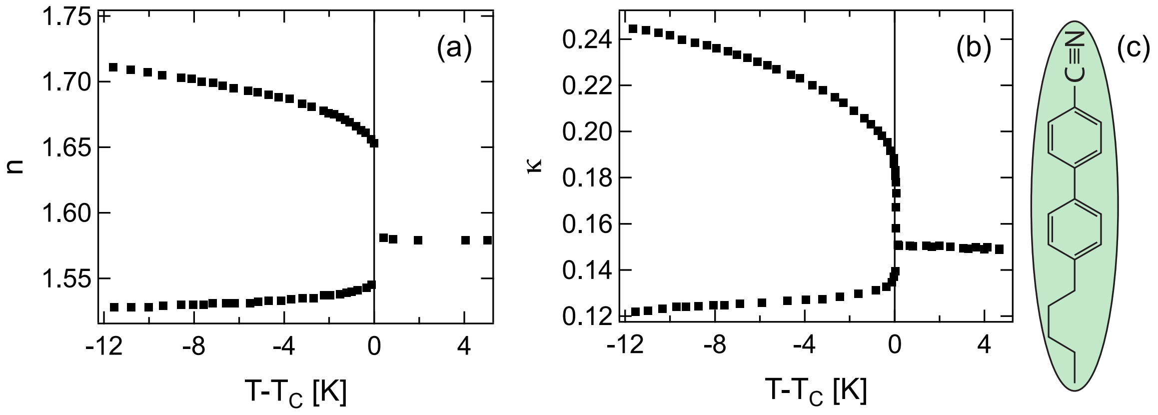

Figure 2.3: (a) Refractive index of 5CB. Top branch refractive index $n_{\parallel}$ of the extraordinary axis and bottom one $n_{\perp}$ of the ordinary axis.[101] (b) Thermal conductivity of 5CB. Top branch thermal conductivity $\kappa_{\parallel}$ parallel to the director and bottom one $\kappa_{\perp}$ perpendicular to the director.[102] (c) Chemical structure of 5CB. T_C=307.5 K.

sample. By inducing small forces from surfaces or electric fields, the liquid crystal molecules are aligned. Here, the orientational order is induced by rubbed polymer films.[100]

The liquid crystal's directional order leads directly to anisotropic material properties like viscosity, refractive index, and thermal conductivity. The molecules fluctuate around the director. These fluctuations increase with temperature and lower the anisotropic material properties. At the nematic to isotropic phase transition, the orientational order is lost. All material properties of 5CB become isotropic. The order parameter quantifies the fluctuation of the molecules around the director. For rigid and cylindrical symmetric molecules the order parameter is[103]

$$S = \left\langle \frac{3\cos^2\beta - 1}{2} \right\rangle, \tag{2.40}$$

which is identical to the average of the second Legendre polynomial $P_2(\cos\beta)$. The order parameter is 1 if all molecules face into the same direction and 0 for a random distribution. The order parameter reduces as the phase transition is approached, and the anisotropies of thermal conductivity and refractive index decrease as well (see fig. 2.3).

Optical Properties of 5CB For liquid crystals, the dipole moment of the molecules is assumed to be maximal parallel to the axis of cylinder symmetry. The orientational ordering of the molecules also leads to an ordering of the molecular polarizabilities. Then a linearly polarized beam of light experiences different refractive indexes depending if the light is polarized parallel to the director $n_{\parallel}$ or perpendicular to it $n_{\perp}$. In 5CB, the director is parallel to the optical axis. The optical anisotropy of a uniaxial crystal is called birefringence $n_{\parallel} - n_{\perp}$.[101,103]

Thermal Properties of 5CB The molecules are assumed to be rods to model the anisotropic thermal conductivities of liquid crystals. The model is based on two assumptions: The free volumes parallel and perpendicular to the director are different, and the heat transfer from molecule to molecule has a finite rate. From this model, it follows that the thermal conductivity along the director is larger than perpendicular to it. The strength of the anisotropy $\kappa_{\parallel} - \kappa_{\perp}$ depends mostly on the length of the rigid core and to a lesser extent on aliphatic side chains. Finally, the thermal conductivity is independent on long range order effects.[102]

The second parameter determining the thermal transport is the heat capacity. The heat capacity of bulk 5CB is $1.8\,\mathrm{kJ\,kg^{-1}\,K^{-1}}$ and increases as the phase transition is approached.[104] The heat capacity in the isotropic phase is $0.1\,\mathrm{kJ\,kg^{-1}\,K^{-1}}$ lower than in the nematic phase. The specific heat is found to increase as the nematic to isotropic phase transition is approached. Confinement of 5CB to less than 200 nm in at least one dimension alters the heat capacity as well. The specific latent heat transformed during the nematic to isotropic phase transition is $1.6\,\mathrm{kJ\,kg^{-1}}$.[104]

2.4 Photothermal Single Particle Microscopy

Three successive processes lead to the photothermal contrast. Firstly, a particle absorbs electromagnetic energy from incident light. The absorber is excited. Secondly, the excitation energy is dissipated via nonradiative processes into the environment creating a localized temperature elevation. Finally, the local temperature increase alters the refractive index of the environment surrounding the absorber. Here, various effects are possible depending on the properties of the materials used and the employed laser intensities. A universal process at moderate laser intensities is thermal expansion.[105] The photothermal contrast is the basis for a variety of highly sensitive measurement techniques.[106]

The local thermal expansion has two effects, it creates local stresses and changes the refractive index. The local stresses lead to acoustic waves. However, the latter are significant only if the time it takes an acoustic wave to pass the heated volume is larger than the duration of the optical heating. In the other case, the stresses are relaxed before they are built up.[105] It takes an acoustic wave about 18 ps to pass a 60 nm-sized gold nanoparticle, which also defines the frequency of the radial breathing mode of the nanoparticle being the dominant acoustic mode.[78] Therefore, femtosecond-pulsed laser sources are required to excite acoustic vibrations of nanoparticles. However, gold nanoparticles are also used as labels for photoacoustic imaging where typically nanosecond-pulsed laser sources are employed. Here, gold nanoparticles in an extended volume are heated and then act as a volume heat source.[107]

Once the stresses are released the thermal energy is transported into the environment establishing a localized temperature profile. In combination with thermal expansion, the refractive index is lowered locally. A refractive index profile is created depending on the geometry of the heat source. The refractive index profile acts as a diverging lens. The change of the index of refraction is usually detected with a second off-resonant laser beam whose propagation is altered.[106] As the refractive index change is only in the order of $10^{-4}\,\mathrm{K^{-1}}$ photothermal microscopy is implemented as a modulated detection scheme where the heating laser is modulated at a frequency f and a second off-resonant detection laser probes any variation at f. Using a lock-in amplifier, modulation amplitude of the probe laser and the phase between heating and detection modulation are measured at high signal to noise ratios despite weak modulation amplitudes. The repeated measurement of changes of the thermal state makes photothermal microscopy an extremely sensitive measurement technique. The photothermal signal itself is shot-noise limited.[108]

In 1965 Gordon et al. observed that the transmission of an intense laser beam was altered upon passing through a long tube filled with liquids.[109] This experiment was the first observation of the photothermal effect. In the following decades, photothermal spectroscopy was significantly improved and has become a standard measurement technique for determining molecule concentrations or thermal transport.[106] Photothermal spectroscopy is typically based on volume absorption meaning that either the entire liquid absorbs light or multiple absorbers are present in the focus of the pump laser. In 2002 Boyer et al. imaged single gold nanoparticles with photothermal differential interference contrast.[43] Subsequently, single particle photothermal microscopy was advanced and has proven single molecule sensitivity.[31] In the same year single molecules were detected using ground state depletion[110] and a microscopic variant of the standard Beer–Lambert experiment.[111] In the following, the focus is on single particle photothermal microscopy: experimental implementations, a ray optics model for the photothermal lensing variant and applications.

2.4.1 Photothermal Detection of Single Nano-Objects

The working principle of all photothermal detection schemes is very similar. They only differ in the way the localized refractive index profiles are detected. All approaches feature a modulated resonant heating laser beam that creates a local variation of the refractive index around the absorber. Thereby, the signal of the detection laser is modulated. The modulation amplitude of the detection signal is referred to as the photothermal signal. This principle makes photothermal microscopy a highly sensitive and selective detection scheme for absorbers.

Point Detection Upon optical heating of a nano-object, a localized temperature profile is created that results in a refractive index profile due to thermal expansion also called a thermal lens. This refractive index profile alters the propagation of a second off-resonant laser beam. Depending on the position of the detection laser focus and the position of the excited absorber the detection laser beam is either expanded or collimated.[26,28] The change in divergence is detected by measuring the transmission through an aperture. Due to the modulated optical heating, the detection signal is modulated as well. A lock-in amplifier detects phase and amplitude of the detection signal at the modulation frequency of the optical heating. This detection scheme was developed by Berciaud et al.[53] and was advanced to enable the detection of single molecules.[31] If the detection laser beam passes the thermal lens while it is offset from the optical axis, the laser beam is deflected probing the gradient of the refractive index. This action is detected by a split detector.[29,30]

The initial photothermal detection of single nano-objects utilized an interferometric detection scheme which detects the heating induced change of the optical path. Using a Wollaston prism, the detection laser beam is split into two perpendicularly polarized beams of light that exit at different angles. The modulated heating laser beam is co-aligned with one of the beams and a 4-f system images parallel beams of light with different angles into the back aperture of the objective. In the object plane, the detection laser beams have a distance of about 1.2 µm.[43] A difference in the phase between both laser beams changes the incident linear polarization which is detected by an analyzer and a photodiode. Recently, the detection scheme was altered to detect flow speeds of nanoparticles where both detection beams are co-aligned with a heating laser beam.[112]

Widefield Detection Another variant of the interferometric detection works in the widefield and is set up as a Michelson–Morley interferometer. One arm of the interferometer consists of the sample which is illuminated by the co-aligned heating laser beam and the detection laser beam. The interference is imaged onto a CCD camera.[113] The heating beam is again modulated. The signal to noise of this approach is much lower as the difference between hot and cold particle is probed less frequently, and the dynamic range of a CCD is much lower compared to a photodiode. Other approaches that detect the photothermal optical path difference are based on holography[114] or wavefront sensing.[115] Optical coherence tomography is another technique capable of photothermal widefield detection. It utilizes a low coherence detection beam of light. The interference is then spectrally resolved. The electric field scattered by the nanoparticle interferes with a reference field. The nanoparticle is again heated by a harmonically modulated heating laser.[116] This implementation has similar disadvantages as the latter two described before.

Pache et al. improved the photothermal detection using optical coherence tomography. Their variant is called optical lock-in detection and enables modulation frequencies which are not limited by the frame rate of the photodetector.[117] The reference field is phase modulated, and interferes with the light scattered by the object. The detector integrates the interference field over multiple periods. In this way the static contributions vanish and only the time-varying signal induced by the optical heating remains.

The resolution remains an issue for widefield photothermal detection. The optical heating creates a long range $1/r$ temperature profile and different heat sources can superimpose themselves. Then the superposition of the temperature profiles is detected. Single nanoparticles might not be detected individually despite being resolvable according to the Rayleigh criterion. In the point detection schemes optical heating and detection are diffraction-limited. The resolution is only limited by the spatial extent of the laser foci. The resolution of widefield photothermal microscopy might be enhanced by using deconvolution techniques.[115]

2.4.2 Modeling the Photothermal Lensing Signal

The physics encountered in single particle photothermal lensing have been studied in great detail.[118,119] There are a many different ways to model the photothermal signal generated by a single nanosource of heat. The two models employed here are the generalized Lorenz–Mie theory and a ray optics model based on Fermat's principle. These models belong to opposite sides of the spectrum of theories describing the photothermal signal. Other approaches are based on an equivalent dipole model, Fresnel diffraction or Rutherford scattering.[119]

Generalized Lorenz–Mie Theory A situation typically encountered in photothermal microscopy is a single spherical absorber that is embedded into a homogeneous environment. Using Mie theory, it is possible to calculate the absorption and scattering cross sections for a plane wave that illuminates the nanoparticle. Mie theory is the exact solution of Maxwell's equations for the described geometry.[64] The situation in photothermal microscopy is more complex. The photothermal signal itself originates from the refractive index profile around the nanoparticle induced by optical heating. Mie's theory has been extended also to capture the case of multilayered spheres.[120] In the center is the absorbing spherical particle which is surrounded by fine layers that approximate the spherical symmetric refractive index profile. This extension is still insufficient as the plane wave is not capable of explaining the dispersive lensing signal observed in photothermal microscopy as in fig. 2.4. In particular,

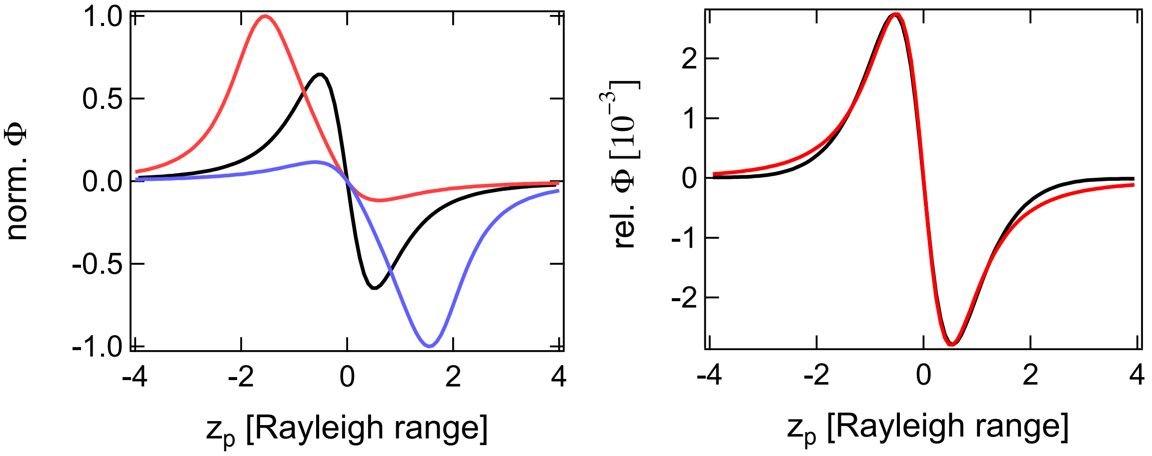

Figure 2.4: (left) The normalized photothermal signal from eq. 2.47 with $\Delta z_F = 0$ (black), $\Delta z_F = +2z_R$ (blue), $\Delta z_F = -2z_R$ (red); $z_R/z_{R,h} = 1.22$.[28] (right) Photothermal Signal with a diffraction model[27] (black) and from the (left) figure with a new normalization. Maximal temperature increase $\Delta T_{max} = 100\,\mathrm{K}$, detection wavelength $\lambda_d = 635\,\mathrm{nm}$, heating wavelength $\lambda_d = 532\,\mathrm{nm}$, $z_R = 570\,\mathrm{nm}$, $z_{R,h} = 470\,\mathrm{nm}$, $NA_{ill} = 1.4$, $NA_{det} = 0.75$, $n_0 = 1.46$, $\partial n_T = 3.6\cdot 10^{-4}\,\mathrm{K}^{-1}$, and $R = 10\,\mathrm{nm}$.

a plane wave model neglects the local character of the probing and the Gouy phase.[119] The model has to include a focused illumination. This approach was indeed followed by Selmke et al.[26,118] for an exact description of the photothermal signal. The approach is found in the literature under the term generalized Lorenz–Mie theory (GLMT). The original solution by Gustav Mie, where a single particle is illuminated by a plane wave, is generalized to arbitrarily shaped electromagnetic fields and the layered spherical refractive index fields.[121]

A calculation of the photothermal signal using the GLMT computes the transmission of the detection when the nanoparticle is heated and unheated. The relative difference $\Phi = (P_{cold} - P_{hot})/P_{cold}$ gives then the photothermal signal. The strength of the GLMT approach is that influences on the photothermal signal like particle size, pupil-filter in the detection path and aberration are all included. Details on the derivation and the implementation of the model can be found in thesis by M. Selmke[118] and more general information in the book by Gouesbet and Gréhan.[74]

Ray Optics Using Fermat's principle the trajectory **r** of a light ray is calculated that is subject to the refractive index field induced by an optically heated object. Fermat's variation principle allows to calculate the path a ray of light takes between two points in space in the presence of an inhomogeneous refractive index field $n(\mathbf{r})$. In its differential form Fermat's principle reads as[122]

$$\frac{d^2\mathbf{r}}{ds} = \nabla\left(\frac{1}{2}n^2(\mathbf{r})\right), \qquad \left(\frac{d\mathbf{r}}{ds}\right) = n(r), \tag{2.41}$$

where s is the path coordinate. In the stationary state a spherical heat source with the radius R reduces the refractive index $n(r)$ locally,

$$\Delta n = \partial_T n \frac{P_{abs}}{4\pi\kappa R}. \tag{2.42}$$

Here, Δn is the refractive index contrast which depends on the thermal conductivity κ, the absorbed power P_{abs} and the refractive index change with temperature $\partial_{\mathrm{T}} n$. The strength of the deflection, i.e. the deflection angle, depends on the relative strength of the refractive index perturbation $\zeta = -n_0/R\Delta n$ and the impact parameter b. n_0 is the refractive index of the surrounding medium. The focal length of the thermal lens is calculated from the deflection angle of the thermal lens,[28]

$$f(b) \approx \frac{b^2 n_0}{2\Delta n R}. \tag{2.43}$$

This approximation is valid in the regime of small refractive index perturbations $\Delta n \ll n_0$. A Gaussian beam with the beam waist ω_0 and a Rayleigh range $z_{\mathrm{R}} = \pi\omega_0^2/\lambda$ will experience an effective focal length depending on the distance between focus and particle position on the optical axis z_{p}. λ is the wavelength. A natural choice is the weighting of b^2 with the Gaussian intensity profile giving

$$b^2_{\mathrm{eff}}(z_{\mathrm{p}}) = \frac{w_0^2}{2}\left(\frac{z_{\mathrm{p}}^2}{z_{\mathrm{R}}^2} + 1\right). \tag{2.44}$$

z_{p} is the difference between the positions of the detection laser focus and the particle on the optical axis. Using b^2_{eff} the focal length of the thermal lens for an offset Gaussian beam is evaluated to[28]

$$f_{\mathrm{eff}} \approx \frac{n_0}{\Delta n}\frac{\omega_0^2}{4R}\left(\frac{z_{\mathrm{p}}^2}{z_{\mathrm{R}}^2} + 1\right). \tag{2.45}$$

The relative photothermal signal is the transmission change of the detection laser upon heating, $\Phi = (P_{\mathrm{th}} - P_0)/P_0$. Here, the transmitted power with and without the optical heating are related to the corresponding intensities on the optical axis. Then the relative photothermal signal is expressed via $\Phi = (I_{\mathrm{th}} - I_0)/I_0$. Using ABCD matrix optics the beam waist of the Gaussian probe beam is calculated with and without the optical heating. The change of the beam waist readily gives the intensity of the probe beam as the intensity of a Gaussian beam is inverse proportional to the squared beam waist, $I \propto \omega^{-2}$. In the far-field and the weak lens limit, the photothermal simplifies to[28]

$$\Phi(z_p) = \frac{2z_{\mathrm{p}}}{f}. \tag{2.46}$$

The effective focal length of the Gaussian probe beam is plugged into eq. 2.46. The intensity of the heating laser is assumed to be Gaussian as well having the Rayleigh range $z_{\mathrm{R,h}}$. Then an analytical expression for the photothermal signal is obtained,[28]

$$\Phi = \frac{\Delta P}{P_{0,\mathrm{d}}} = \frac{2}{\pi\omega_0^2}\frac{\partial_{\mathrm{T}} n}{n_0}\frac{\sigma_{\mathrm{abs}}}{\kappa} I_{0,\mathrm{h}} \left[\frac{(z_{\mathrm{p}} - \Delta z_{\mathrm{f}})^2}{z_{\mathrm{R,h}}^2} + 1\right]^{-1} z_{\mathrm{p}} \left[\frac{z_{\mathrm{p}}^2}{z_{\mathrm{R}}^2} + 1\right]^{-1}. \tag{2.47}$$

Here, Δz_{f} is distance between both laser foci. Changing the distance between the laser foci along the optical axis affects the shape of the photothermal signal. The photothermal signal can be only positive for $\Delta z_{\mathrm{F}} < 3z$, only negative for $\Delta z_{\mathrm{F}} > 3z$ and has a double loped-structure for $\Delta z_{\mathrm{F}} \sim 0$ (see fig. 2.4 (left)). Despite the dimensions being smaller than the wavelength of the light, the ray optics models gives similar results like a diffraction model (see fig. 2.4 (right)).

Due to the thermal lens, the detection laser intensity is either increased or lowered. The probe beam is collimated or dispersed, respectively. An expression frequently found in the literature is the maximal photothermal signal. Equation 2.47 allows to derive a simple expression for the maximal photothermal signal. Assuming that both laser foci are not offset along the optical axis $\Delta z_f = 0$ and have comparable Rayleigh ranges $z_{R,h} \approx z_R$, the maximal photothermal signal is approximately

$$\Phi_{\max} \approx \frac{2}{3\pi\omega_0^2} \frac{\partial_T n}{n_0} \frac{\sigma_{abs}}{\kappa} I_{0,h}. \tag{2.48}$$

The use of $\Delta z_f \neq 0$ changes the amplitude by a prefactor in the order of one. In eq. 2.48 all parameters appear naturally. $\Phi_{\max}$ is proportional to the relative refractive index change with temperature $\partial n_T / n_0$. The term $\frac{\sigma_{abs}}{\kappa} I_{0,h}$ is attributed to the temperature elevation. A larger temperature increase results in a larger $\Phi_{\max}$. The inverse proportionality to the inverse beam waist squared is explained by the assumption of a point source. If the beam waist decreases, the effective focal length f_{eff} increases as the contribution of the region close to the point source where large changes occur is increased.

2.4.3 Information Contained in the Photothermal Signal

Due to its nature, the photothermal signal contains information on absorption and the thermal transport. Both features are well known and used in experimental observations. As the photothermal signal is proportional to the absorption cross section (see eq. 2.48), the technique is well suited to measure this quantity. Assuming that the thermorefractive coefficient and thermal conductivity are constant, the temperature elevation is proportional to the absorption cross section. This dependence is used to quantify absorption cross sections of metallic nanoparticles,[26,36,39] quantum dots,[33] molecules[31] and carbon nanotubes.[38]

The measurement itself is more complex as the intensity of the heating laser is hard to determine and subject to aberration. This issue is typically resolved by performing a reference absorption measurement for a sample where the absorption cross section is well known. Possible candidates are gold nanoparticles[31] or gold films.[39] The other approach is to include the aberration in the modeling of the photothermal signal using a generalized Lorenz–Mie theory.[26]

Another application of photothermal microscopy is the study of adsorption on the nanoparticle's surface. The adsorption layer alters the absorption of the nanoparticle as a change in the refractive index also alters the absorption cross section. On the other hand, the thermal transport is altered. The adlayer has a different thermal conductivity and adds an interface that has an interfacial resistivity due to the acoustic mismatch. The study by Koh et al. indeed measured a change in the photothermal signal after adsorption of molecules and reported that the change was due to a six-times lower thermal conductivity in the adlayer than in the surrounding liquid.[123] Zijlstra et al. reported a change of the photothermal signal of a nanorod upon adsorption of single proteins which was attributed to the local refractive index change by single proteins.[124]

The photothermal signal is inverse proportional to the thermal conductivity of the medium surrounding the absorber (see eq. 2.48). But, as already mentioned, the determination of the absorbed power is very hard due to aberrations. Also the power absorbed by a particle is proportional to its volume, $\sigma_{abs} \propto R^3$. Therefore, it is not feasible to determine the thermal conductivity from a static measurement. Luckily, there is a different approach based on the modulation of the optical heating f. In the first observation of single particle photothermal microscopy, it was observed that the photothermal signal depends on the modulation frequency.[43] If the thermal diffusion length $R = \sqrt{\frac{\alpha}{\pi f}}$, α being the thermal diffusivity, becomes smaller than the diameter of the probe laser beam the photothermal signal drops.[43,53] In other words, the temperature profile is not completely modulated during a modulation cycle. Using this approach the thermal diffusivity could be measured. Past approaches have failed to extract reasonable thermal diffusivities. Using a simplified model Berciaud et al. determined thermal diffusivities that were at least three-times lower than what is expected for an organic liquid.[53,54] The disagreement is the result of a simplified model.

2.4.4 Signal Enhancement

The photothermal signal is proportional to the refractive index change with temperature (see eq. 2.48). To make photothermal microscopy highly sensitive, it is desired that a small temperature elevation creates a large signal. The enhancement in sensitivity is, for example, required to study the absorption and fluorescence at the same time.[32] A material class that features a significant refractive index change slightly above room temperature are some thermotropic liquid crystals such as 5CB. Thermotropic liquid crystals consist of rodlike molecules that have direction-dependent polarizabilities. The orientational order of molecules makes them birefringent (see also section 2.3). At the nematic to isotropic phase transition, liquid crystals loose their anisotropy and become isotropic. Therefore, the refractive index change is significant for polarizations parallel to the principal axes. It was indeed observed that the photothermal signal in 5CB is up to a factor of 20 compared to glycerol.[125,126] However, these publications do not include discussions of the optimal parameters in the intensity of the optical heating and the modulation frequency. Therefore, the measured signal enhancement of 20 is only a lower boundary.

The perception that the modulation frequency, sample temperature as well as heating and detection power influence the photothermal signal and, thereby, the signal to noise in a nonlinear manner is supported by mid-infrared photothermal spectroscopy studies of thermotropic liquid crystals.[127,128] In 4-Cyano-4’-octylbiphenyl (8CB) for example, the photothermal signal drops with the absorbed power for a sample that is heated to about 1 K below the nematic–isotropic phase transition temperature and the optical heating exceeds a certain threshold. In this case, the modulation of the optical heating is too fast, and a stationary offset is added to the temperature profile. Therefore, the phase transition is not completely modulated anymore and the photothermal signal is not enhanced by the large change of the refractive index during the phase transition.

To optimally use the nematic–isotropic phase transition for the signal enhancement one is required to heat to sample as close to the phase transition temperature as possible. Then a tiny optical heating of an absorber would drive the phase transition. In this case, one can make use of the large refractive index change upon heating. But the heating power supplied to drive the phase transition is very small. Therefore, it takes very long to complete the phase transition. In this case, modulation frequencies, as typically used in photothermal microscopy, are not accessible if high enhancement factors shall be used. Therefore, the ultimate limitation of the signal enhancement is the latent heat transformed in the nematic–isotropic phase transition.

A solution to this limitations is the use of a different system such a xenon. Supercritical xenon changes its density and thereby the refractive index considerably.[129] The use of a supercritical fluid circumvents the nucleation processes present in liquid–gas phase transitions which are highly nonlinear and difficult to control. The photothermal signal can be enhanced by a factor of about 500 compared to glycerol.[130] Using the signal enhancement in xenon simultaneous observations of absorption and fluorescence provided new insight into the photophysics of conjugated polymers.[32] Finally, the use of nanometer-sized bubbles is another route to achieve large photothermal signals at extreme conditions and are also of fundamental interest.[131] Their applications include superresolution photothermal imaging.[132]

Chapter 3

Experimental and Theoretical Prerequisites

The present chapter will discuss experimental and theoretical techniques used during the thesis. It will discuss details on the sample preparation, lock-in detection, the experimental setup, the numerical calculations and the polarization contrast measurements.

3.1 Sample Preparation

All samples are produced on top of BK7 glass substrates from Roth that undergo the following cleaning procedure. They are rinsed with acetone, ethanol and Millipore deionized water. After rinsing the substrates are dried with nitrogen. The substrates are treated for 1 min in an oxygen-nitrogen plasma at 2.5 mBar.

PDMS Samples Polydimethylsiloxane (SYLGARD 184 from Dow Corning), also called PDMS, is often used in microfluidics due to its homogeneity and transparency. The monomer is mixed at a ratio of ten to one with the curing agent and stirred well. This process induces air bubbles into the viscous mixture. Negative pressures at $1-10$ mBar remove the air bubbles. Then $100-200$ µl of the prepared liquid PDMS mixtures are dropped onto a cleaned coverslip which is placed on a spin-coater (Laurell WS-400B-6NPP) and spun to 8000 rpm. The coverslip remains at that velocity for approximately 20 s. The sample is cured in an oven for 25 min at 100° C. This procedure results in layer thicknesses of approximately 15 µm.
The cured sample is treated for 20 s in the plasma above. Then $20-30$ µl of gold nanoparticle solution are applied onto the sample. The sample is spun to 8000 rpm. The particle concentrations of the gold nanoparticle solutions are adapted depending on the particle size. For nanoparticles with 60 nm in diameter the stock solution is used having a concentration of about $2 \cdot 10^{10}$ particles per ml to get well separated particles in the sample. For smaller particle sizes the respective stock solutions are diluted to achieve particle concentrations that are comparable to the one above. During the course of the thesis gold nanoparticles with 10, 20, and 60 nm in radius from Nanopartz and BBI Solutions have been used. During the experiments, no influence of the manufacturer was observed.
After the spin-coating of the gold nanoparticles, the sample is dried for $2-5$ min in an oven at 100 °C to remove excess water. To embed gold nanoparticles in an homogeneous environment, a second PDMS layer is applied on top of the particles following the procedure described above.

Water Samples Gold nanoparticles at the interface are needed to spatially overlap both laser beams in the samples. Therefore, gold nanoparticles are covalently attached to the glass substrate using (3-Aminopropyl)trimethoxysilane called APTMS from Sigma-Aldrich. The preparation process is as follows.
Rinsed coverslips are additionally processed with a piranha solution containing sulphuric acid and hydrogen peroxide at a 1:1 ratio. The pyranha etching creates silanol groups at the glass surface enabling the bonding of APTMS. Pyranha solution and glass substrates are put into a Teflon vessel and treated in an ultrasonic bath for 20 min. Afterward, the samples are rinsed with Millipore and dried with nitrogen. The APTMS solution contains methanol and APTMS at a 9:1 ratio. The cleaned glass substrates are incubated for 30 min. The treated samples are rinsed with methanol and water to

remove access APTMS molecules. After drying with nitrogen and spin-coating of gold nanoparticles the samples are heated to $100\,^\circ C$ in an oven for 10 min to attach the gold nanoparticles covalently to the surface.

Having prepared the bottom coverslip, 20 µl solution containing nanoparticles dissolved in water are applied onto the substrate. A second coverslip is used as a cover. The resulting chamber is sealed with the PDMS monomer to prevent evaporation and evaporation induced flows. The samples can be used for several days and contain a liquid layer which is about 50 µm in thickness. To ensure single particle events in the experiments, the average volume occupied by a single particle is 300 to 1000-times larger than the focal volume of the detection laser

Liquid Crystal Samples The used liquid crystal is 5CB (4-Cyano-4'-pentylbiphenyl). The crystalline order is induced by surface alignment. Therefore, a saturated solution of PVA (Polyvinylalcohol, Sigma-Aldrich, 99% hydrolyzed) and water is prepared, and one which additionally contains gold nanoparticles. The solutions are spin-coated onto a cleaned coverslip at 3000 rpm. Then the cover slip coated with PVA only is unidirectionally rubbed using Thorlabs Webril Handi-Pads. This approach creates untwisted samples. If both cover slips are rubbed the liquid crystal films are always slightly twisted due to the manual rubbing. To achieve different layer thicknesses, a chamber is formed where the coated surfaces face each other having aluminum foil as a spacer on one side. The chamber is filled with 2 µl of liquid crystal by capillary forces.

3.2 Lock-in Detection

A lock-in detection is used to extract signals at a frequency f. The noise can be much larger than the signal $s(t) = \Phi\cos(2\pi f t + \delta)$ with the phase delay δ and the amplitude Φ. The signal is multiplied with a reference signal $r_{\cos}(t) = V_{\mathrm{ref}}\cos(2\pi f_{\mathrm{ref}} t + \theta_{\mathrm{ref}})$ that has a certain reference phase delay θ_{ref} and frequency f_{ref},[133]

$$\Phi'_{\cos} = V_{\mathrm{sig}} V_{\mathrm{ref}} \cos(2\pi f t + \delta)\cos(2\pi f_{\mathrm{ref}} t + \theta_{\mathrm{ref}}) \tag{3.1}$$

$$= \frac{1}{2} V_{\mathrm{sig}} V_{\mathrm{ref}} \cos([2\pi f - 2\pi f_{\mathrm{ref}}]t + \delta - \theta_{\mathrm{ref}}) + \tag{3.2}$$

$$\frac{1}{2} V_{\mathrm{sig}} V_{\mathrm{ref}} \cos([2\pi f + 2\pi f_{\mathrm{ref}}]t + \delta - \theta_{\mathrm{ref}}). \tag{3.3}$$

The following lowpass filtering removes the high-frequency component at the frequency $f + f_{\mathrm{ref}}$. Depending on $f - f_{\mathrm{ref}}$ a low frequency component might remain if the time constant of the lowpass filter is smaller than $1/(f - f_{\mathrm{ref}})$. Only signals very close to f_{ref} are detected. The bandwidth of the filtering depends on the time constant of the lowpass filter. If $f = f_{\mathrm{ref}}$ the in-phase signal is

$$\Phi_{\cos} = \frac{1}{2} V_{\mathrm{sig}} V_{\mathrm{ref}} \cos(\delta - \theta_{\mathrm{ref}}). \tag{3.4}$$

The out-of-phase signal is then

$$\Phi_{\sin} = \frac{1}{2} V_{\mathrm{sig}} V_{\mathrm{ref}} \sin(\delta - \theta_{\mathrm{ref}}). \tag{3.5}$$

If the optimal performance of the lock-in amplifier without perturbations shall be reached, different aspects have to be considered.[133][a] In the ideal case, the present noise is purely white. In practical situations, periodic background signals are minimized as much as possible.
Amplitude and phase delay are calculated from the phase sensitive signals via

$$\Phi = \sqrt{\Phi_{\cos}^2 + \Phi_{\sin}^2} \tag{3.6}$$

$$\phi = \arctan\left(\frac{\Phi_{\sin}}{\Phi_{\cos}}\right). \tag{3.7}$$

If the signal is purely harmonic like $s(t)$, first-order Fourier components are identical to the multiplication of signal and references:

$$\begin{pmatrix} \Phi_{\sin} \\ \Phi_{\cos} \end{pmatrix} \propto f \int_0^{1/f} \begin{pmatrix} \sin(2\pi f t) \\ \cos(2\pi f t) \end{pmatrix} s(t)\mathrm{d}t. \tag{3.8}$$

This approach is used to calculate the phase sensitive signals from numerical calculations of time-harmonic signals.

3.3 The Photothermal Microscope

The photothermal setup is home-built and adapted to the use of different contrast mechanisms. In all situations, one point is imaged at a time and images are obtained by moving laser beams and sample relative to each other.

3.3.1 Measuring Photothermal Signals

The transmission change upon heating is typically in the order of $10^{-4}\,\mathrm{K}^{-1}$. As the temperature profile for nanometer-sized absorbers is established within fractions of a microsecond a modulated detection scheme is applied. The intensity of the heating laser is harmonically modulated by an acousto-optic modulator at frequencies of $1-2000\,\mathrm{kHz}$. The modulation of the heating laser results in a modulation of the detection laser which is orders of magnitude smaller than its overall signal. To measure the modulation amplitude, which is the photothermal signal, the photodiode signal is fed to a lock-in amplifier.

3.3.2 Photothermal Microscope

The photothermal setup consists of two different laser beams. The heating laser at 532 nm is a Coherent Verdi V-5 operated at 1 W. A beam splitter reflects 10% of the output and a 500 mm lens focuses the light into the active region of an acousto-optic modulator (Isomet 1206C or Isomet 1260C). The modulation is controlled either by a function generator (Fluke and Philips PM5138) or a lock-in amplifier (Signal Recovery 7280). The beam of light is collimated by a 400 mm lens. In the next step the beam of light is expanded using a telescope with 60 mm and 100 mm lenses. Spatial modes other than TEM 00 are filtered by a 20 µm pinhole. The heating laser is co-aligned with the detection laser using

---

[a] Manual for the lock-in amplifier Signal Recovery DSP7280 http://ameteksi.com/-/media/ameteksi/download_links/documentations/7280/190398-a-mnl-d.pdf

a dichroic mirror. Typically heating powers of 1 µW to 2 mW are used and tuned by a continuously variable neutral density filter wheel.

The detection beam of light is provided by a Coherent ULN laser diode at 635 nm. It has a very stable power output and shows low fluctuations at frequencies between 10 Hz and 10 MHz. However, the laser light is pulsed at a repetition rate of 170 MHz. The beam of light is spatially expanded in a telescopic system having a 19 mm and a 200 mm lens and is spatially filtered by a 30 µm pinhole.

After both beams of light are co-aligned at the dichroic mirror, the illumination objective (Olympus UPlanSApo 100x, NA=1.4, oil immersed) focuses the laser beam into the sample. The laser beams overfill the back aperture of the objective. A piezo stage (Physik Instrumente P-517.3CL) controls the sample position and enables sample scanning to obtain images. LabVIEW and a real time processing unit (Jäger Messtechnik Adwin-Gold) control the positions of the piezo stage and manage the data acquisition including digitization of the analog measurement signals.

In the following the used configurations in the detection path are described, which differ depending on the measurement of transmission images, photothermal lensing, deflection, and polarization contrast.

Transmission Microscopy The transmission images of single gold nanoparticles are used to validate that the laser beams are well co-aligned, meaning that both laser beams are positioned central and perpendicular in the back-aperture of the illumination objective and overlap in the object plane. A dry objective (Olympus MPlanFLN 50x, NA=0.8) collects the transmission. The laser beams are split by a dichroic mirror and imaged onto different photodiodes (Thorlabs PDA36A). The Adwin-Gold digitizes the analog photodiode signals. It is important to use relatively low powers of the heating laser as the optical heating can alter the transmission. The signal to noise ratio of the heating laser can be enhanced by intensity modulation and subsequent demodulation using the lock-in amplifier.

Photothermal Lensing Single particle photothermal lensing detects the change of divergence of a detection laser beam which is caused by an optically heated nanoparticle. Photothermal lensing is detected by measuring the transmission through an aperture. Here, the aperture is already given by the detection objective (NA=0.8), which has a significantly smaller numerical aperture than the illumination objective (NA=1.4). As the refractive index change is typically in the order of $10^{-4}\,\mathrm{K}^{-1}$, a modulated detection scheme is implemented to enhance the signal to noise. The heating laser is intensity modulated at a frequency f, which causes a harmonic modulation of the detection if a particle is in focus of the heating laser. A lock-in amplifier measures the in-phase and out-of-phase signal with respect to the modulated optical heating (see fig. 3.1 (a)). The repeated comparison of the transmission of the detection laser when a particle is heated and not heated makes photothermal microscopy very sensitive. The shape of the photothermal lensing signal can be controlled by changing the distance between heating and detection laser beam foci.[26,28] The latter is achieved by moving lens L_I in the telescope of the heating laser.

The transmission of the detection laser is measured by a photodiode (Thorlabs PDA36A or Femto HCA-S-200M). The Thorlabs PDA36A is a variable gain silicon photodiode. It has a large detector size. If low harmonic distortion and constant amplification are of interest, a gain of 0db shall be used. The Femto HCA-S-200M offers a much smaller active area, low harmonic distortion, and constant amplification if operated below an output voltage of 1.2 V.

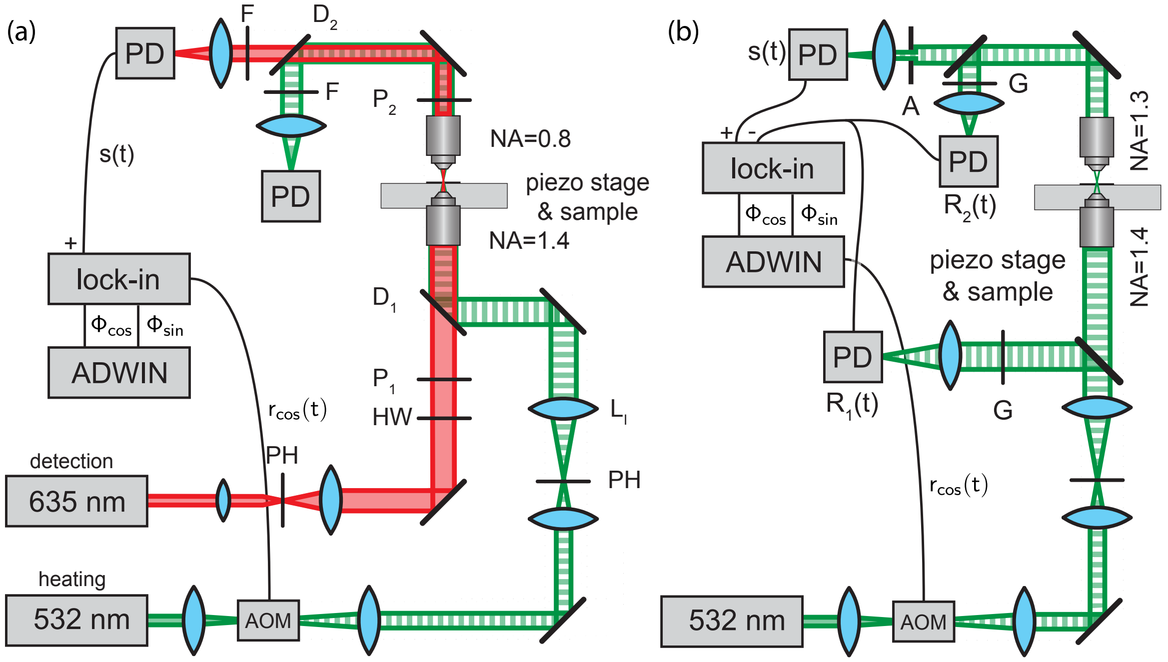

Figure 3.1: (a) The standard setup for photothermal lensing and transmission microscopy. Polarizers (P_1, P_2) and half-wave plate, required for polarization contrast, pinhole (PH), dichroic mirrors (D_1, D_2), interference filter (F), photodiode (PD), acousto-optic modulator (AOM). (b) Setup for single laser beam photothermal microscopy. The signal $s(t)$ is measured by a photodiode. References R_1 or R_2 can be subtracted from $s(t)$ to reduce the magnitude of the modulated signal. Thereby, the input amplification of the lock-in amplifier can be increased. The laser beams are attenuated by a grey filter (G) to match the power of the signal beam (S) which is spatially filtered by an aperture.

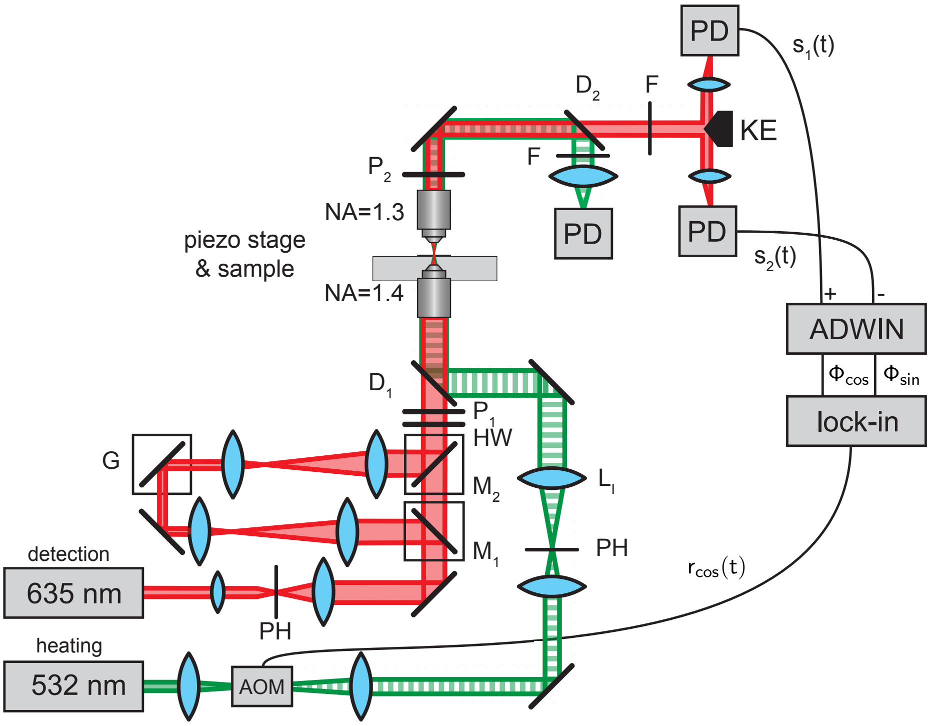

Figure 3.2: Setup for photothermal deflection. In the scheme of the setup two modes of operation are shown. For the usual photothermal deflection with particle scanning the two magnetic mirrors (M_1 and M_2) are removed. The probing of the extended thermal lens utilizes a laser scanning where the heating laser remains focused on the nanoparticle. The detection laser is raster scanned by a set of galvanometer scanning mirrors (G) to probe the extended thermal lens. Pinhole (PH), dichroic mirrors (D_1 and D_2), polarizers (P_1, P_2) and half-wave plate (HW) if required for example for the polarization contrast. The combination of right angle knife edge prims (KE) and photodiodes (PD) detects the deflection of detection laser in one direction.

Single Beam Photothermal Lensing Single Beam Photothermal microscopy is a variant of photothermal lensing which utilizes only a single laser beam to selectively detect absorbers (see fig. 3.1). The heating laser is intensity modulated at f with an additional offset. The laser power of the offset and the average of harmonically modulated power are approximately equal. The detected laser signal is fed to the lock-in amplifier which calculates in-phase and out-of-phase signals. The in-phase signal contains the scattering signal from the nanoparticle and the photothermal signal. The out-of-phase signal consists in principle solely of the photothermal signal. To reduce the modulation amplitude of the signal that has to be analyzed by the lock-in, the references R_1 or R_2 can be subtracted from the signal S (see fig. 3.1 (b)).

Polarization Contrast The polarization contrast is utilized to characterize samples where gold nanoparticles are embedded into a liquid crystal matrix. The detection is polarized with a nanoparticle linear film polarizer. A half-wave plate is placed in front of the polarizer to maximize the power of the polarized light. Due to technical reasons a dichroic mirror, a silver mirror and two objectives are placed between analyzer and polarizer. Therefore, the contrast between parallel and perpendicular polarizer configurations is only about 100:1. If the polarization is purely s or p polarized at the optical elements, the contrast between parallel and perpendicular polarizers is higher. The measurement is performed with the detection laser only. The signal of the detection laser is directly recorded by the Adwin-Gold.

Photothermal Polarization Contrast Upon optical heating of a nanoparticle the anisotropy of the liquid crystal decreases. Therefore, the polarization of the detection laser is changed upon optical heating. This microscope configuration is set like the polarization contrast with a co-aligned heating laser beam described above.

Photothermal Deflection Photothermal deflection detects the movement of the detection beam's center due to a heated particle. The transmission is detected with an objective (Olympus UPlan-FLM 100x, NA=1.3) that has a numerical aperture similar to the one of the illumination objective to minimize photothermal lensing. The transmission is split by a right angle prism and imaged onto two photodiodes (Thorlabs PDA36A, 0db). The photodiode signals are input to a lock-in amplifier and subtracted from each other. The lock-in output modulation amplitude and phase delay of the difference signal is caused by a harmonically heated particle.

Probing the Extended Thermal Lens To probe the extended thermal lens via photothermal deflection, the probing laser has to be steered independently on the heating laser. Therefore, the beam path of the detection laser is altered and a set of galvanometer mirrors (Thorlabs GVS012) is added (see fig. 3.2). The beam expander of the detection laser beam is modified by changing the focussing lens to 60 mm and the collimating one to 200 mm to underfill the illumination objective. To utilize laser scanning, the laser beam has to be rotated around the back focal plane of the illumination objective. This is achieved by putting, for example, a 4f system between galvanometer scanning mirrors and the illumination objective. This way the rotation by the mirrors is imaged into the back aperture without shifting the lateral position of the laser beams. The rotation around the back aperture shifts the focus position in the object plane.

To achieve the optimal resolution and range of the laser scanning a telescope with a 400 mm and a 60 mm lens are placed in front of the scanning mirror. Behind galvanometer scanning mirror, the 4f system above is replaced by a telescope having a 60 mm and a 300 mm lens. The distances between all the lenses and the lenses themselves are chosen according to the algorithm developed by Fällman and Axner.[134]

Amplification of the Photodiodes As the frequency dependence of the photothermal signal's amplitude and phase delay are of particular interest, the amplification of the photodiodes has to be constant over the whole frequency range, and the phase measurement should not suffer from harmonic distortions. In figure 3.3 the frequency dependence of the measured modulation amplitudes is plotted against the modulation frequency. This relationship is heavily affected by the amplification. At 20db the amplification of the incident light increases slightly with modulation frequency up to 300 kHz and decreases afterward due to its bandwidth of 1 MHz (see fig. 3.3 (left)).[a] At 10db the detected signal amplitude increases by a factor two from 10 kHz to 2 MHz. At 0db amplification the detection

---

[a] Manual for the photodiode Thorlabs PDA36A https://www.thorlabs.com/drawings/abf41200f5b4afe2-02C8E42C-5056-0103-79ED767FCEF2B44F/PDA36A-Manual.pdf.

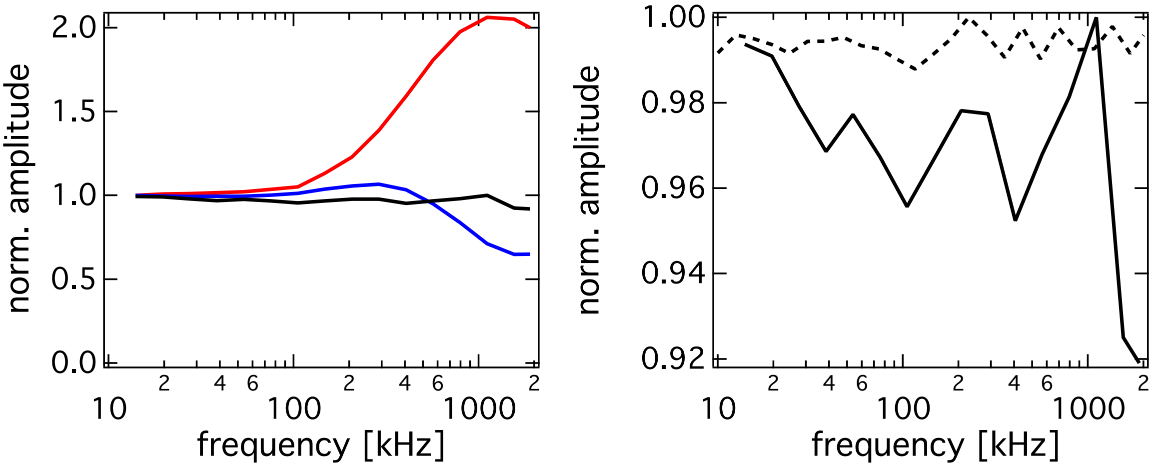

Figure 3.3: The heating laser is intensity modulated and its transmission is detected by a photodiode. The photodiode signal is input to the lock-in amplifier that measures the modulation amplitude. (left) shows the modulation amplitude for a frequency sweep for different amplifications of the photodiode Thorlabs PDA36A at 0db (black), 10db (red) and 20db (blue). (right) modulation amplitude for Thorlabs PDA36A at 0db (solid line) and Femto HCA-S-200M (dashed line).

modulation amplitude is constant and fluctuates by about 4%. At 0db and 20db the performance of the photodiode is acceptable. The amplification of 10db will not be used.
According to the manual the Femto HCA-S-200M provides low harmonic distortion and linear amplification if the photodiode signal is below 1.2 V.[a)] The photodiode output is monitored with an oscilloscope and the laser power is adjusted with a grey filter wheel in front of the detector. The amplification of the photodiode is constant over the whole frequency regime with deviations that are smaller than 1% (see fig. 3.3 (right)).

3.4 Numerical Electromagnetic Calculation

Here, details on the numerical electromagnetic calculations are given. The calculations are based on a generalized Lorenz–Mie theory that solves Maxwell's equations for spherical symmetric refractive index profiles and arbitrarily shaped laser beams.[26,118] The situation of interest here is a spherical gold nanoparticle that is surrounded by a refractive index generated by a thermal wave (see eq. 2.31). The implementation was done by M. Selmke who improved scattnlay[120] from incident plane waves to arbitrarily shape laser beams.
The implementation has three different layers. Layer 1 is a c-program which takes the beam shape parameters and the parameters characterizing the layers. The most important outputs are the extinction, scattering, and absorption efficiency factors which allow the calculation of the respective cross sections. An Igor Pro script generates the inputs for the c-program, starts the calculation and reads the command line output. This is the second layer which calculates the transmission signal for one

---

[a)] Manual for the photodiode Femto HCA-S-200M-SI `http://www.femto.de/images/pdf-dokumente/de-hca-s-200m-si_r10.pdf`.

pixel and one time instance. Layer 3 batches layer 2 to obtain images and photothermal images at different time instances.

3.5 Optical Characterization of Liquid Crystal Domains

Here, the aim is to measure the orientation of the principal axes Ψ_D, retardation $\beta' = \frac{\pi(n_\parallel - n_\perp)d}{\lambda}$ and twist angle ϕ of the liquid crystal films. The retardation quantifies the phase delay between light that is parallel and perpendicular polarized to the director. The twist angle is the angle between the directors at the two interfaces inducing ordered liquid crystal domains.

The nematic liquid crystal film changes the polarization of the incident linearly polarized light. Taking a second polarizer the change of polarization results in a transmission change which is detected by a photodiode. The measurement is performed twice for each orientation. First polarizer and analyzer are set parallel and then perpendicular to each other measuring the corresponding transmissions I_s and I_p to guarantee the normalization $1 = I_\mathrm{s} + I_\mathrm{p}$. Linear polarized light that is incident on the liquid crystal film and an analyzer measure the polarization change[135]

$$I_\mathrm{p} = \left[\cos\gamma\cos\phi + \frac{\phi}{\gamma}\sin\gamma\sin\phi\right]^2 + \left[\frac{\beta'}{\gamma}\sin\gamma\cos\left(2\zeta - \phi - 2\Psi_D\right)\right]^2, \tag{3.9}$$

$$I_\mathrm{s} = \left[\cos\gamma\sin\phi - \frac{\phi}{\gamma}\sin\gamma\cos\phi\right]^2 + \left[\frac{\beta'}{\gamma}\sin\gamma\sin\left(2\zeta - \phi - 2\Psi_D\right)\right]^2, \tag{3.10}$$

where $\gamma = \sqrt{\phi^2 + \beta'^2}$, and ζ is the orientation of the polarizers. The measurement is performed for $10 - 15$ different orientations of the polarizer. I_p and I_s are invariant under the transformations $\zeta \to \zeta \pm \pi/2$, which makes it impossible to distinguish ordinary and extraordinary axis of the LC, and $\phi = \pi/2 \to \phi = -\pi/2$.[135] Ordinary and extraordinary axis can be identified with the help of the photothermal signal.

Chapter 4

Results and Discussion

The following chapter constitutes the main part of the cumulative dissertation. The purpose of thesis is to show that single nanoparticle can be utilized as probes for thermal transport and actuators in the sample.

4.1 Thermal Diffusivity Measured Using a Single Plasmonic Nanoparticle

Abstract

A method to measure the thermal diffusivity around a single heated gold nanoparticle is presented. It is based on photothermal single particle microscopy and employs the phase delay of a temperature modulation due to the finite thermal diffusivity. The phase delay is detected optically averaging over the focal volume of a diffraction limited beam of light. The thermal diffusivity is extracted by comparison to electromagnetic scattering calculations of the photothermal signal. Measurements in the solid (polymer) and liquid (water) are presented and compare well with literature data. The method paves the way for extended measurements of nondiffusive and heterogeneous heat transport in complex media.

The Section is based on the following article **A. Heber**, M. Selmke, F. Cichos. *Thermal diffusivity measured using a single plasmonic nanoparticle*, Phys. Chem. Chem. Phys. **105**:2, 065428 (2015) is published by the PCCP Owner Societies under CC BY 3.0. The article has been adapted. Details on the author contributions are given in the appendix 6.4.

The understanding of thermal transport processes has greatly benefitted from numerous methods that measure heat transfer close to surfaces or of macroscopic samples. The general principle behind these measurements is that a thermal perturbation is induced and then monitored. The temporal evolution of this thermal perturbation is a reporter for the thermal diffusivity. There are many different methods that implement this principle. Using the 3ω method a metallic wire acts as the heating and temperature probe at the same time.[95] Other methods apply a delta-like heating by a pulsed laser to an absorbing surface[5,136,137] or particles[7,8] and then measure transient reflectance or absorption that are related to temperatures using a delayed probe laser pulse. Scanning thermal microscopy[10] probes temperatures directly and measures thermal conductivities at high spatial resolution, but requires physical contact with the probe. Recently, surface plasmon resonance shifts of single gold nanoparticles have been used to quantify the average thermal conductivity at an interface.[52] Macroscopic thermal lensing can be utilized to measure thermal diffusivities in solids,[138] liquids and colloidal suspensions.[139]

In this paper, we demonstrate the capabilities of quantitative single particle photothermal (PT) microscopy[26–28] to assess thermal diffusivities locally within a medium using far-field optical readout. This is not possible with most other methods apart from transient absorption[7,8] which employs picosecond pulsed lasers and thermal lensing microscopy.[138] Thermal diffusivity measurements using PT microscopy will enable the study of thermal transport in samples where gold nanoparticles are already used as tracers[42] or for local temperature manipulations.[140]

PT microscopy is a versatile method to study absorbing particles. This technique enables absorption measurements of single nanoparticles and single molecules,[31] imaging[41,42] as well as correlation spectroscopy, i.e. to investigate dynamics in solution.[44,48] The PT contrast originates from optically excited objects that dissipate their thermal energy into the surrounding medium as heat. Around these nanosources of heat, a temperature profile is created that brings about a refractive index change due to thermal expansion. As the photothermally induced transmission change is small as compared to the overall transmission a lock-in detection scheme is put forward in which the heating laser is harmonically modulated.[53] The refractive index change is detected by a continuous wave laser in transmission demodulated by a lock-in amplifier. The amplitude of the PT signal has been shown to depend on the modulation frequency of the optical heating[43,53,138,141,142] due to a finite thermal diffusivity. Therefore, the frequency dependence of the photothermal signal contains information on the thermal transport property of the medium surrounding the nanoparticle. This feature can be used to selectively detect absorption using just a single laser beam.[142] To extract the thermal diffusivity from the frequency dependence of the PT signal it has to be modeled quantitatively. Attempts have been undertaken but have given unrealistic thermal diffusivities due to a simplified model[54] or the neglect of aberrations.[142] To make PT microscopy a quantitative method for the measurement of thermal diffusivities the PT signal is calculated for different modulation frequencies. The modeling starts with the calculation of the thermal transport around the harmonically heated gold nanoparticle leading to a refractive index profile. Afterward, the transmission signal of the detection laser as measured by a photodiode is determined.

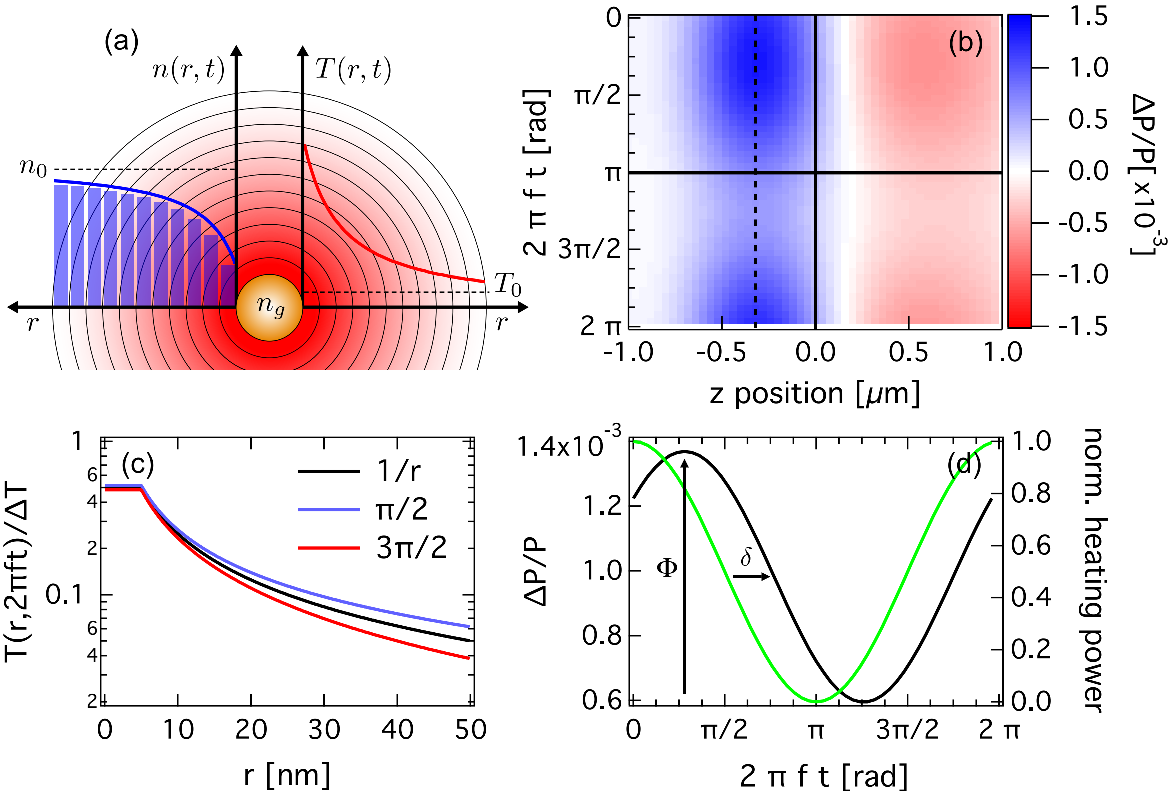

Figure 4.1: (a) Temperature and refractive index profile around a heated gold nanoparticle. (b) Calculated transmission signal change in the detector $\Delta P/P$ due to the presence of a harmonically heated gold nanoparticle ($R = 5\,\mathrm{nm}$) in PDMS. The nanoparticle is positioned on the solid vertical line at $z = 0$. The relative transmission change $\Delta P/P$ is shown for different displacements between nanoparticle and laser foci along the optical axis (z-position) at different time instances during one modulation cycle $2\pi f t$. The blue color encodes an enhanced transmission due to the optically heated nanoparticle and a red one a decrease. Dashed line: the position of the maximal signal. Horizontal line: heating is turned off. The thermal diffusion length is 150 nm. (c) Comparison of the temperature profiles when the heating power is decreasing (blue) or increasing (red) to the case with continuous heating. (d) Transmission profile for the dashed line in (b) for one heating period (black). Normalized power of the heating laser (green). The vertical arrow indicates the amplitude Φ of the photothermal signal and the horizontal one the phase delay δ between the optical heating and the detection signal.

4.1.1 Numerical Calculations

The gold nanoparticle is excited at its plasmon resonance and dissipates the excitation energy as heat into its surrounding medium which increases the temperature locally. An analytical solution for the thermal transport of a harmonically heated sphere has recently been derived.[86] It includes the heat capacity of the nanoparticle as well as interfacial thermal resistances. However, in our experiments, the mentioned contributions are negligibly small. Only at modulation frequencies f larger than 10 MHz the heat capacity of the nanoparticle starts to show an effect on the temperature profiles. To see an effect on the interfacial thermal resistance modulation frequencies of more than 100 MHz have to be used. For those reasons the time dependent temperature profile $\Delta T(r,t)$ was derived in the appropriate limit based on the theory of Berto et al.[86] retaining the finite particle size only

$$N = \sqrt{(R/R_{\text{th}})^2 + (1 + R/R_{\text{th}})^2} \tag{4.1}$$

$$\psi(r) = \frac{r-R}{R_{\text{th}}} + \arctan\left(\frac{R/R_{\text{th}}}{1+R/R_{\text{th}}}\right) \tag{4.2}$$

$$\Delta T(r,t) = \Delta T \frac{R}{r}\left(1 + \frac{1}{N} e^{-\frac{r-R}{R_{\text{th}}}} \cos\left(2\pi f t - \psi(r)\right)\right). \tag{4.3}$$

Herein, ΔT is the temperature elevation in the steady state at the nanoparticle's surface, R its radius, $R_{\text{th}} = \sqrt{\alpha/\pi f}$ the thermal diffusion length and α being the thermal diffusivity of the medium which is the quotient of thermal conductivity divided by the volumetric heat capacity. The thermal diffusion length characterizes how far thermal energy is transported during one modulation cycle. The term N is a small correction to the amplitude of the temperature modulation and $\psi(r)$ its phase delay in a certain distance r from the center of the nanoparticle. Equation 4.3 is slightly more accurate for finite R as compared to the temperature profile of a point source[90] typically used in this context and does not contain any additional material parameters. The temperature profiles differ significantly from a purely one over distance dependence (see fig. 4.1 (c)). The temperature elevation alters the refractive index locally as

$$\Delta n(r,t) = \partial n_{\text{T}} \Delta T(r,t). \tag{4.4}$$

The thermorefractive coefficient ∂n_{T} quantifies the refractive index change with temperature. At an instance, the gold nanoparticle is surrounded by a radially symmetric refractive index profile that is modulated in time being induced by the harmonically modulated heating laser. The situation is sketched in fig. 4.1 (a). The PT signal depends on the exact shape of the non-absorbed detection laser beam as it averages over different $\psi(r)$. The two laser beams are co-aligned using their scatter images and focused by an oil-immersed objective (NA=1.4). Their transmission is collected by a dry objective (NA=0.8). The peak intensities of both laser beams have no displacement in any spatial dimension. The aberrations caused by the high NA objectives significantly alter the intensity distributions, which needs to be taken into account when modeling the photothermal signal.

The transmission signal of the non-absorbed laser beam as detected by a photodiode is computed utilizing a generalized Lorenz–Mie theory[26,143] for the gold nanoparticle and the time-dependent temperature profile calculated using eq. 4.3. This step is repeated for different positions of the laser foci with respect to the nanoparticle and times during the heating cycle. The results of such a calculation are displayed in fig. 4.1 (b). The image shows the variation of the transmission signal due to the modulated heating power and the nanoparticle at each position z along the optical axis. The nanoparticle is positioned at $z = 0$. A dispersive lensing signature is found when moving the particle along the optical axis. This signal is on top of the transmission signal of the nanoparticle without the refractive index profile.[143] For particles smaller than 3 nm in radius this contribution disappears, and a clear dispersive signal due to the refractive index profile is observed. More importantly, the plot in fig. 4.1 (b) is not symmetric with respect to the horizontal line. This is due to the fact that if the optical heating of the nanoparticle is turned off the thermal energy is not instantaneously dissipated into the surrounding medium. This results in a phase delay δ of the detected signal with respect to the optical heating. Figure 4.1 (d) shows the time-dependent transmission signal when the detection laser focus and nanoparticle are displaced by $z = -320\,\mathrm{nm}$ which also corresponds to the solid vertical line in fig. 4.1 (b) and to about one Rayleigh range. Here the transmission signal due to the nanoparticle is extremal. Phase delay δ and amplitude Φ of the PT signal for each position z in fig. 4.1 (b) are determined by calculating the fundamental Fourier components of transmission profiles as in fig. 4.1 (d).

4.1.2 Experiments

We record the PT signal for single gold nanoparticles in a polymer matrix (Polydimethylsiloxane - PDMS; SYLGARD 184 from Dow Corning). Heating and detection laser are co-aligned and focused onto single gold nanoparticles (Nanopartz, $R = 5\,\mathrm{nm}$). The detection power was adjusted to $P_\mathrm{d} = 1.9\,\mathrm{mW}$ at the wavelength $\lambda_\mathrm{d} = 635\,\mathrm{nm}$ and the heating power to $P_\mathrm{h} = 0.9\,\mathrm{mW}$ at $\lambda_\mathrm{h} = 532\,\mathrm{nm}$. The transmission signal of the detection laser is recorded using a photodiode. The modulated transmission signal is analyzed using a lock-in amplifier resulting in two different components one being in-phase Φ_cos and the other one being out-of-phase Φ_sin with the modulated optical heating. The latter two correspond to the fundamental Fourier components mentioned in a paragraph before. Further details on the experimental implementation have previously been reported in Ref. [26]. The signal to noise ratio of the PT signal is around 40 for accumulation times of 20 µs. The relations

$$\Phi = \sqrt{\Phi_\mathrm{cos}^2 + \Phi_\mathrm{sin}^2} \tag{4.5}$$

$$\delta = \arctan(\Phi_\mathrm{sin}/\Phi_\mathrm{cos}) \tag{4.6}$$

are used to calculate the amplitude of the photothermal signal Φ and its phase delay δ with respect to the heating δ marked in fig. 4.1 (d). In this study the amplitude of the photothermal signal is normalized to the maximal observed amplitude at $f = 10\,\mathrm{kHz}$.

Measurement in the Solid Measurement results for the normalized amplitude of 62 different $R = 5\,\mathrm{nm}$ sized gold nanoparticles in PDMS are shown in fig. 4.2 (a). Each data point is averaged over 0.8 s giving a SNR of approximately 10^4. The measurements were performed twice on every nanoparticle at modulation frequencies f between 10 kHz and 2 MHz. The amplitude of the PT signal saturates for low f and decreases with increasing frequencies (see fig. 4.2 (a)). This behaviour is observed for all particles.

The recorded signal amplitudes vary significantly from particle to particle (see fig. 4.2 (c)), which can be explained by the proportionality of Φ to the particle's volume. From the standard deviation of the normalized amplitude being 40% one can conclude that the size dispersion of the nanoparticles is in the order of 12%, which is in agreement with the value given by the manufacturer being 10%.

The phase delays δ of different particles are shown in fig. 4.2 (b) as a function of the modulation frequency. The phase delay increases with the modulation frequency. At low modulation frequencies, the temperature profiles show a one over distance dependence from the nanoparticle where only the amplitude is modulated. Therefore, the phase delay is very small. At higher f the temperature modulation is diminished, and the phase delay increases. The phase delay for very high frequencies will saturate at a finite value. A temperature profile that is constant in time with a one over distance

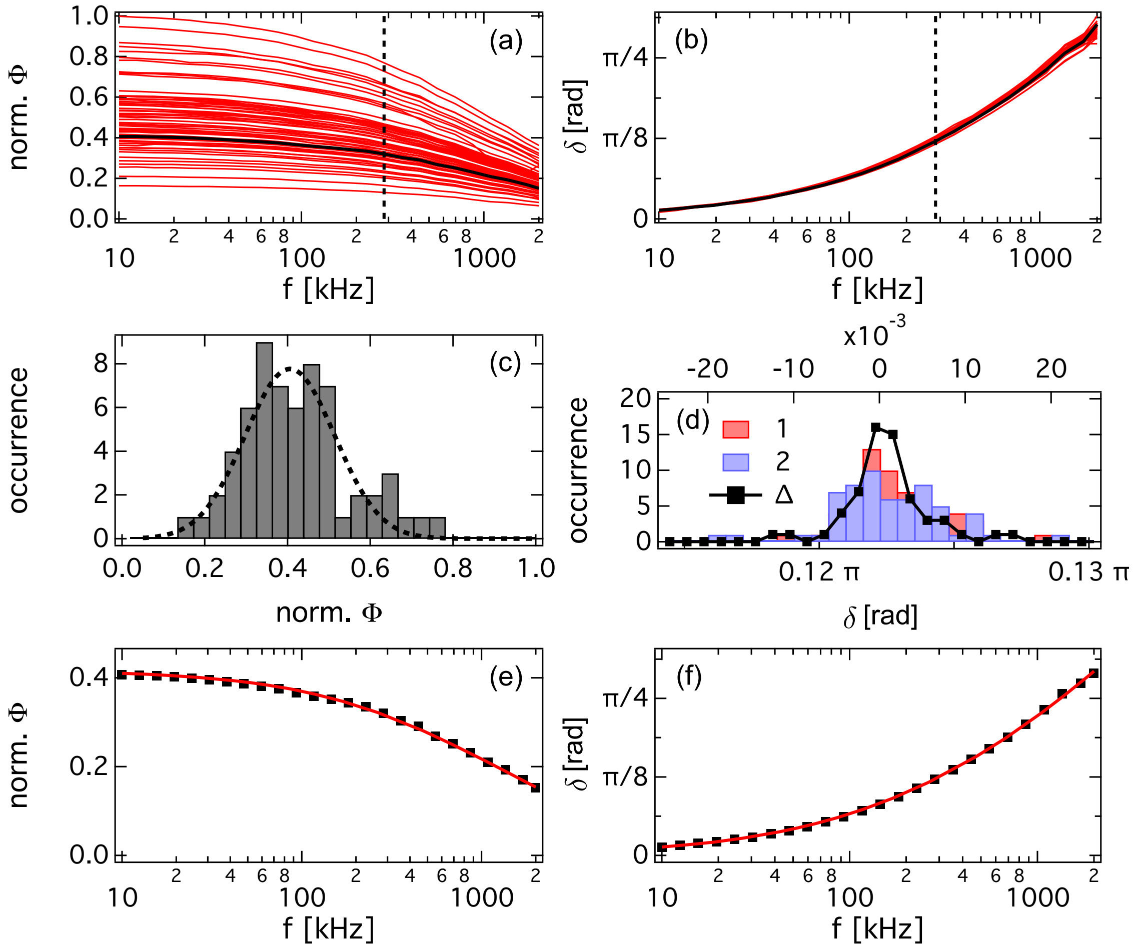

Figure 4.2: (a) PT amplitude normalized to the maximal amplitude at $f = 10\,\mathrm{kHz}$ and (b) phase delay as a function of the modulation frequency. The graph shows the results for one acquisition of 62 different nanoparticles. At the dashed line $f = 284\,\mathrm{kHz}$. (c) Histogram of different photothermal signal amplitudes at 284 kHz. (d) Histogram of phase delays at 284 kHz measured in two different acquisitions (bars) as well as a histogram of their difference (line and markers). For the black colored graph in (a) and (b) the corresponding fits are depicted in (e) for the amplitude and (f) for the phase delay. Both fits give a thermal diffusivity of $\alpha = 1.33 \cdot 10^{-7} \mathrm{m}^2\mathrm{s}^{-1}$.

dependence is retained. At one particular modulation frequency f the spread of δ is much lower as compared to the spread of the normalized amplitude (see fig. 4.2 (c) and (d)). The variance of δ for all measurements is comparable to the variance in case the difference between two measurements of the same particle is taken. Therefore, we were not able to detect any heterogeneities in the sample concerning the thermal transport which is an expected result. In fig. 4.2 (e) and (f) the results of the numerical calculation are scaled to δ and Φ for one measurement. The scaling factor is directly proportional to the thermal diffusivity. The numerical results fit the experimental ones in their frequency dependence very well.

At a fixed heating power we are able to see the expected proportionality between the signal amplitude Φ and the particle's volume.[26] This allows us to test whether the size dispersion has an influence on the phase delay by correlating δ and Φ at modulation frequencies of 284 and 355 kHz (see fig. 4.3 (c)). The Pearson correlation coefficients of about -0.2 indicate that both quantities are only weakly correlated (see fig. 4.3 C). The scatter of the measured phase delays and thereby of the thermal

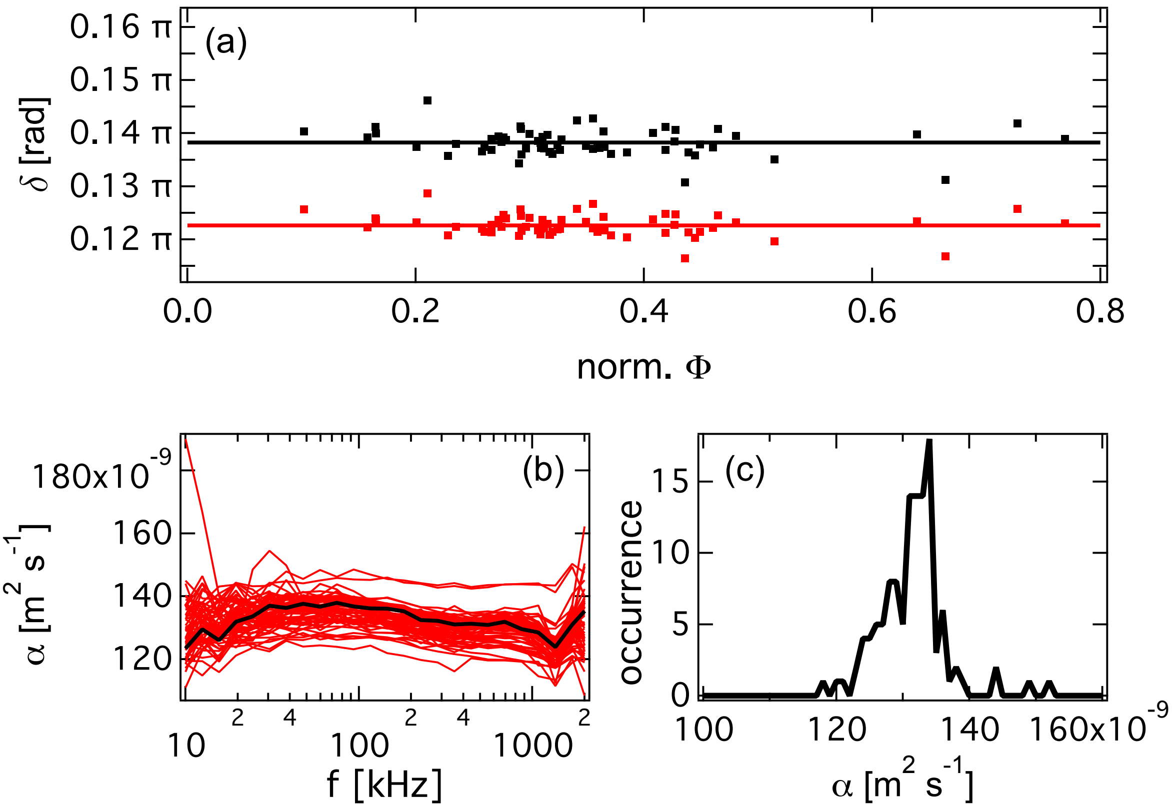

Figure 4.3: (a) Phase delay plotted against the normalized amplitude at the modulation frequencies $f =$ 284 kHz (red) and $f = 355$ kHz (black). The Pearson correlation coefficients are -0.16 and -0.20 respectively. The solid lines mark the average phase delays. (b) The thermal diffusivity as determined from the phase delay at every measured frequency. The black colored data set has already been discussed in detail in fig. 4.2 (e) and (f). (c) Average thermal diffusivities are depicted as a histogram for every particle and measurement. The average thermal diffusivity is $\alpha = (1.3 \pm 0.1) \cdot 10^{-7} \mathrm{m}^2\mathrm{s}^{-1}$.

diffusivities in fig. 4.2 (d) and 4.3 (a), (b) stem from the positioning error of the nanoparticle in the laser foci. A positioning uncertainty of the nanoparticle in the co-aligned laser foci of 30 nm perpendicular to the optical axis and 80 nm along the latter results in a change in the phase delay of $1.5 \cdot 10^{-2}$ rad at $f = 284$ kHz corresponding to an error of 8% in the thermal diffusivity.

For the determination of the thermal diffusivity, the measurement of the phase delay δ at a single modulation frequency should in principle suffice as the phase delay is independent of the heating power and the dependence on the particle's size is negligible as compared to the statistical errors. Therefore, the thermal diffusivity is determined by comparing the experimentally determined phase delay δ to the calculation. The thermal diffusivity measured using this procedure is shown in fig. 4.3 (b). The thermal diffusivities averaged over all modulation frequencies are shown as a histogram in fig. 4.3 (c). The average thermal diffusivity is determined with $(1.3 \pm 0.1) \cdot 10^{-7} \mathrm{m}^2\mathrm{s}^{-1}$. The thermal diffusivities as measured by photothermal microscopy agree well with macroscopic measurements performed in a laser flash apparatus (LINSEIS LFA 1000) giving $(1.30 \pm 0.02) \cdot 10^{-7}\,\mathrm{m}^2\mathrm{s}^{-1}$. The thermal diffusivity still shows a small systematic dependence on the modulation frequency (see fig. 4.3 (b)) likely for the reason that the aberrations are not perfectly captured by our numerical calculations.

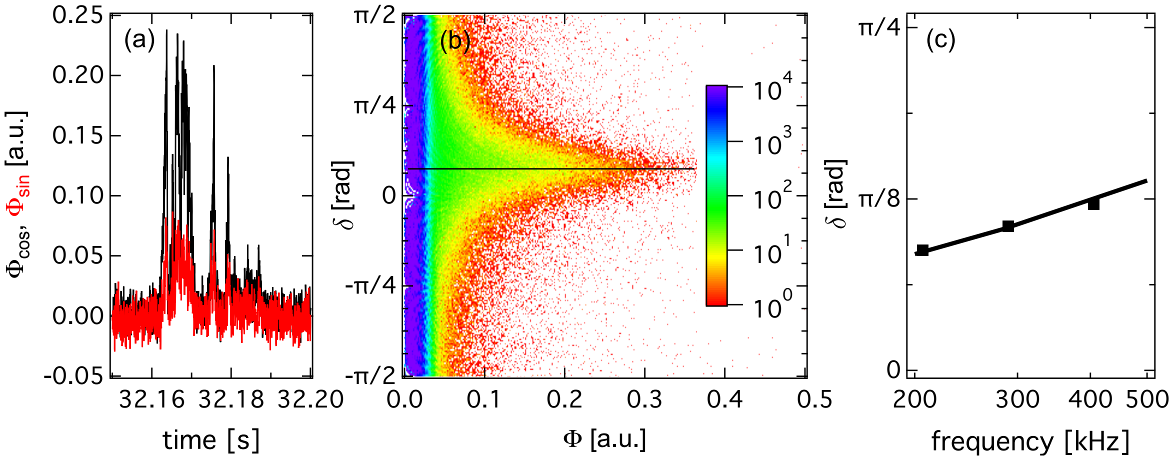

Figure 4.4: (a) The time trace of $\Phi_{\cos}$ (black) and $\Phi_{\sin}$ (red) is shown for a representative burst event. (b) Occurrence of the simultaneous measurement of phase delay and amplitude at $f = 206\,\mathrm{kHz}$. The average phase delay as extracted from the 2D histogram is plotted in (c). Experimentally measured (squares) and numerically calculated phase delays (solid line).

Measurement in the Liquid So far it has been demonstrated that PT microscopy can be extended to study thermal diffusivities in solids. In solids, the two co-aligned laser beams are focused onto an immobile particle, and phase delays are recorded during frequency sweeps at the position where the PT amplitude is maximal. In solution, gold nanoparticles perform Brownian motion, and signal bursts are recorded whenever a particle passes the detection focus (see fig. 4.4 A). Therefore, gold nanoparticles ($R = 30\,\mathrm{nm}$ in size; BBI Solutions) dissolved in water are put between two cover slips and sealed with silicon oil. The heating power is adjusted to $P_\mathrm{h} = 0.42\,\mathrm{mW}$ leading to a temperature increase at the particle's surface of maximal 50 K. The detection power is $P_\mathrm{d} = 1.7\,\mathrm{mW}$. The focal volume is approximately 500 times smaller than the average volume occupied by a single particle ensuring single particle signals. Again the two components of the PT signal are recorded namely the in-phase ($\Phi_{\cos}$, black) and out-of-phase ($\Phi_{\sin}$, red) components allowing the calculation of the PT signal's phase delay and amplitude. We create 2D histograms counting the number of 20 µs time bins having a certain amplitude and phase delay as in fig. 4.4 (b). The histogram is constructed from a 45 min long time series. The average phase delay is extracted as follows. From the histogram, line profiles are taken at a particular amplitude, and the average phase delay is extracted using a Gaussian fit. This procedure is repeated for all the amplitude bins. For large signal amplitudes Φ the phase delays are independent of Φ. The corresponding average phase delays are plotted for three different modulation frequencies in fig. 4.4 (c). The phase delays allow to extract the thermal diffusivity of water with $(1.4 \pm 0.2) \cdot 10^{-7}\,\mathrm{m^2 s^{-1}}$, which agrees very well with the literature value $1.43 \cdot 10^{-7}\,\mathrm{m^2 s^{-1}}$.

4.1.3 Conclusions

We have extended photothermal microscopy to measure thermal diffusivities with gold nanoparticles of a few nanometers in radius. The presented measurements can be conducted in every existing photothermal microscopy setup and employ the phase information, which is typically neglected. Our technique will enable spatially resolved thermal transport measurements for materials previously not accessible for example of plasmonic networks.[115,144] Based on these findings we will be able to measure anisotropic thermal diffusivities as well as latent heats. Heterogeneous and so far unexplored biological materials become accessible as well, but future studies have to investigate the spatial resolution of the thermal diffusivity measurement in detail. A thorough understanding of the frequency dependence of the photothermal signal has recently led to the selective detection of absorbing nanoparticles using a single laser beam.[142] The insights presented above can also contribute to a more detailed understanding of nanoscopic phase transitions.[131,145]

Acknowledgement We thank Felix Fahrnbauer for the laser flash measurements. We acknowledge financial support from the European Union and the Free State of Saxony, the DFG Forschergruppe ”From Local Constraints to Macroscopic Transport” and the graduate school BuildMoNa.

4.2 Thermal Diffusivities Studied by Single Particle Photothermal Deflection

Abstract

Using a fixed pump beam and a steerable probe beam, we image the thermal lens generated by a harmonically heated gold nanoparticle using photothermal deflection. In combination with a simple geometric optics model, we extract thermal diffusivities. The measurement technique is applied to reveal the anisotropic thermal conductivity of a nematic liquid crystal. As the measurement is highly local, it paves the way for applications in heterogeneous and anisotropic nanoscale thermal transport studies in complex biological systems.

Adapted with permission from **A. Heber**, M. Selmke, F. Cichos: *Thermal Diffusivities Studied by Single Particle Photothermal Deflection Microscopy*, ACS Phot. **4**:3, 681–687 (2017). Copyright (2017) American Chemical Society. Details on the author contributions are given in the appendix 6.4.

Single fluorescent molecules have become an indispensable tool for studying condensed matter systems and have provided many surprising insights[146] by measuring position, temperature, viscosity, orientation, and pH, among other properties, on the nanoscale.[147] They can access spatial and dynamic heterogeneities in these quantities, which is, in particular, powerful for biological studies. Single nonfluorescent absorbers can also be imaged sensitively and selectively using ground-state depletion microscopy,[110] spatial modulation spectroscopy,[148] interferometric detection,[149] and photothermal microscopy.[26,31,53] Absorbers are also able to manipulate their environment. Single optically heated gold nanoparticles are nanosources of heat, which can be used to manipulate biochemical processes,[140] control the propagation of light,[145] induce click chemistry,[150] catalyze urethane polymerization,[151] perform nanolithography[152] or grow nanostructures.[153] Especially for the latter two examples the effect of the plasmonic heating cannot be imaged optically requiring electron or atomic force microscopy to validate whether the experiment was successful. Changes in the thermal transport properties would indicate whether a reaction has taken place and the thermal transport in the nanostructures could be measured. The measurement of changes in the thermal transport enables the detection of caries,[154] molecular binding assays[155] and the detection of adlayers.[123] Thermal lensing can be used to identify tissues by their thermal diffusivity.[138] State-of-the-art techniques do not probe the thermal transport around single nanosources of heat, which might hinder the understanding of highly heterogeneous systems such as the coupling of gold nanorods to their environment.[78] Current techniques study thermal transport at interfaces, such as time-domain thermo-reflectance[6] and scanning thermal microscopy,[10] for macroscopic samples,[5] particle ensembles[7,156,157] as well as two- or four-contact transport measurements.[94]

In this paper, we extend photothermal deflection to study thermal transport in the environment of a single gold nanoparticle. The deflection signal originates from the heat-induced change of the refractive index of the medium surrounding the heat source. In the case of single particle photothermal microscopy, a single nano-object is excited at its absorption resonance. The excitation energy is dissipated as heat into its environment, establishing a localized temperature field. A refractive index field, also called a thermal lens (TL), is created, which alters the propagation of a second nonabsorbed detection laser beam. Here, we follow the heat flowing away from a single heated gold nanoparticle into space by characterizing the deflection of the detection beam interacting with the refractive index profile generated by the heated nanoparticle. The photothermal deflection probes the extended thermal lens, which directly allows the extraction of thermal diffusivities. It is analyzed by a simple geometric optics model. Using the two-dimensional information on photothermal deflection, we can extract the anisotropy of the thermal transport in the liquid crystal 4-Cyano-4’-pentylbiphenyl (5CB). The use of a single nanometer-sized particle will enable thermal transport studies in more complex samples and in situations where gold nanoparticles catalyze chemical reactions. Photothermal deflection will provide new ways to uncover heterogeneities in the thermal transport of complex and even biological samples.

4.2.1 Theory

To analyze the deflection of a probe laser beam by a refractive index profile, we calculate the refractive index change in the medium around a gold nanoparticle with a time-harmonic heating

$(1+\exp(i2\pi ft))$. The time-dependent heating at a frequency f allows a low noise lock-in detection on the experimental side[53, 108] but also provides the time scale for measuring heat propagation. The complex solution of the heat diffusion equation[90] gives the complex temperature rise at a certain distance r from a gold nanoparticle of radius R in a medium

$$\theta(t,r) = \Delta T \frac{R}{r} \left[1+\exp\left(i2\pi ft - k_{\text{th}} r\right)\right] \tag{4.7}$$

with a temperature increment ΔT_0 at the particle's surface. Equation 4.7 consists of a stationary term and a critically damped wave-like term with a complex wavenumber $k_{\text{th}} = (1+i)/R_{\text{th}}$.[158] The damping of the wave-like term occurs on a length scale of the thermal diffusion length $R_{\text{th}} = \sqrt{\alpha/\pi f}$. $\alpha = \kappa/C$ is the thermal diffusivity, κ and C being the thermal conductivity and heat capacity per unit volume, respectively. The above equation is only wave-like as the time-independent part transports the energy and not the wave-like time-dependent part.[91] Thermal conduction is thus distinct from energy transport by electromagnetic or acoustic waves. The complex spatially-dependent part $\exp(-ir/R_{\text{th}})$ is a spatial phase delay of the transient response, which will become important for the analysis of the experimental data.

The real part of the complex solution in eq. 4.7 readily yields the refractive index field when including the medium's thermorefractive coefficient $\partial_T n$ and the ambient refractive index n_0,

$$n\left(r,t\right) = n_0 + \Delta n \frac{R}{r} \left[1 + e^{-\frac{r}{R_{\text{th}}}} \cos\left(2\pi ft - \frac{r}{R_{\text{th}}}\right)\right]. \tag{4.8}$$

The refractive index contrast $\Delta n = (\partial_T n) P_{\text{abs}}/4\pi\kappa R$ of the thermal lens (TL) is determined by the absorbed power modulation amplitude $P_{\text{abs}} \propto \sigma_{\text{abs}} P_I$, σ_{abs} and P_I being the absorption cross section and the incident power modulation amplitude, respectively. Note that the refractive index at a certain distance is phase-delayed with respect to the optical heating by r/R_{th} due to the finite thermal diffusivity. The cosine in eq. 4.8 can be rewritten as the sum of two oscillating functions

$$\cos\left(2\pi ft - \frac{r}{R_{\text{th}}}\right) = \Phi'_{\cos} \cos\left(2\pi ft\right) + \Phi'_{\sin} \sin\left(2\pi ft\right). \tag{4.9}$$

The term $\cos\left(2\pi ft\right)$ represents the in-phase response to the optical heating, while the sine function describes the out-of-phase component. The latter arises due to the thermal diffusivity of the medium, which is reflected by its amplitude $\Phi'_{\sin} = \sin\left(r/R_{\text{th}}\right)$, which starts to become nonzero for distances larger than zero. Correspondingly, the in-phase component has to decrease as $\Phi'_{\cos} = \cos\left(r/R_{\text{th}}\right)$. The amplitudes of the time-oscillating functions are oscillating functions in space. Therefore, they show distinct maxima and minima on a length scale that is determined by the thermal diffusion length R_{th}. As the diffusion length depends on the inverse frequency f, the in- and out-of-phase components of the refractive index signal obey specific resonances for a well-defined distance r and frequency f.

To calculate the photothermal deflection from the time-dependent refractive index profile, we use a simple geometric optics model. Although we are in the limit of tightly focused beams, and accordingly wave optics is appropriate, we have shown in the past[29, 30] that geometric optics provides a good approximation as long as the offset of the probe beam b to the nanoparticle is large compared to the beam diameter of the probe beam. The signal is obtained from a geometric optics calculation of a light ray with the impact parameter b passing through the optically inhomogeneous medium, acting

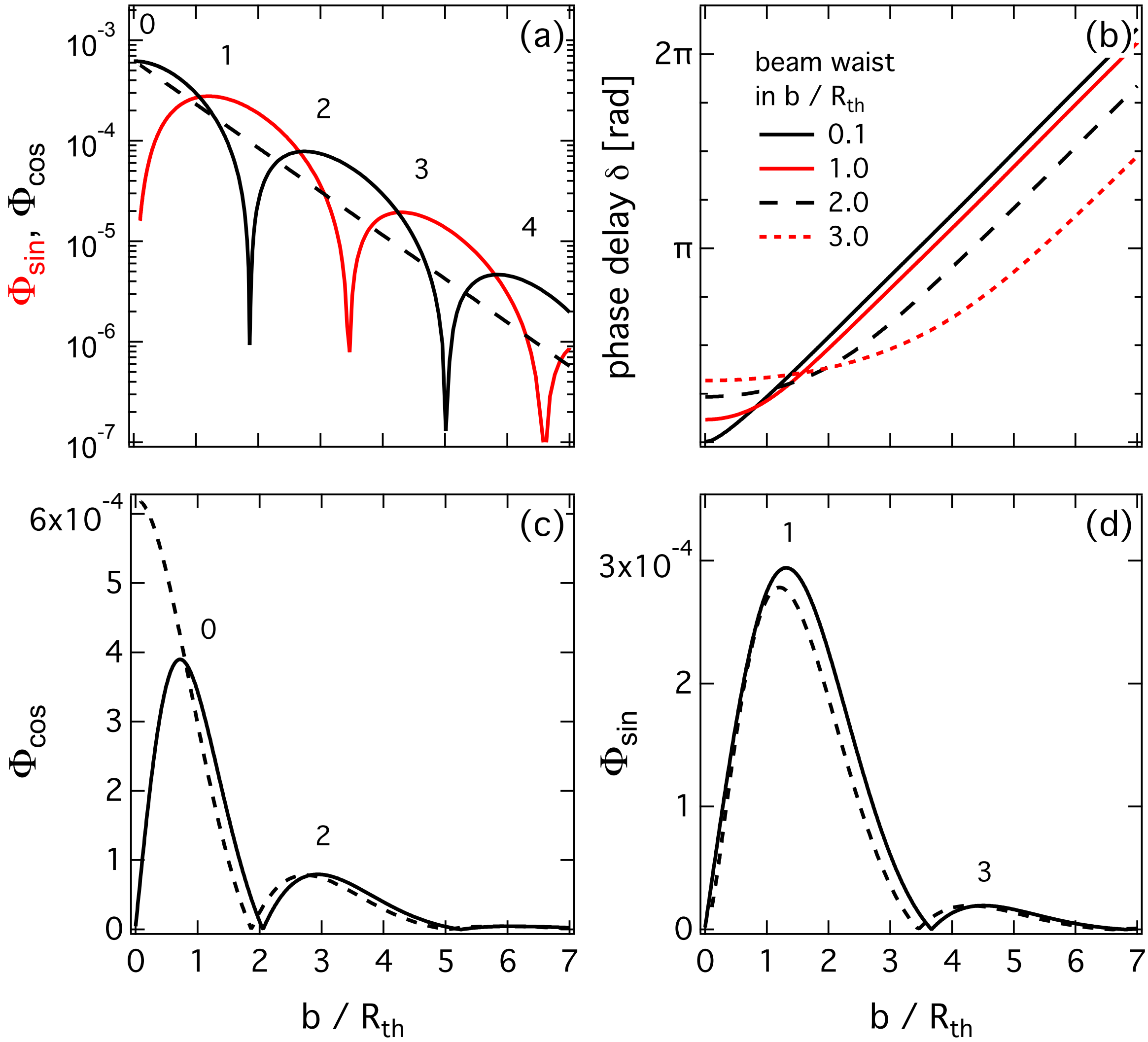

Figure 4.5: (a) The calculated photothermal deflection signal in-phase Φ_{cos} (black) and the of-out-phase with the harmonically modulated optical heating Φ_{sin} (red) in semilogarithmic scale showing the resonances 0 to 4 (res). (b) The phase delay of the deflection signal induced by the thermal transport for beam waists of 0.1 (black), 1.0 (red), 2.0 (dashed) and $3.0 b/R_{\mathrm{th}}$ (dotted) according to eq. 4.10. (c) In-phase Φ_{cos} and (d) out-of-phase signal Φ_{sin} for a Gaussian beam with the beam waist $\omega_0 = b/R$ (solid) and for rays of light (dashed).

as a lens of focal length $F(b;t)$. The demodulated photothermal signal at a frequency f as measured by a lock-in amplifier is proportional to the inverse focal length averaged over one period:

$$\begin{pmatrix} \Phi_{\sin}(b) \\ \Phi_{\cos}(b) \end{pmatrix} \propto 2f \int_0^{1/f} \begin{pmatrix} \sin(2\pi f t) \\ \cos(2\pi f t) \end{pmatrix} \frac{1}{F(b;t)} \mathrm{d}t. \tag{4.10}$$

The equation governing the ray propagation through the refractive index field at any given instant is Fermat's principle.[159] The model is sketched in the supplementary material of ref. [142]. Here, we exploit it for off-axis probing and photothermal deflection instead of lensing. The in-phase $\Phi_{\cos}$ and out-of-phase signals $\Phi_{\sin}$ with respect to the optical heating are plotted in fig. 4.5 (a). The signals depend on the fraction b/R_{th}. Phase delay δ and amplitude Φ are calculated via

$$\delta = \arctan\left(\frac{\Phi_{\sin}}{\Phi_{\cos}}\right) \text{ and } \Phi = \sqrt{\Phi_{\sin}^2 + \Phi_{\cos}^2}. \tag{4.11}$$

Using eq. 4.10 we find resonances at laser offsets b_i corresponding to multiples of the thermal diffusion length R_{th}, i.e. at $b_i = c_i R_{\text{th}}$ (see fig. 4.5 (a)). Specifically, the first five resonances are expected at $b_0 = 0$ (the nondeflection PT lensing signal, $\Phi_{\cos}$), $b_1 = 1.2 R_{\text{th}}$ ($\Phi_{\sin}$), $b_2 = 2.75 R_{\text{th}}$ ($\Phi_{\cos}$), $b_3 = 4.3 R_{\text{th}}$, $b_4 = 5.8 R_{\text{th}}$. With increasing order, the amplitudes of these resonances decay exponentially and become harder to detect experimentally. For impact parameters much larger than the decay length, $b/R_{\text{th}} \gg 1$, the time-dependent part of the thermal lens is completely damped and a stationary temperature profile remains. In this case, the TL is equivalent to the ideal one $n(r) = n_0 + \Delta n R/r$. Indeed, the focal length closely follows the photothermal Rutherford scattering result

$$F\xi = -1/2\left[1 + b^2\xi^2\right] \tag{4.12}$$

in this regime, where $\xi = -n_0/R\Delta n$.[29,30]

The deflections induced by the weak TL ($b\xi \gg 1$) differ from the ideal TL (see eq. 4.12) only substantially if the impact parameter and thermal diffusion length are roughly of the same size. Here, the out-of-phase component of the inverse focal length becomes significant, leading to a large contribution to the photothermal signal. The spatial oscillations for impact parameters larger than the thermal diffusion length $b > R_{\text{th}}$ coincide with the extrema of the refractive index field $\sin(r/R_{\text{th}})$. The in-phase deflection signal exhibits local extrema for impact parameters $b/R_{\text{th}} = m\pi$ (m being an integer), corresponding to $\cos(r/R_{\text{th}})$.

Equations 4.10 yields the photothermal deflection for one specific impact parameter b. The spatial extent of the laser focus is about ten times larger than the size of the heat source. Therefore, the deflections are averaged over different impact parameters. We handle this approximately by calculating the convolution of the detection beam's intensity profile with the in- and out-of-phase signals. Then the phase delay is calculated from the phase sensitive signals. Figures 4.5 (c) and (d) show the phase sensitive signals. It is found that the convolution shifts the positions of the extrema of $\Phi_{\cos}$ and $\Phi_{\sin}$ to higher impact parameters. The in-phase signal for $b = 0$ vanishes, as there is no deflection of the beam's center. An increase of the beam waist shifts the zeroth maximum to larger impact parameters (see fig. 4.5 (c)). Beam waist and impact parameter are approximately equal where the in-phase signal of the deflection is maximal.

The phase delay δ shows two features in fig. 4.5(b). At $b = 0$ of the detection beam, an increasing beam waist is increasing the phase delay from zero to larger values. A greater beam waist averages over regions with larger phase delays. The second feature is observed for impact parameters larger than the beam waist of the probe beam. Here, the increase of the phase delay is proportional to increase of the impact parameter as the heat needs more time to diffuse away from the heat source according to eq. 4.8. In between a nonlinear transition region is observed. The linear increase of the phase delay at larger offsets appears to be a good candidate to extract thermal transport coefficients from experimental data. For the analysis of the experimental data, the phase delay is chosen as it is independent of the temperature increase at the heat source if the lens is weak $\xi \gg 1$ and the medium linear.[29] It is a more reliable measure than the signal amplitudes.

4.2.2 Experiment

The experiment utilizes a custom-made microscopy setup (see fig. 4.6). A solid state laser (Coherent Verdi) provides the optical heating at 532 nm wavelength. The laser beam is intensity modulated using an acousto-optic modulator (Isomet 1260C) at frequencies between 50 and 1000 kHz. The laser beam is expanded and spatially filtered in a telescopic system with a pinhole. The detection laser beam is a laser diode (Coherent ULN) at 635 nm and a laser power of 1.2 mW. The detection laser beam is also expanded and spatially filtered. Its position in the sample plane is steered using a scanning galvanometer mirror (Thorlabs GVS21) and a telescopic system. The latter allows the rotation of the laser beam around the back focal plane of the illumination objective. Positions and focal length of the lenses were chosen as outlined by Fällman and Axner.[134] A dichroic mirror overlays both laser beams. A half-wave plate and a polarizer control the polarization of the probe beam. An oil-immersed objective (Olympus UPlanSApo 100x, NA=1.4) focuses both laser beams into the sample. The heating laser beam overfills and the detection beam underfills the back aperture of the illumination objective. A second objective (Olympus UPlanFLM 100x, NA=1.3) collects the transmission. The detection laser underfills the back aperture of the illumination objective to suppress photothermal lensing[27] and prevent clipping of the detection laser beam.

The transmission of the probe laser is separated from the heating laser by a dichroic mirror and an interference filter. The transmission is split into two parts using a knife-edge right-angle prism (Thorlabs MRAK25-P01) and imaged onto two different photodiodes (Thorlabs PDA36A) at 0 db amplification (see fig. 4.6). This detector configuration detects the deflection of the probe laser beam in one direction. Both detector signals are input to a lock-in amplifier (Signal Recovery DSP 7280) which calculates the difference between both photodiode signals and determines the phase sensitive deflection signal at the modulation frequency f. The setup detects the oscillations of the detection beam's center in one direction at f.

Samples consist of gold nanoparticles (Nanopartz, $R = 30\,\mathrm{nm}$), which are embedded between two 15 µm thick PDMS layers (polydimethylsiloxane; SYLGARD 184 from Dow Corning) on top of a glass substrate. A single gold nanoparticle is positioned in the focus of the heating laser by minimizing the transmission signal of the heating laser. The maximal temperature increase at the particle's surface is approximately 35 K for a heating intensity of $20\,\mathrm{kW/cm^2}$. The detection laser is scanned over a $(6 \times 6)\,\mathrm{\mu m^2}$ area at a resolution of $256\,\mathrm{px} \times 256\,\mathrm{px}$ and a pixel dwell time of 3 ms. The displacement between the laser foci along the optical axis is zero. In the experiment, we measure the phase sensitive signals $\Phi_{\cos}$ and $\Phi_{\sin}$. The liquid crystal samples consist of two glass substrates that

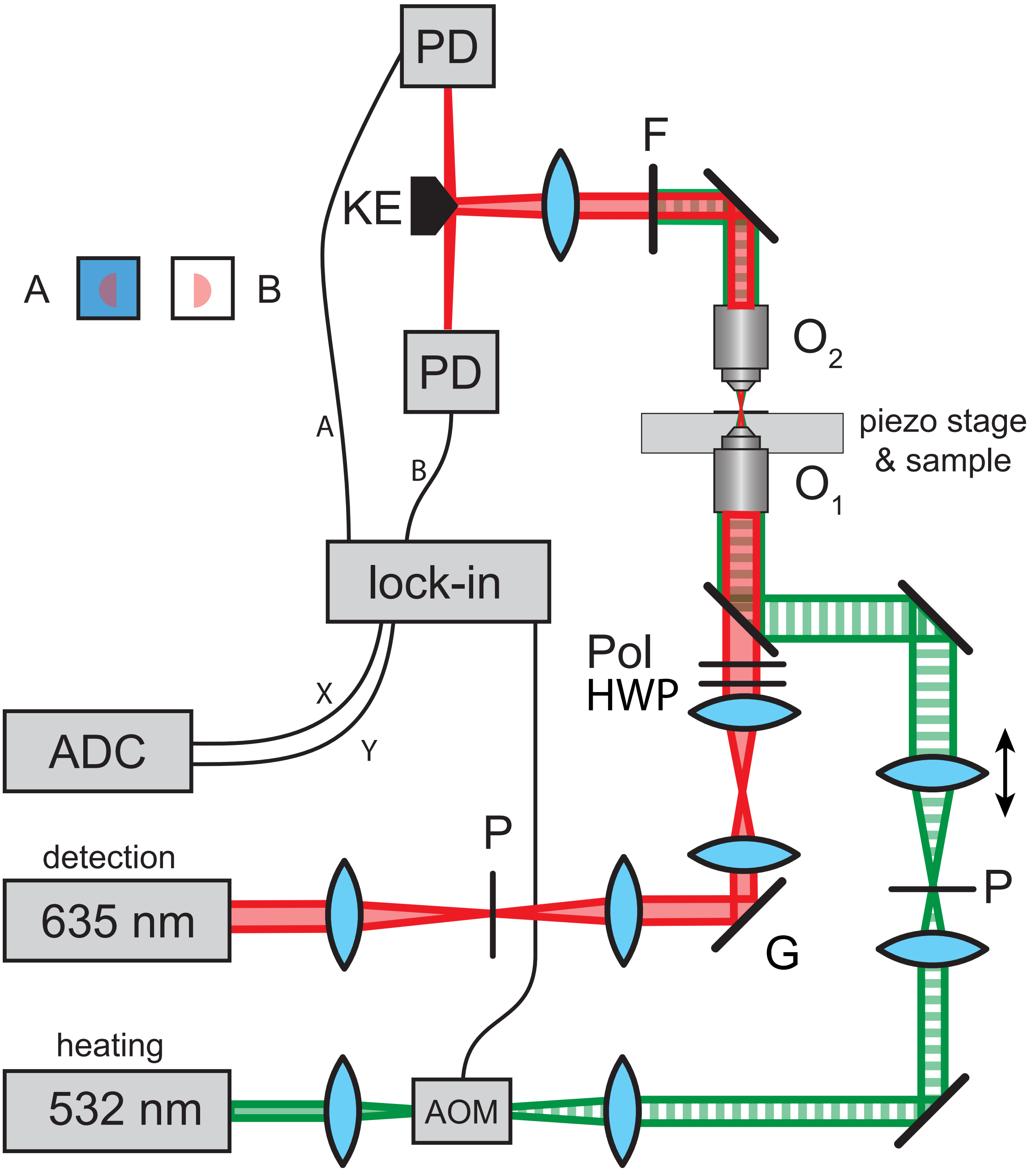

Figure 4.6: The experimental setup: Acousto-optic modulator (AOM), galvanometer scanning mirror (G), pinhole (P), half-wave plate (HWP), polarizer (Pol), illumination objective (O_1), detection objective (O_2), photodiodes (PD), reflective knife-edge prism (KE), analog digital converter (ADC).

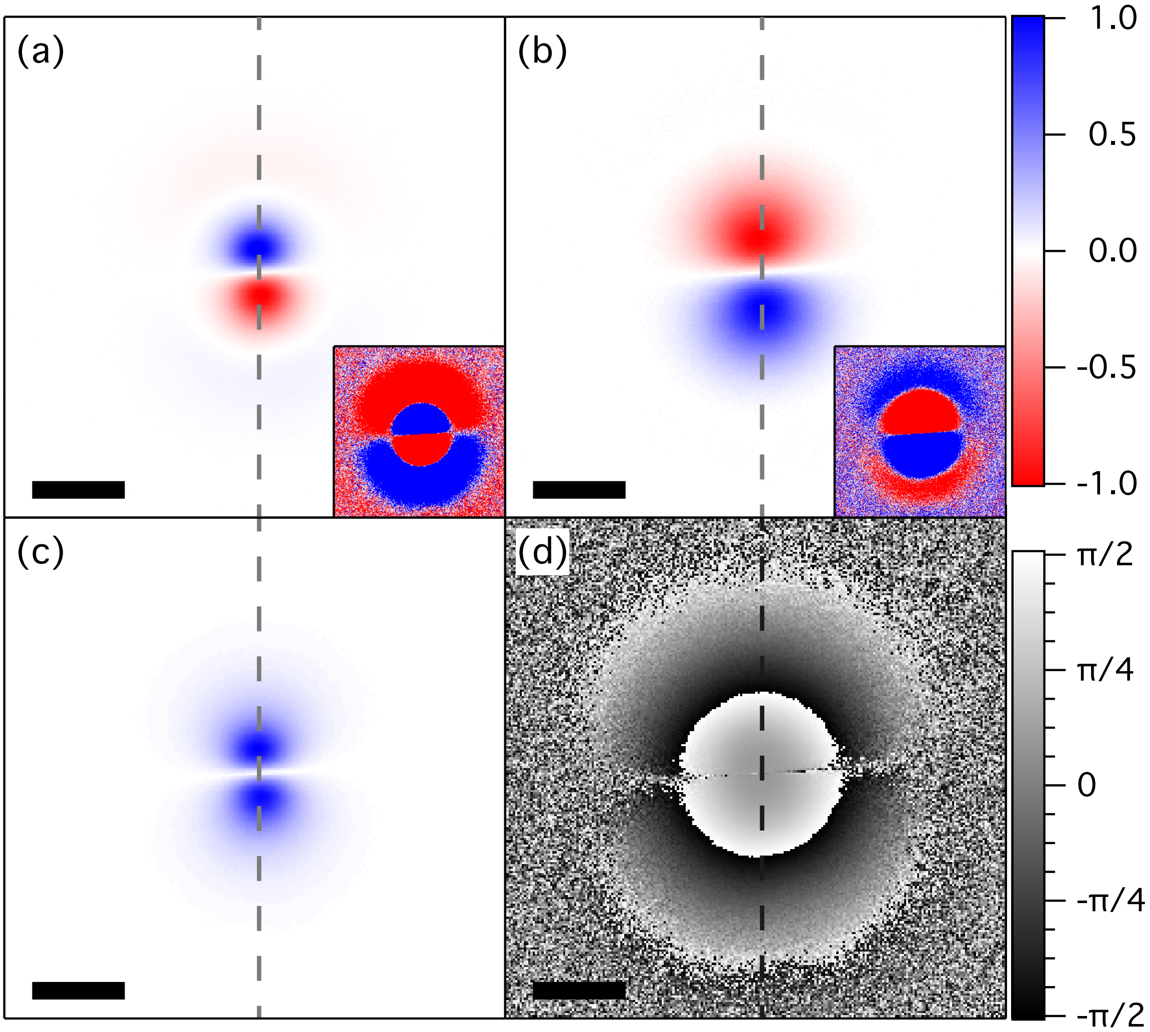

Figure 4.7: Photothermal deflection signal (a) in-phase and (b) out-of-phase with modulated optical heating in PDMS. The insets show the signal's sign. Amplitude (c) and phase delay (d) images are shown for a single gold nanoparticle with $R = 30\,\text{nm}$ in PDMS at a heating intensity of $30\,\text{kW/cm}^2$ and a modulation frequency of 200 kHz. See fig. 4.8 for the corresponding line profiles. The bars correspond to 1 µm.

restrict and align the liquid crystal 4-Cyano-4'-pentylbiphenyl (5CB). One substrate is coated with polyvinyl alcohol (PVA) and is unidirectionally rubbed to surface align the liquid crystal molecules. The other substrate is covered with a PVA layer that hosts single gold nanoparticles with 30 nm in radius. The liquid crystal layer has a thickness of approximately 5 µm.

4.2.3 Results and Discussion

Figure 4.7 shows a sample scan for a single particle at a modulation frequency of 200 kHz and fig. 4.8 the corresponding line profiles at 50 and 200 kHz and a peak heating intensity of $30\,\text{kW/cm}^2$. As compared to conventional photothermal microscopy where heating and probe laser overlap, our scanning system with a fixed heating beam probes the extended thermal lens. Thus, the spatial extent of the signal is much wider than the diffraction-limited signals typically observed for photothermal lensing[26] and deflection.[30]

The direction of the deflection measurement coincides with the vertical direction of the images. The phase sensitive images show two distinct extrema with opposite signs that are separated by a zero crossing at the position of the gold nanoparticle $b = 0$ (see fig. 4.7 (a) and (b)). The direction of the deflection changes when the sign of the impact parameter b does. The resonances 0 and 1 from fig. 4.5 are clearly visible in fig. 4.7 (a) and fig. 4.7 (b), respectively. Besides these global extrema closest to the position of the gold nanoparticle, resonance 2 is visible in the in-phase signal in fig. 4.7 (a) as well as resonance 3 in the out-of-phase signal $\Phi_{\sin}$ in fig. 4.7 (b). The amplitude of the photothermal deflection signal $\sqrt{\Phi_{\cos}^2 + \Phi_{\sin}^2}$ does not exhibit any resonances due to the strong damping of the thermal waves (see fig. 4.7 (c)).

The phase delay δ, which is induced by the thermal transport, is plotted with a periodicity of π in fig. 4.7 (d). The phase delay increases with the distance from the position of the nanoparticle. The phase delay is almost spherically symmetric with respect to the position of the nanoparticle. A deviation from the spherical symmetry is visible only for small vertical distances from the nanoparticle as there is no deflection. In this region, the phase is undefined as the deflection amplitude is vanishing.

The line profiles in fig. 4.8 (a-d) at modulation frequencies of 50 and 200 kHz allow for a more quantitative comparison. $\Phi_{\cos}$, $\Phi_{\sin}$ and Φ decrease with the modulation frequency, and they are confined to a region closer to the location of the nanoparticle (see fig. 4.8 (a-c)). The position of the resonance closest to $b = 0$ in fig. 4.8 (a) and (c) is independent of the modulation frequency and therefore a property of the laser focus. Resonance 2 is clearly visible for the in-phase signal. The position of the maximum depends on the modulation frequency and therefore contains information on the thermal diffusivity. However, the phase delay is better suited to extract thermal diffusivities, as this value depends only on the beam waist of the detection focus and the thermal diffusion length. The phase delay is minimal for small impact parameters $b \approx 0$ and shows a plateau (see fig. 4.8 (d)). The plateau results as explained in the theory section from an averaging of the detection laser over phase delays from a finite volume. The relative size of the volume increases with the modulation frequency. Therefore, the phase delay at $b = 0$ increases with the modulation frequency, which is also observed in fig. 4.5 (d). The phase delay is well fitted with the geometric optics model, where the phase delay is weighted according to the signal amplitude. From the fits, the thermal diffusion length and the effective beam waist are extracted.

To validate the applicability of photothermal microscopy, we measure the thermal diffusivity of PDMS. Single gold nanoparticles are optically heated using a peak heating intensity of $4\,\mathrm{kW/cm^2}$ and modulation frequencies of 50, 100, 200, 400 and 1000 kHz. Sample data points and fits are shown in fig. 6.3 in appendix 4.2. Figure 4.8 (e) plots the thermal diffusivities against the modulation frequency for eight different particles. At the highest modulation frequency of 1000 kHz the average extracted thermal diffusivity is 5% larger than the average at all other modulation frequencies, and the standard deviation is bigger. This observation originates from the geometric optics model, which performs best for impact parameters larger than the beam waist. At high modulation frequencies the data points for large impact parameters b/R_{th} are sparse due to the rising attenuation of thermal waves with the modulation frequency (see also fig. 6.3 in appendix 4.2). For high modulation frequencies, it becomes evident that only the plateau contributes and the straight tail is not fitted. The average thermal diffusivity of $(1.32 \pm 0.04) \cdot 10^{-7}\,\mathrm{m^2\,s^{-1}}$ using modulation frequencies from 50 to 400 kHz is in

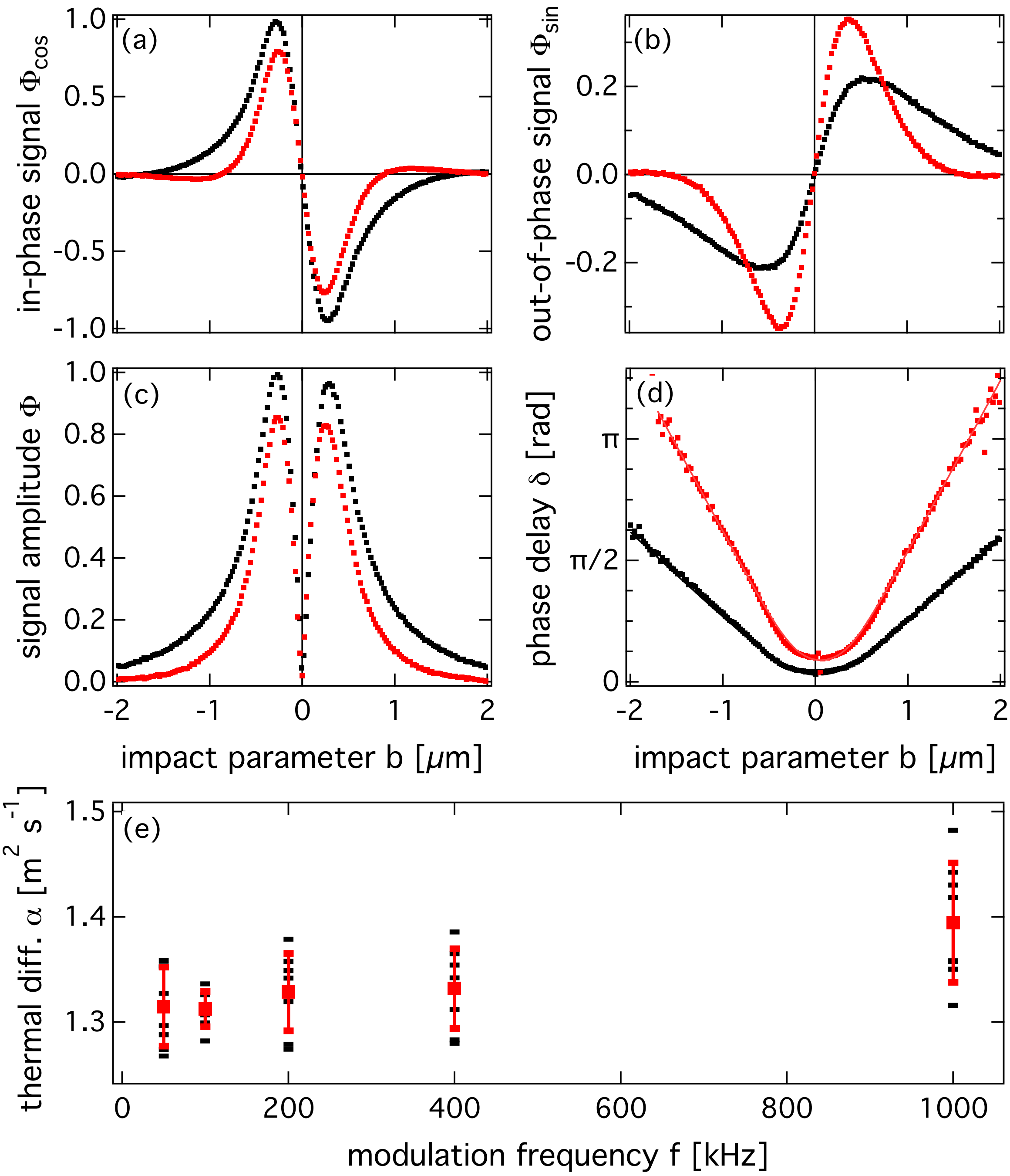

Figure 4.8: Line profiles (a) in-phase $\Phi_{\cos}$, (b) out-of-phase signal $\Phi_{\sin}$, (c) amplitude Φ and (d) phase delay δ of the photothermal deflection along the to dashed lines in fig. 4.7 in PDMS. The modulation frequencies are 50 kHz (black) and 200 kHz (red). (e) Thermal diffusivities extracted from the line profiles of the phase delay using the ray optics model. The black points are the data points for individual nanoparticles. The red squares show the average thermal diffusivity for each modulation frequency. The average thermal diffusivity using modulation frequencies from 50 to 400 kHz is $(1.32 \pm 0.04) \cdot 10^{-7}\,\mathrm{m^2\,s^{-1}}$.

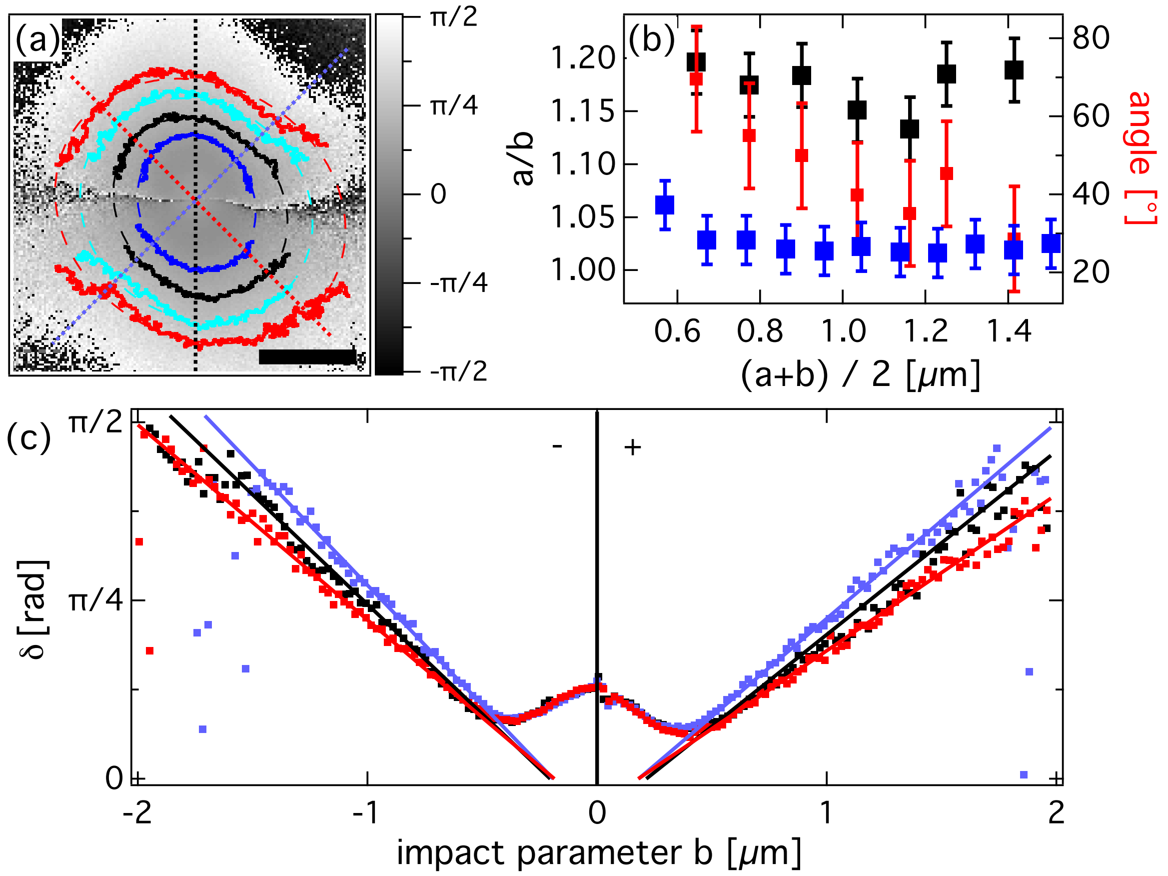

Figure 4.9: (a) Phase delay δ for the liquid crystal 5CB image with overlaid contour lines where the phase delay is 0.4 (blue), 0.6 (black), 0.8 (light blue) and 1.0 rad (red). The dashed lines are least square ellipse fits to determine orientation and fraction of the semi axes. The scale bar corresponds to 1 μm. The dotted lines show the direction of the deflection (black), ordinary (blue) and extraordinary axis (red). (b) shows the parameters extracted from the ellipse fitting. It plots the fraction of semi-major axis and semi-minor axis against the average radius for PDMS (blue, $a/b = 1.02 \pm 0.02$) and 5CB (black, $a/b = 1.18 \pm 0.03$). The red data points show the orientation of the semi-major axis for 5CB. (c) show line profiles (dots) extracted from (a) and corresponding linear fit to the tails. The line profiles are extracted along the dotted lines in figure (a) with the corresponding colors.

very good agreement with the one measured on a macroscopic sample with a laser flash measurement $(1.30 \pm 0.02) \cdot 10^{-7}\,\mathrm{m^2 s^{-1}}$ (Linseis LFA 1000).[160]

So far, photothermal microscopy has been used in isotropic and linear media to study thermal transport. We quantify the anisotropy of the thermal transport in the liquid crystal 5CB. The principal axes' orientation of the liquid crystal is determined using quantitative polarization contrast microscopy.[135] Then the detection laser is polarized parallel to the extraordinary axis of the liquid crystal domain, and the deflection is measured at an angle of approximately 45° to the principal axes. The phase delay image and the corresponding line profiles along the principal axes and the deflection direction are shown in fig. 4.9 (a) and (c).

The most striking feature of the line profiles is the initial decrease of the phase delay as the distance to the nanoparticle increases. As the refractive index of the liquid crystal is large, the absorption resonance of the gold nanoparticle is red-shifted. The absorption of the detection laser by the gold nanoparticles adds a stationary optical heating, which eventually leads to the nematic–isotropic phase transition at $T_c = 35\,^\circ\mathrm{C}$ and thus influences the photothermal deflection signal. If the distance between the center of the detection laser and the position of the nanoparticle increases, the optical heating by the detection laser decreases. Therefore, the phase transition in a smaller volume is modulated and leads to a smaller phase delay. This dependence could be utilized to study the phase transition in liquid crystals but requires a more refined model that includes the stationary heating by the probe laser beam and nonlinearities of the thermal transport coefficients. For impact parameters larger than the beam waist of the detection laser the phase delay is proportional to the impact parameter and reflects the phase delay in the nematic phase of the liquid crystal.

To extract the anisotropy of the thermal transport, we fit a linear function to the tails of the phase delay measured along directions of the principal axes of the refractive index of the liquid crystal. The thermal diffusion length is determined with $R_{\mathrm{th}}^{-} = 0.95\,\mu\mathrm{m}$ for negative impact parameters and $R_{\mathrm{th}}^{+} = 1.10\,\mu\mathrm{m}$ for positive ones. For the extraordinary axis the thermal diffusion length are $R_{\mathrm{th}}^{-} = 1.15\,\mu\mathrm{m}$ and $R_{\mathrm{th}}^{+} = 1.45\,\mu\mathrm{m}$, respectively. The different results of the positive and negative deflection direction result from a drift of the nanoparticle out of the heating focus, thereby reducing the heating power at the gold nanoparticle. The phase transition is then modulated in a smaller volume, increasing the thermal diffusion length. The above-reported values of the thermal diffusion length reveal an anisotropy of about $(18 \pm 2)\%$.

Alternatively, we analyze the contour lines for different phase delays, which enable the determination of the orientation of the principal axes. The reference measurement in PDMS shows as expected an isotropic thermal transport (see fig. 4.7 (d) and 4.9 (b)). From the phase delay image the contour line is extracted (see fig. 4.9 (a)). To extract the orientation, the length of semimajor a and the semiminor axes b, an ellipse is fitted to the data points using a least-squares algorithm.[161] The ratio a/b and the orientation of the semimajor axes are shown in fig. 4.9 (b). The anisotropy of the thermal transport gives again $(18 \pm 2)\%$ and the orientation angle of $47^\circ \pm 14^\circ$ with the vertical axis agrees well with the angle of 50° obtained from the polarization contrast measurement. A simulation of the heat transport using COMSOL gives an anisotropy of the thermal diffusion lengths of 35%. The lower ratio detected by our experiments is, however, expected as the nanoparticle is located at the interface between liquid crystal molecules and glass. This deviation gives further evidence that local heterogeneities in the thermal conductivity may be accessed by the presented method. It will be thus highly interesting to apply this method to biological materials or even living cells.

4.2.4 Conclusion

We have shown that thermal waves generated by optically heated gold nanoparticles lead to the observation of resonances in the phase sensitive photothermal deflection signal generated by the local refractive index change around the heated nanoparticle. This behavior is at first glance counterintuitive, as the temperature wave-field is overdamped. However, the resonances result from a projection of the deflection amplitude onto the cos- and sin-functions.

As compared to the recently proposed frequency-dependent photothermal lensing measurements in solids and liquids[160] no modeling of aberrated laser beams is required. Here we employ a geometric optics model to extract thermal diffusivities from photothermal deflection measurements. The photothermal deflection has several advantages as compared to photothermal lensing. Photothermal deflection does not need to deal with the competition between photothermal lensing and scattering which occurs for photothermal lensing and complicates the analysis of the photothermal lensing approach. The two-dimensional information on photothermal deflection makes heterogeneities and anisotropies of the thermal transport in the vicinity of the heated nanoparticle directly accessible. For large impact parameters, the detection laser is not illuminating the nanoparticle. Therefore, the nano-object is not heated by the detection laser. The exclusion of optical heating by the detection laser is of particular importance if phase transitions are to be studied by photothermal microscopy. The simple modeling makes photothermal deflection microscopy more appealing for the study of thermal transport measurements of thermal transport in complex media.

We have used photothermal deflection microscopy to study thermal transport in a linear, isotropic and a nonlinear, anisotropic medium surrounding a single nanoparticle by modeling the data with a simple geometric optics model. The presented measurement scheme was used to detect anisotropies in the thermal transport by determining the deflection in different directions in the liquid crystal 5CB. Other currently existing techniques such as time-domain thermoreflectance[6] are not applicable to the study of thermal transport in polymers under mechanical load[23] as the stretching of the polymer film deforms the reflecting metal layer irreversibly, making the thermal transport measurement impossible. As a first example, many phenomena observed in photothermal microscopy of liquid crystals may be studied in greater detail.[125–128]

Acknowledgement Financial support by the graduate school BuildMoNa as well as funding by the European Union and the Free State of Saxony are acknowledged.

4.3 Metal Nanoparticle Based All-Optical Photothermal Light Modulator

Abstract

We present a simple scheme for the manipulation of light intensity by light mediated by a dissipative process. The implementation employs the heat released by an optically excited plasmonic metal nanoparticle to control the size of an isotropic bubble in a nematic liquid crystal film. The nematic film is designed as a zero-order half-wave plate that rotates an incident probe light polarization by $\pi/2$ and is blocked by an analyzing polarizer behind the structure. The growing isotropic bubble disturbs the half-wave plate and causes the probe to be transmitted through the modulator structure. Our results demonstrate that dissipative processes may be advantageously used to control light by light.

Adapted with permission from **A. Heber**, M. Selmke, F. Cichos: *Metal Nanoparticle Based All-Optical Photothermal Light Modulator*, ACS Nano **8**:2, 1893-1898 (2014). Copyright (2014) American Chemical Society. Details on the author contributions are given in the appendix 6.4.

Controlling light propagation with light is intrinsically difficult as the photon–photon interaction cross-sections are almost vanishing.[162] Thus dielectric media have to pick up the role of photonic modulators, and a number of different and highly advanced schemes have been proposed to control the flow of light by light with the help of nonlinear optical effects,[163,164] optical resonators,[165] exciton polaritons,[166,167] or with the optical response of a two-level system in a single fluorescent molecule.[168] Approaches utilizing photoexcited carriers in biased p-i-n diodes provide high speed switching at GHz frequencies.[169] Twisted liquid crystal cells allow for polarization control in light propagation.[170] Many of these schemes utilize highly advanced structures and technologies for realizing these photonic modulators. Here, we report on an extremely simple all-optical modulator based on a single metal nanoparticle embedded in a liquid crystal. The transmission of a focused laser beam is controlled by the local phase composition in a liquid crystalline cell. This phase composition is varied by an optical signal heating a gold nanoparticle. The presented modulator can be easily prepared by simple self-organization methods and provides an example of a slow-speed dissipative switch to control the propagation of light by light.

Our all-optical intensity modulator is constructed as a zero order half-wave plate (see fig. 4.10 and Materials and Methods section). Therefore, we utilize a homogeneously aligned liquid crystal layer with accurately tuned thickness into which single gold nanoparticles are embedded.

The birefringence of the liquid crystal causes a phase retardation β (eq. 4.13) between the electric field components parallel and perpendicular to the director according to the ordinary $n_{\perp}$ and extraordinary refractive index $n_{||}$,[101] the thickness d of the liquid crystal film and the vacuum wavelength λ_{d} of the incident probe laser beam:

$$\beta = \frac{2\pi(n_{||} - n_{\perp})d}{\lambda_{\mathrm{d}}}. \tag{4.13}$$

This retardation β increases with the thickness d at a given refractive index contrast $\Delta n = n_{\perp} - n_{||}$ which is specified by the choice of the liquid crystal. At a retardation of $\beta = \pi$ the liquid crystalline layer acts as a half-wave plate. This is fulfilled for $d = d_{\mathrm{min}} = 3.2\,\mu\mathrm{m}$ thick 5CB layer at $T = 307\,\mathrm{K}$.[101] At this thickness, the liquid crystal acts as a zero order half-wave plate rotating an incident polarization of $\zeta = \pi/4$ by $\pi/2$ where ζ is the polarization angle with respect to the liquid crystal director.

As the transmitted light impinges on the analyzer oriented parallel to the incident polarization, no light is transmitted through the modulator structure. The transmission through the whole structure including the two polarizers then follows as[135]

$$\mathfrak{T} = \frac{I(\beta,\zeta)}{I_0} = 1 - \sin^2(2\zeta)\sin^2(\beta/2). \tag{4.14}$$

An intensity modulator based on a nematic liquid crystal film thus has to control the thickness of the nematic phase optically. This can be achieved by a gold nanoparticle placed on the PVA/5CB interface. While the gold nanoparticle itself may induce a local distortion of the director structure[171] it only negligibly perturbs the local transmission through the cell. If the gold nanoparticle is placed in the focus of a laser beam resonant to the wavelength of the plasmon resonance ($\lambda_{\mathrm{h}} = 532\,\mathrm{nm}$), the heat released by the particle[172] will cause a local phase transition from the nematic to the isotropic phase. The hot nanoparticle generates an isotropic bubble, which decreases the thickness of the nematic

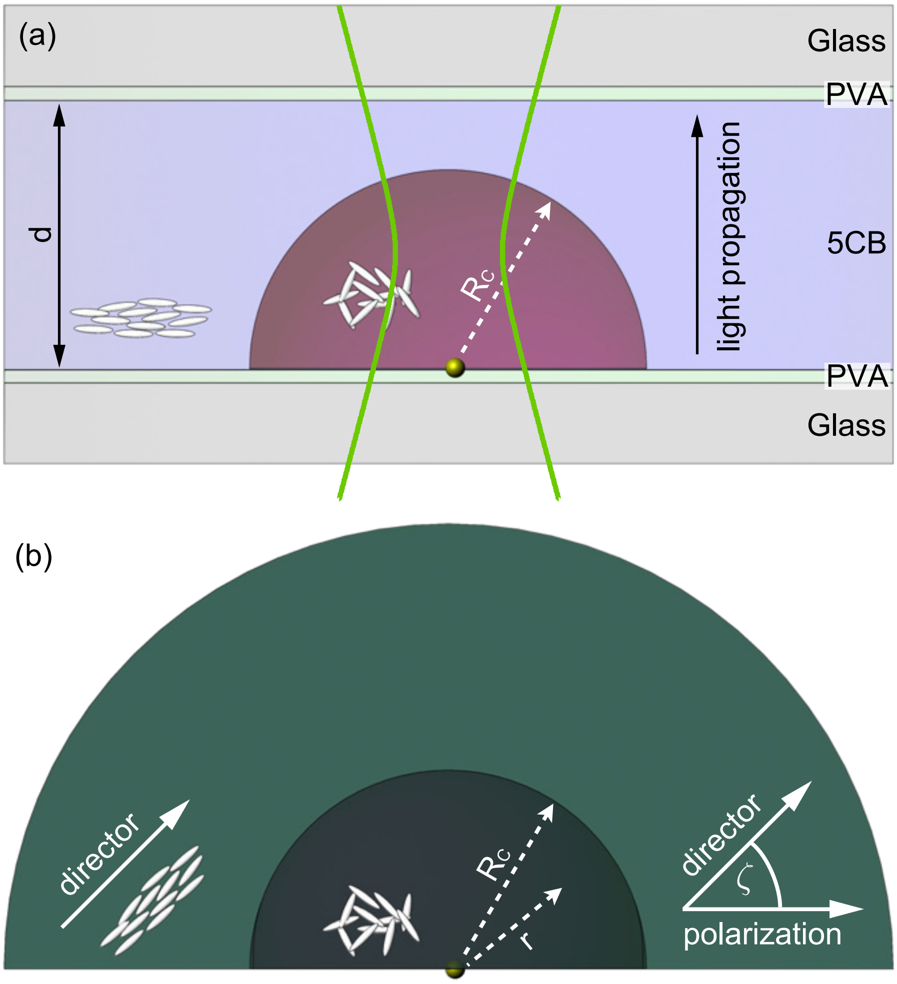

Figure 4.10: Scheme of the photothermal light modulator. (a) Side view: The modulator structure consists of a liquid crystal and a gold nanoparticle heated optically to convert the liquid crystal from the nematic to the isotropic phase. (b) Top view: The principle axis of the liquid crystal in the nematic phase is oriented at 45° to the polarization of the detection laser. The liquid crystal film of a well-defined thickness d_{min} forms a zero-order half-wave plate.

layer locally and thus causes a smaller retardation of the field components of a weakly absorbed laser wavelength λ_{d} (see fig. 4.10 for a sketch). If this isotropic bubble extends across the whole film thickness, all light is transmitted. Consequently, the optically controlled heat dissipation of the nanoparticle at its plasmon resonance controls the light transmitted through the modulator structure between 0 and 100 %. As the liquid crystal is well- ordered on length scales of the probe beam waist, the total optical contrast is mainly related to the quality of the polarizers in the modulator structure.

4.3.1 Results and Discussion

Stationary Response of the Modulator Structure In the steady state, the phase boundary between the nematic and the isotropic liquid crystalline phase occurs at a distance R_{C}, where the phase transition temperature matches the local temperature $T(R_{\text{C}}) = T_{\text{C}}$. Since the liquid crystal structure is anisotropic, the heat conductivity is anisotropic as well, and the phase boundary is nonspherical.[102] Further, the interface to the PVA film and the glass cover slide will distort the temperature profile.[173] For simplicity we model the temperature profile to be isotropic such that

$$\Delta T(r) = T(r) - T_0 = \frac{P_{\text{abs}}}{4\pi\kappa r} = \frac{1}{4\pi\kappa r}\frac{2\sigma_{\text{abs}} P_{\text{inc}}}{\pi\omega_{\text{h}}^2} \tag{4.15}$$

with P_{abs} being the absorbed laser power at $\lambda_{\text{h}} = 532\,\text{nm}$, T_0 the ambient temperature, κ the average thermal conductivity of the liquid crystal, P_{inc} the heating power incident on the back aperture of the microscope objective, $\sigma_{\text{abs}} = 9.6 \cdot 10^{-15}\,\text{m}^2$ the gold nanoparticle absorption cross-section and $\omega_{\text{h}} = 270\,\text{nm}$ the beam waist of the heating laser. Taking all effects into account that lower the intensity incident on the particle $P_{\text{inc}} = 100\,\mu\text{W}$ corresponds to $P_{\text{abs}} = 2.6\,\mu\text{W}$ (see also appendix 6.3). The changing radius of the isotropic bubble requires a detailed analysis of the light scattering properties of the isotropic bubble, which is beyond the simple demonstration targeted here. We note that a detailed modeling of the light scattering at this liquid crystal structure will allow a detailed study of local phase transitions in liquid crystals as well, which is a new and promising field of research for itself.[26,27]

Here, we describe the change in the transmission by assuming that the thickness of the nematic phase is given by the overall film thickness d_{min} minus the radius R_{C} of the isotropic bubble created around the gold nanoparticle (see fig. 4.10). Under steady state conditions the radius of the isotropic bubble is given according to eq. 4.15 by $R_{\text{C}} = R\Delta T/[T_{\text{C}} - T_0]$, where R is the particle radius and $\Delta T = \Delta T(R)$ the temperature increase on the surface of the particle induced by the optical heating. Thus the phase retardation is

$$\beta = \frac{2\pi\Delta n}{\lambda_{\text{d}}}\left[d_{\text{min}} - R\frac{\Delta T}{T_{\text{C}} - T_0}\right] \tag{4.16}$$

and using equation 4.14 the transmission through the modulator structure for an incident polarization of $\zeta = \pi/4$ is found to be

$$\mathfrak{T}(\Delta T, T_0) = \cos^2\left(\frac{\pi\Delta n}{\lambda_{\text{d}}}\left[d_{\text{min}} - R\frac{\Delta T}{T_{\text{C}} - T_0}\right]\right). \tag{4.17}$$

According to equation 4.17, the transmission depends only on the particle radius R, the ambient temperature T_0 and the temperature increment ΔT at the particle surface. Figure 4.11 (inset) plots the expected transmission for various ambient temperatures as a function of the particle temperature rise. At $\Delta T = 0$ the modulator structure shows zero transmission, while the transmission becomes maximal at $\Delta T = [T_{\text{C}} - T_0]d_{\text{min}}/R$. Thus the temperature rise required to switch from zero to full transmission decreases the closer the ambient temperature T_0 is to the phase transition temperature. The corresponding absorbed heating power is

$$P_{\text{abs}}^{\text{min}} = 4\pi\kappa d_{\text{min}}(T_{\text{C}} - T_0). \tag{4.18}$$

Above this absorbed power, no further transmission changes occur. As the film thickness d_{min} is typically 100 times larger than the particle radius R and the ambient temperature is about 0.1 K below the phase transition temperature, it requires a temperature rise of just 10 K to switch from zero to 100 % transmission. The calculated transmission curves displayed in fig. 4.11 (inset) also reveal that

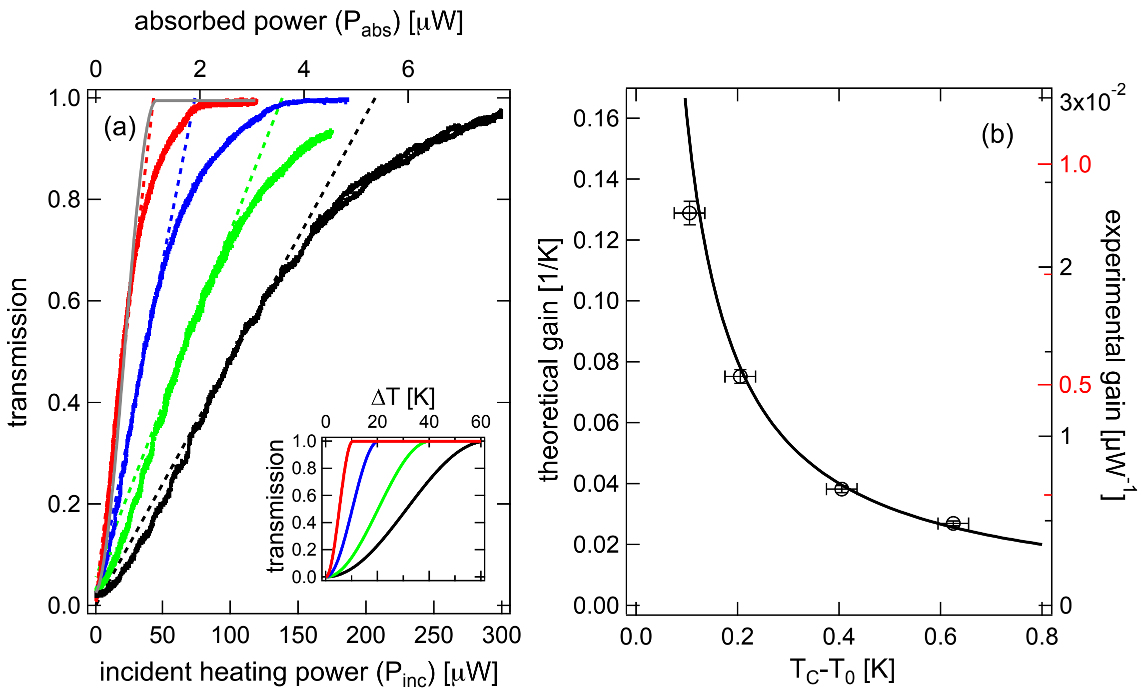

Figure 4.11: (a) Steady state response: The transmission of the probe laser beam is plotted against the incident heating power. It is varied sufficiently slowly to achieve a steady state transmission signal of the system at each incident heating power. The transmission is shown at different temperatures $T_C - T_0$ being 0.11 K (red), 0.21 K (blue), 0.43 K (green) and 0.63 K (black) below the nematic to isotropic phase transition temperature $T_C = 307.5$ K. The corresponding dashed lines are tangents of the maximum slopes indicating the linear regime and determining the experimental gain. The gray line is a fit of equation 4.17 to the experimental data. The inset shows the theoretically derived transmission as a function of the temperature increase at the nanoparticle's surface according to eq. 4.17. (b) Gain factors: Comparison of theoretical (line) and experimental gain factors (markers), which correspond to the maximum transmission increase per temperature and incident heating/absorbed power (see eq. 4.19). The labels on the right axis correspond to the experimental gain with respect to P_{inc} (black) and P_{abs} (red).

the slope of the transmission curve is controlled by the ambient temperature. Thus a small particle temperature variation $\delta\Delta T$ causes a strong transmission variation $\delta\mathfrak{T}$ if the ambient temperature is close to the phase transition temperature. The maximum slope of the transmission function $\mathfrak{T}$ eq. 4.17 therefore defines the gain $\mathfrak{G}$ eq. 4.19 of the system, i.e. the maximum transmission factor change per Kelvin particle temperature rise at an ambient Temperature T_0:

$$\mathfrak{G} = \left.\frac{\delta\mathfrak{T}}{\delta\Delta T}\right|_{\mathfrak{T}=1/2} = \frac{\pi\Delta n}{(T_C - T_0)}\,\frac{R}{\lambda}. \tag{4.19}$$

This gain factor diverges in case the ambient temperature corresponds to the phase transition temperature $T_0 = T_C$. It decays to zero if the ambient temperature is far below the phase transition temperature. The modulator structure has two control parameters defining the transmission. The first is the heating power, which controls the particle temperature rise and thus corresponds to the base voltage of an electrical transistor and second the ambient temperature, which controls the gain.

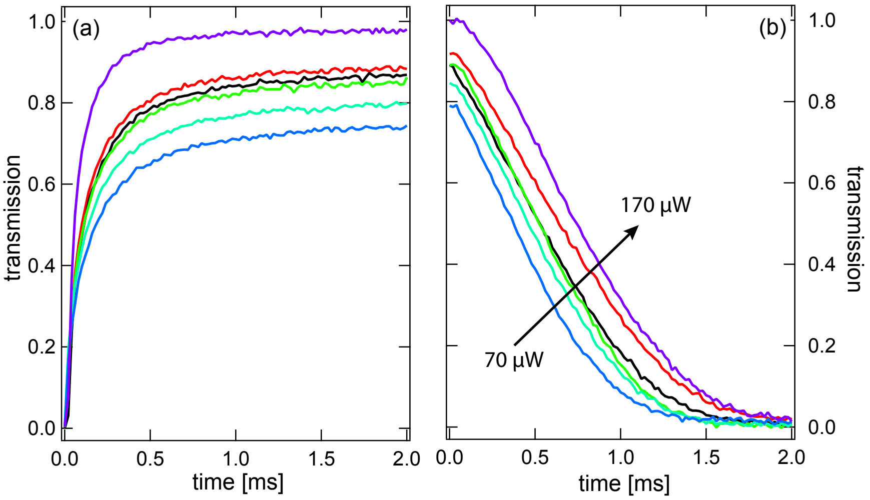

Figure 4.12: Step response of the optical modulator at $T_C - T_0 = 0.2\,\mathrm{K}$: The transmission of the modulator structure is displayed in response to a step-like switching of the heating laser. (a) The switch-on response is plotted for incident heating powers at 70 (blue), 85 (light blue), 95 (green), 103 (black), 123 (red) and 170 µW (violet). (b) Switch-off response of the modulator structure at the same incident heating powers as in (a).

Experimental transmission data obtained with a 5CB liquid crystal modulator described above is displayed in fig 4.11 (a). Details of the experimental setup can be found in the supplementary information and ref. 26. The graph shows the transmission at various incident heating powers and different ambient temperatures T_0. The ambient temperature is thereby controlled with a resistive heater attached to the objective. The experimental data clearly follow the predicted behavior. The closer the ambient temperature gets to the phase transition temperature, the steeper is the increase in transmission with the incident heating power. The experimental data can be fitted with eq. 4.17 displaying a good agreement. At low powers deviations occur, which are due to the fact, that the isotropic bubble is smaller than the beam waist of the probe beam. Between 80% and 100%, the saturation of the transmission signal with rising incident heating power is slower than in the experiment because of the spherical shape of the nematic to isotropic interface. The maximum slope of the curve is shown in fig. 4.11 (b), characterizing the amplification factor of the modulator structure. The experimental gain factor $\mathfrak{G}$ is given by the maximum slope of the transmission curve with increasing heating power. The incident heating power can be converted into a particle temperature rise using the absorbed fraction of the power (see sapendix 6.3). This absorbed fraction of the heating power is given by the fraction of the absorption cross-section σ_{abs} compared to the illuminated focus area with a radius of 270 nm (see eq. 4.15). Accordingly, a power of 10 µW incident heating power corresponds to a temperature increase of about 1 K. Experimental gain values are given in $\mu\mathrm{W}^{-1}$, since the temperature of the particle is not exactly known. The theoretical data is included using the left axis for a gold nanoparticle with $R = 30\,\mathrm{nm}$ in a 5CB environment. Both the experimental and theoretical gain factor agree well in their dependence on the ambient temperature T_0. Thus, when stabilizing the ambient temperature very close to the nematic–isotropic phase transition temperature strong changes of the transmitted optical power can be obtained for very small changes in the incident optical control beam. This is in contrast to most all-optical modulators demonstrated before, which control a weak signal with a very intense control beam. In the case of the presented photothermal modulator, this probe power is only limited by the absorption of the probe power by the gold nanoparticle.

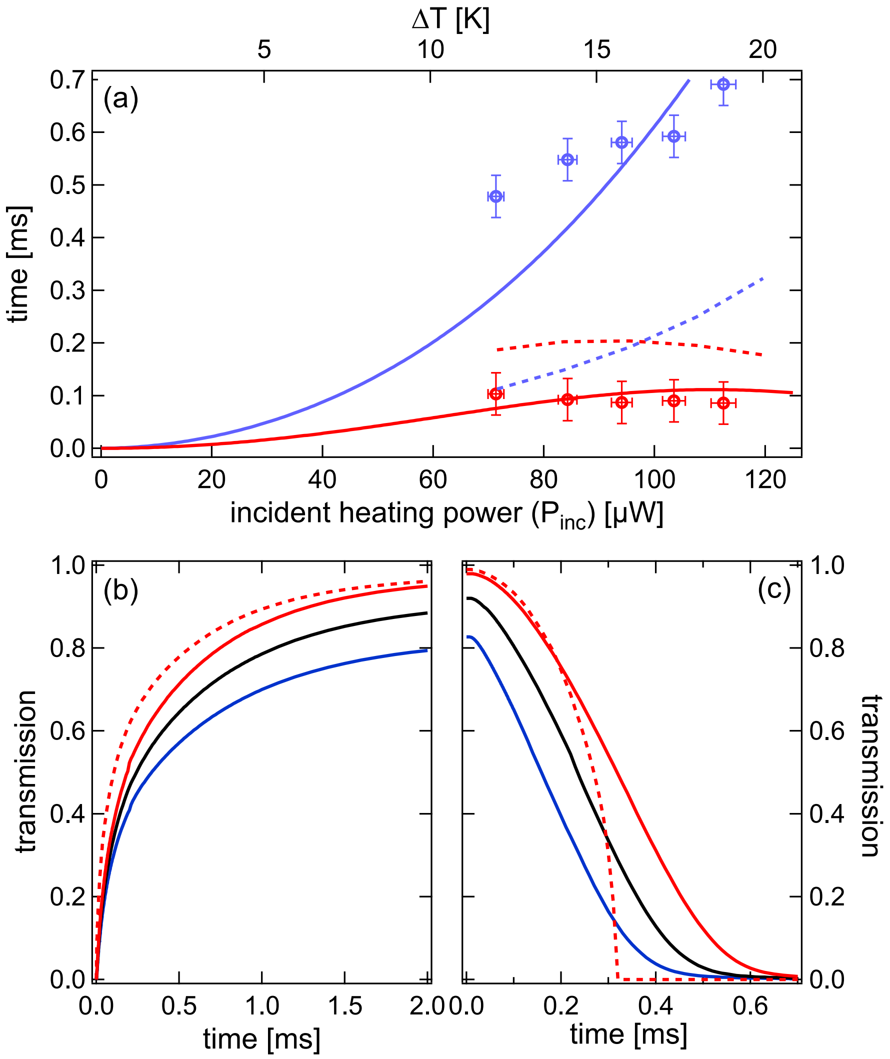

Figure 4.13: Comparison of experimental and theoretical switching times at $T_C - T_0 = 0.2\,\mathrm{K}$: (a) The times required to change the transmission signal of the modulator by 50% are plotted for the switch-on (red) and switch-off process (blue). The dashed lines show the results of the numerical simulations. The solid lines represent the trend from a simple analytical model (see appendix 6.3). The markers display the experimental results. (b) and (c) show the corresponding time-dependent transmission signals obtained from the simulations using eq. 4.20 to get steady state transmission at $\mathfrak{T} = 83\%$ (blue), $\mathfrak{T} = 92\%$ (black) and $\mathfrak{T} = 100\%$ (red). The solid lines include a heating effect due to the detection laser, whereas the red dashed line excludes that effect.

Dynamic Response of the Modulator Structure The second key factor characterizing the modulator is related to the dynamics of the switching process. Here, the switching from zero transmission to the steady state transmission and back is studied as a function of the incident heating power. Therefore, the probe laser beam is focused onto the particle, the heating laser beam is switched on/off, and the time-dependent probe response is recorded at a time resolution of 20 µs. At 0.2 K below the phase transition temperature, 50% of the transmission is reached after 0.1 ms. The experimental data are shown in fig. 4.13 for six different heating powers and reveal that most of the signal change is occurring within a few milliseconds.

To quantify the time scale, we plot the time when half the steady state signal is reached in either the switch-on or the switch-off process (see fig. 4.13 (a)). As found, the switch-on time is about 100 µs and almost constant for the considered heating power range. The switch-off time increases with increasing heating power. This can be qualitatively understood from the following arguments. We assume that the time required to reach half the steady state signal is mainly determined by the latent heat required to convert the liquid crystal from the nematic to the isotropic phase in volume $V_{1/2}$.[174] The radius of the isotropic bubble grows linearly with the absorbed heating power. The radius $R_{1/2}$ of the isotropic bubble required to generate half the steady state signal does not increase linearly with the heating power since the relation between the heating power and the signal is nonlinear (see fig. 4.11 (inset)). $R_{1/2}$ saturates for heating powers close to maximum transmission, which means, that the volume to be converted to the isotropic phase in the switch-on process is almost constant at larger heating powers. The studied steady state transmission range between 0.7 and 1 corresponds to this large heating power regime, and thus no dependence of the switch-on time on the heating power is observed.

In the switch-off case, the initial isotropic volume before switching the heating power off is still a linear function of the heating power. The signal drops from the stationary isotropic bubble radius to the half-signal radius $R_{1/2}$. Thus the time scale of the switch-off is still increasing with increasing heating power. The estimated time scales for the switch-on and switch-off process based on this consideration (see appendix 6.3 for a detailed calculation) are plotted in fig. 4.13 (a), scaled in y-direction, and confirm the observed trend. The switch-on and switch-off times differ as different processes are responsible for their time scale. The switch-on time depends on the rate at which the latent heat of the phase transition is supplied to the liquid crystal by the incident laser radiation, whereas the switch-off time results from the transport of the latent to the environment and thereby on the thermal diffusivity.

A more quantitative analysis requires considering the time-dependent heat equation including the phase transition. The dynamics of a liquid crystal phase transition involving a moving phase boundary can only be solved numerically. For this purpose, we employ the apparent heat capacity method.[93] This method introduces an apparent heat capacity at the phase boundary consisting of the heat capacity C of the liquid crystal and the latent heat H_f of the nematic to isotropic phase transition. We assume a spherically symmetric system neglecting the presence of the PVA/glass interfaces and the anisotropic thermal conductivity κ, which allows to transforming the heat equation with apparent heat capacity into spherical coordinates

$$\rho\left(C\frac{\partial T}{\partial t}+H_\mathrm{f}\delta(T-T_\mathrm{C})\right)=\frac{1}{r^2}\frac{\partial}{\partial r}\left(\kappa r^2\frac{\partial T}{\partial r}\right)+S \tag{4.20}$$

with ρ being the mass density and $\delta(T-T_\mathrm{C})$ the delta distribution. The term S represents a heat source present in the form of the gold nanoparticle. To be as close as possible to the experimental conditions, we include a steady heating effect caused by the probe laser in the source as well. Using the corresponding boundary conditions, we obtain the transient temperature profile in the liquid crystal numerically (see appendix 6.3). To obtain the optical signal from the temperature profile, we extract the radius of the phase boundary and employ eq. 4.17. The results of the numerical calculation are shown in fig. 4.13(b) and (c) for switch-on and -off process. The shown striking similarity to the experimental results further reveals the correct trends with increasing heating power (see fig. 4.13 (a)). The absolute time scale deviates by a factor of 2. We suppose that this deviation results from the influence of the probe laser heating the particle. Neglecting the influence of the probe laser in the simulations reveals a steeper response in the switch-on and the switch-off process as depicted by the dotted lines in fig. 4.13 (b) and (c). Thus the probe laser may play an important role in the dynamics of the optical switching process in the modulator structure. The deviations between experimental and numerical data result from the simplifications made to solve the time-dependent heat conduction equation including a moving phase boundary and to model the light propagation. Two of the assumptions are plane wave propagation for the optical signal and a spherical geometry of the phase boundary in the heat conduction model. A technically more defined model will lead to q quantitative agreement. The major physics is already captured by the simplified theory presented above.

4.3.2 Conclusion

We have presented a simple all-optical modulator based on an absorbing nanoparticle dissipating its excitation energy as heat. We use an inherently linear process, the absorption of a single absorbing nanoparticle, to modulate the transmission of the second beam of light using a driven phase transition of a liquid crystal. While the speed of the modulating structure is limited by the phase transition, the main goal of this report is to demonstrate that dissipative optical processes may provide a scheme to manipulate light as well. The performance of the device could easily be improved by using nanoparticles with a sharper and larger surface plasmon resonance like gold nanorods. Faster structures using Mach-Zehnder type interferometers where the optical phase in one interferometer arm is manipulated by optically controlled heating may speed up light modulation considerably.

Acknowledgement We acknowledge financial support from the European Union, the Free State of Saxony and the DFG Forschergruppe ”From Local Constraints to Macroscopic Transport”.

Chapter 5

Summary and Outlook

5.1 Summary of the Results

The advancing possibilities in material synthesis and sample preparation techniques have enabled unprecedented control over photons and electrons. A new task is the control of propagation of phonons. This aim requires suitable techniques for the characterization of thermal transport. Although several advanced measurement schemes do exist for the study of thermal transport on virtually all length and time scales, thermal transport studies are lacking a method that can measure thermal transport on the single particle level using far-field optical readout and only require small temperature increases. Single particle investigations will enable the measurement of the distributions of thermal transport parameters and will, thereby, shed new light on heat conduction and radiative thermal transport.

The developed single particle thermal transport measurement schemes are based on optically heated gold nanoparticles and possess far-field optical readout. Upon optical excitation plasmonic nanoparticle relax within picoseconds via nonradiative decay channels creating a localized temperature elevation. Then, this thermal energy is released into the environment. A temperature change is connected to thermal expansion that leads to a change in the refractive index. The heating induced refractive index change, which alters the propagation of a detection laser, is the basis for the photothermal contrast. Using a modulated heating laser and a continuous wave detection laser, photothermal microscopy can image absorbers ranging from single molecules[31] to plasmonic nanostructures.[35] The modulated detection scheme is the foundation of the method's high sensitivity and provides a time scale for the study of thermal transport. The observation that the amplitude of the photothermal signal drops with the modulation frequency and thereby depends on the thermal diffusivity was already made in the first experiments of single particle photothermal microscopy.[43,53] However, the accurate measurements of the thermal diffusivity were not possible due to the lack of a suitable model. The presented thermal diffusivity measurements are based on recent advances in the modeling of the photothermal signal.[26,28,30,48,119]

Here, it is also demonstrated that single gold nanoparticles could be used as sensors for thermal transport. This advance improves the sensing capabilities of single gold nanoparticles and enables thermal transport measurements of samples that were not accessible before. A second aspect of the thesis was the development of a photothermal light modulator based on a heated gold nanoparticle that is embedded into a surface-aligned liquid crystal film. Here, modulation amplitudes of up to 100 % were observed, which is orders of magnitude larger than photothermal signals of 10^{-4} to 10^{-3} which are typically present in photothermal microscopy. Using the photothermal contrast in liquid crystals, an all-optical modulation scheme was presented that is also promising for sensing applications.

Results of Sections 4.1 and 4.2: Measurement of Thermal Diffusivities

Photothermal microscopy is implemented as a modulated detection scheme where the heating laser is intensity modulated, and the detection laser senses variations at that particular frequency. The modulation amplitude of the detection laser is called photothermal signal. Besides the modulation amplitude, there is a phase delay between the modulation of the heating and the detection laser. This phase delay is the consequence of the thermal transport. Temperature profiles are not instantly built up, and then the maximal temperature rise is not in phase with the maximal heating intensity. This effect is utilized by the two detection schemes described in the following.

Photothermal Lensing Amplitude and phase delay of the frequency-dependent photothermal signal are measured at modulation frequencies between 10 kHz and 2 MHz. The modulation amplitude decreases with the modulation frequency as the modulation of the temperature profile is diminished. The phase delay between modulated optical heating and the detection laser increases. The measured modulation amplitudes at one frequency are broadly distributed due to the dispersion of the particle size and the signal's proportionality to the particle's volume. The statistical variation of the phase delay is much lower. The phase delays of different particles at one modulation frequency have approximately the same standard deviation as the difference between the phase delays of two measurements on the same particle. Therefore, the thermal transport is homogeneous in the sample, which is an expected result. The deviations are explained by the manual focusing. The data analysis relies predominantly on the phase delays because it is an absolute measure. The phase delay is only weakly dependent on the particle size and independent of the heating intensity assuming that the thermal diffusivity is temperature-independent. Therefore, a phase delay measurement at a single frequency is in principle enough to measure the thermal diffusivity.

To extract thermal diffusivities the photothermal signal has to be modeled. The model considers the thermal transport around a harmonically heated sphere which leads to a refractive index profile. The latter alters the propagation of the probe laser which is modeled by a generalized Lorenz–Mie theory.[26] The calculated photothermal signal is compared to the experiment to extract thermal diffusivities. If the aberrations of the probe laser beam are included in the model, the thermal diffusivity measured with photothermal lensing agrees with a laser flash measurement. Deviations between macroscopic and microscopic thermal transport measurements are not expected as the sample is homogenous and ballistic thermal transport is not expected for the polymer (PDMS).[175]

For the thermal diffusivity, an unexpected frequency dependence is observed. This deviation is not rooted in the approximation of the thermal transport in eq. 2.31 as the approximation $\tau_m = 0$ changes the phase delay by less than 10^{-3} rad. This artifact is attributed to the imperfect modeling of the detection laser focus. The photothermal signal in single particle microscopy always has two contributions, the thermal lens and the thermal scatterer. The share of each part depends on the modulation frequency. At high modulation frequencies, the damping of the thermal lens is much stronger than that of the thermal scatterer. The thermal scattering senses refractive index changes close to the nanoparticle. To the thermal lens, regions far away from the nanoparticle contribute as well. If the modeling of the laser focus is imperfect, the frequency dependence of the different contributions will result in a frequency-dependence of the thermal diffusivity. This effect is stronger for larger nanoparticles as the thermal scattering signal increases.

If thermal transport is studied with nanoparticles inside a liquid, the particles are diffusing freely. Whenever a nanoparticles passes the laser foci, a short signal burst is recorded. This burst still has a well-defined amplitude and phase delay. From time traces lasting 45 min histograms are created that count the number of events having a certain amplitude and phase delay. These histograms allow the measurement of water's thermal diffusivity which agrees very well with literature.

Photothermal Deflection The thermal transport is investigated in two dimensions using photothermal deflection. The intensity modulated laser heats the nanoparticle. The extended thermal lens deflects the detection laser scanned by galvanometer scanning mirrors. A split detector measures the deflection in one direction. Thereby, the propagation of thermal energy into the environment is probed. The detection laser beam underfills the back-aperture of the illumination objective to reduce spherical aberrations and clipping of the detection laser. The latter would additionally induce a photothermal lensing signal. Using a lock-in amplifier the in-phase and out-of-phase components of the deflection signal with respect to the optical heating are measured. The phase sensitive signals show spatial oscillations. However, the amplitude of the photothermal signal does not exhibit any spatial oscillations. The local extrema in the phase-sensitive signal result from the projection of the amplitude onto $\cos(\delta)$ and $\sin(\delta)$ with the phase delay δ.

Using a ray optics model the measured phase delays are fitted to extract the thermal diffusivity of the medium surrounding the nanoparticle. The measured values agree with a macroscopic laser flash measurement and the photothermal lensing variant. The phase delay images are spherically symmetric on the position of the gold nanoparticle except at small impact parameters where no deflection is present. The spherical symmetry is expected due to the isotropic, homogenous thermal transport in PDMS. In a nematic liquid crystal, the spherical symmetry is lost, and the phase delay images become elliptic. The orientations of semi-minor and semi-major axes agree very well with a polarization contrast measurement. The anisotropy of the thermal diffusion length is lower than expected from a numerical calculation. This result is explained by the position of the gold nanoparticle which is located at the glass liquid crystal interface lowering the anisotropy of the thermal diffusivity. The result demonstrates the potential of photothermal deflection to study thermal transport at interfaces.

In the liquid crystal (5CB), the phase delay decreases for small impact parameters. Once the impact parameter is larger than the beam waist of the detection laser, the phase delay increases. At long distances, the phase delay increases linearly. Here, thermal transport is studied in the nematic phase. At small distances, the detection laser heats the nanoparticle due to the large refractive index of the liquid crystal that shifts the plasmon resonance of the nanoparticle to the red. Therefore, the phase transition from the nematic to the isotropic phase is driven in an extended volume increasing the phase delay. This observation has the potential to enable the study of phase transitions in liquid crystals in greater detail as well as other materials.

Comparison of Photothermal Lensing and Deflection This thesis presented two variants of single particle photothermal microscopy that allow the study of thermal transport using single nanoparticles and far-field optical readout. The differences are as follows: In the photothermal lensing approach, the detection laser overfills the back-aperture of the illumination objective and both laser beams are fixed on each other. In the photothermal deflection experiment, the detection laser underfills the illumination objective. The heating laser remains fixed on the particle, and the detection laser is scanned probing the full thermal lens. The photothermal lensing signal has two different contributions, the thermal lens and the thermal scatterer. The presence of both mechanisms requires the use of electromagnetic optics to model the signal quantitively. At large impact parameters, the thermal lens is the only contribution to the deflection signal. Therefore, a simple ray optics model is enough to calculate the phase delay quantitively. The simple modeling makes the deflection implementation more appealing for future experiments were more complex sample geometries shall be studied. Photothermal deflection is used to study thermal transport in an anisotropic sample. Photothermal lensing can measure thermal diffusivities inside liquids.

Results of Section 4.3: Photothermal Intensity Modulator

Nematic liquid crystals are optically anisotropic materials that alter the polarization state of light. Into an aligned liquid crystal film, single gold nanoparticles are embedded. The liquid crystal layer acts as a half-wave plate which is achieved by choosing the appropriate layer thickness. Light is linearly polarized at a 45° angle on the principal axes. The liquid crystal film rotates the light by 90°. The whole sample is heated close to the nematic to isotropic phase transition temperature where the optical anisotropy is lost. Now, an optical heating of the gold nanoparticle can cause the phase transition over the whole sample thickness. The polarization of a linear polarized probe laser is not rotated any more. Using a polarizer that is parallel to the incident polarization, the intensity of the detection laser is modulated.

In the experiment, the transmission of the detection laser is studied when the nanoparticle is optically heated. A heating of the whole sample controls the gain of the photothermal modulator. At the sample temperature closest to the phase transition, 220 nW absorbed power or 1 K temperature increase at the particle's surface can change the transmission signal by up to 20 %. The biggest drawback of this intensity modulator are the low switching rates due to the phase transition. The closer the modulator is operated at the phase transition temperature the slower it gets. The switch-on time is limited by the rate at which heat is provided for the phase transition. The switch-off depends on the transport of thermal energy into the environment. For the studied heating powers, the time to switch from 0 to 50 % transmission is independent of the heating power. For larger heating powers the switching time would decrease. This decrease would increase the switch-off times from 100 % to 50 % transmission as more thermal energy has to be dissipated.

5.2 Outlook

This thesis has demonstrated the applicability of photothermal microscopy to the study of thermal transport and the control of light transmission. Now, some experiments are described where the developed techniques can be employed, and some possible perspectives of future research are given.

Single Laser Beam Photothermal Microscopy The throughout understanding of the frequency-dependent photothermal lensing signal has already resulted in a variant of photothermal microscopy that only requires a single laser beam. The single beam detection scheme can discriminate between absorbers and scatterers.[142] Scattering is an almost instantaneous process whereas absorption creates the thermal lens. At high modulation frequencies, the maximal temperature elevation and maximal heating intensity are phase-delayed. Using a heating laser that is intensity modulated with an offset, absorbers are selectively imaged in the presence of scatterers. The scattering signal is always in phase with the modulation. The absorption also results in a component that is out-of-phase. The described properties are the basis for the selective imaging of absorption.

Single beam photothermal microscopy will simplify absorption measurements using photothermal microscopy. The use of a single laser makes the imaging scheme simpler to set up and more robust compared to pump-probe detection schemes. The biggest drawback is the lower signal to noise ratio. Using a detection laser beam with radially balanced annuli the signal to noise could be enhanced and the scattering signal reduced.[27,176] The large scattering signal might be the reason for a cross-talk between in-phase and out-of-phase signal which creates an out-of-phase signal for pure scatterers. With this optimization single beam photothermal microscopy could be used for selective imaging of gold nanoparticles in biological systems.

Thermal Transport Studies using Photothermal Lensing To improve the precision of the thermal transport studies using photothermal lensing an autofocus system should be implemented. The manual focusing was the primary random error source in the measurement. A concern in the measurements was the accuracy of the method as aberration influences the experiment. Here, different approaches are possible: The illumination objective could be underfilled to reduce spherical aberrations. A second more demanding approach is the correction of the aberrations which could also be performed in real-time.[177,178] The study of thermal transport in heterogeneous samples like polymer films and cells should include a monitoring of the aberrations. The control is important to exclude the possibility that heterogeneous thermal transport might only be a measurement artifact due to heterogeneities of the refractive index.

Thermal Transport Studies using Photothermal Deflection The photothermal deflection measurement could be improved by using a quadrant photodiode. Then, the photothermal deflection would be measured in two orthogonal directions enabling the reconstruction of the direction of the deflection. This modification would improve the sensitivity for the measurement of anisotropic and heterogeneous thermal transport. Possible experiments using photothermal deflection are the following: Energy transport in chains of plasmonic nanoparticles,[144] thermal transport through interfaces,[179] and transport in stretched polymer samples.[23] Especially the latter measurement of the strain-dependent anisotropy of the thermal conductivity is not possible with current techniques. A first approach using a polymer (PDMS) failed due to significant spherical aberrations. High numerical aperture objectives are optimized for well-defined refractive indexes. For significant refractive index mismatches like 0.1, large spherical aberrations occur that make the measurement impracticable. This deviation occurs if a PDMS substrate is used instead of glass. Again this challenge can be solved by aberrations corrections.[178]

Photothermal Light Modulator The biggest limitation of the photothermal light modulator is the low operation speed. The switching rates could likely be enhanced if the switch is integrated into an optical fiber. The volume in which the phase transition is modulated could be reduced, and the nanoparticle could be placed in the center of the liquid crystal. This adaptation would significantly enhance the operation speed. The biggest strength are the large modulation amplitudes at moderate heating powers. This feature makes the light modulator structure applicable as a sensor for acoustic waves and an amplifier. The amplifier could be used to detect objects that absorb very weekly and are not able to drive the nematic-isotropic phase transition of the liquid crystal. The modulator would be prepared in the state where the transmission change with temperature is the largest. Then a small heating by a weak absorber would cause a large change in the transmission of the detection laser. The other possible application of the light modulator is the sensing of acoustic waves. The nanoparticle is heated, and a phase boundary in a particular distance is created. This phase boundary is then deformed by an acoustic wave and would induce a change in the transmission signal.

Photothermal Lensing and Phase Transitions A more refined model of the photothermal signal that includes phase transitions has tremendous potential. Based on the latter the phase transition in the liquid crystal can be studied in greater detail, and latent heat capacities can be measured. A more detailed model could be used to identify the optical parameters of sample temperature, heating and detection laser intensities and modulation frequencies. The largest observed enhancement factor compared to glycerol is 20, which is surprisingly small. Thereby, the sensitivity of photothermal microscopy could be enhanced, and the system is easier use than a pressurized xenon gas.[130] In general, the interesting phenomenology of the photothermal signal in liquid crystals could be studied in detail.[127,128] The observed behavior could be explained using thermal transport and scattering calculations compared to a phenomenological model.

Sensing based on the Measurement of Thermal Transport The study of thermal transport is not only interesting due to fundamental interest and for material research, but also due to its applicability as a sensor. A change in the thermal transport around a nanoparticle can give much information. One example is single particle tracking of a gold nanoparticle dispersed in water at interfaces using photothermal microscopy. By measuring the thermal diffusivity, the relative distance between the gold nanoparticle and the interface can be determined if the interface has a thermal diffusivity differing from the solvent. Heat transport based molecular binding essays could also be performed with single nanoparticles.[155]

Chapter 6

Appendix

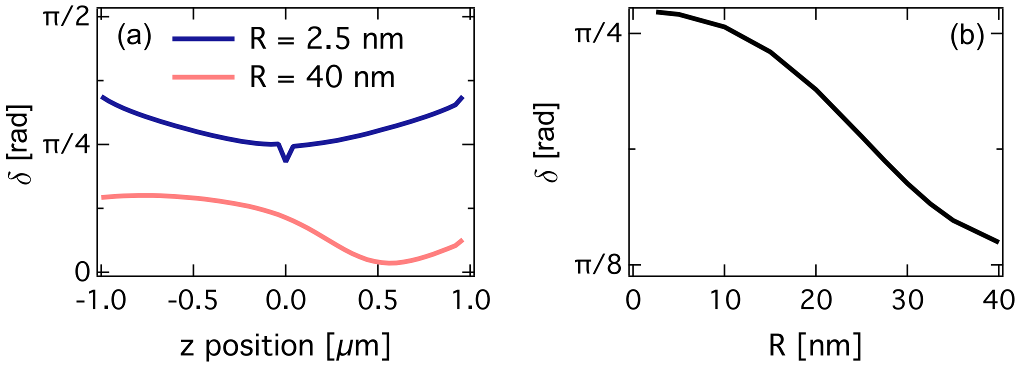

Figure 6.1: (a) Calculated phase delay for two differently sized gold nanoparticles at $R_{\mathrm{th}} = 150\,\mathrm{nm}$ assuming a Gaussian intensity profile in der Laser focus in PDMS. (b) Phase delay for nanoparticles with different diameters at $z = -320\,\mathrm{nm}$.

6.1 Supplementary Information for Section 4.1

6.1.1 Sensitivity of the phase delay to parameter changes

Calculations have also been performed for Gaussian beams, which significantly decreases computation times and still captures the main dependencies. It is found that the optically detected phase delay depends on the particle size (see fig. 6.1 (a) and (b)), refractive index, the detection aperture and the characteristic of the incident detection laser beam. The size dependence results from the fact that the heated gold nanoparticle with the refractive index profile acts as a modulated scatterer and a thermal lens at the same time. The contribution of either mechanism changes with particle size. For small particles the thermal lensing is dominant whereas for large particles the scattering contribution is considerably enhanced.[143] A size dispersion of 12% and an average radius of $R = 5\,\mathrm{nm}$ result in an error of the measurement of the thermal diffusivity of less than 1%.

The temperature dependence of the thermorefractive coefficient of the surrounding material and the ∂n_{T} of the nanoparticle alter the results of the calculation only weakly. This has the effect that the frequency dependencies of photothermal signal's amplitude and phase delay do not depend on the heating power. We find that the displacement between both laser foci along the optical axis does not change the phase delay in the distance dependence between the nanoparticle and the detection laser focus (see fig. 6.1 (b)). The displacement between detection and heating laser alters amplitude and position of the maximal photothermal signal.[26] Therefore, the phase delay at the position with maximal signal amplitude is changed. In section 4.1 only numerical calculations using exact beam descriptions are compared to the experimental data to obtain the thermal diffusivity of the material surrounding the gold nanoparticle.

6.1.2 Correction of the phase delay

The acoustooptic modulator and the photodiode have phase delays that depend on the modulation frequency. To correct for that the phase delay of the modulated heating laser ϕ_{heat} is measured. This phase delay is very stable and only change by less than 0.001 rad over days. The phase delay which

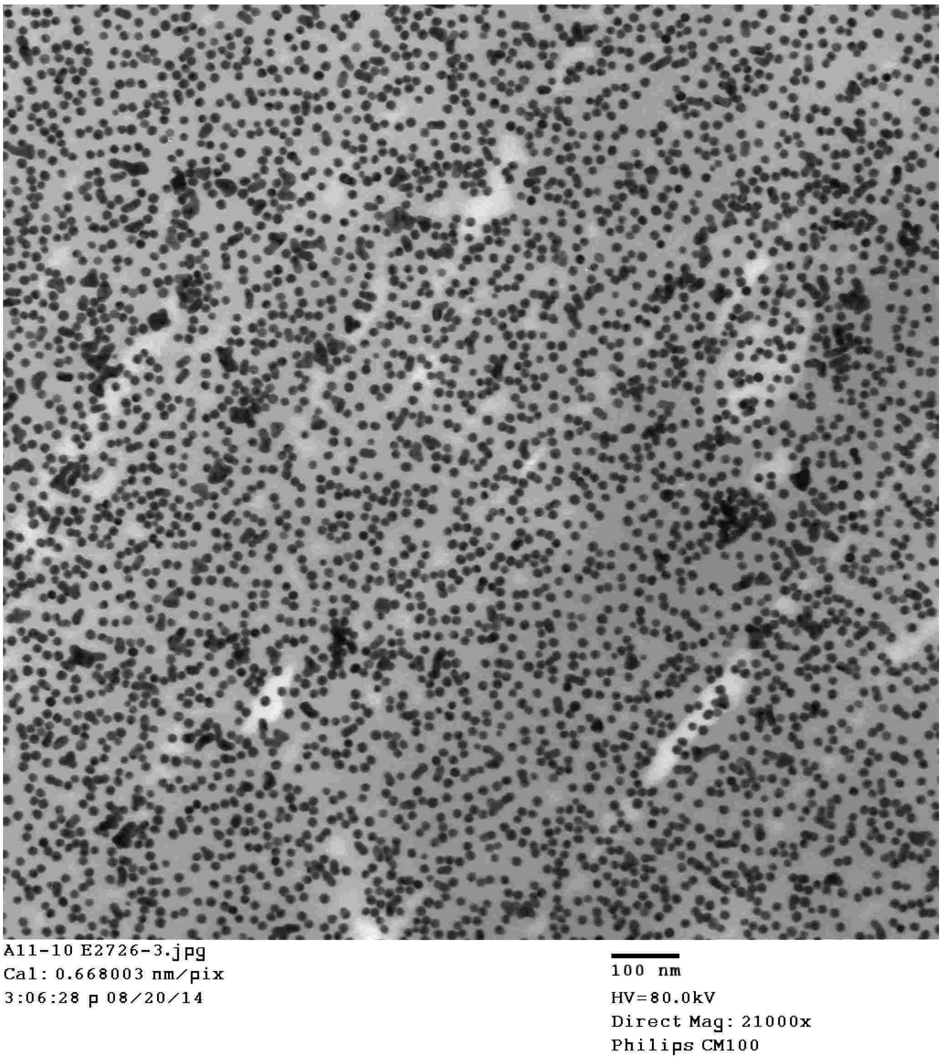

Figure 6.2: Transmission electron micrograph of gold nanoparticles with 5 nm in radius. Kindly supplied by Nanopartz Inc.

is induced by the thermal transport ϕ is calculated by subtracting ϕ_{heat} from the phase delay measured by the lock-in amplifier.

6.2 Supplementary Information for Section 4.2

6.2.1 Fit of the ray optics model to the line profiles of the phase delay

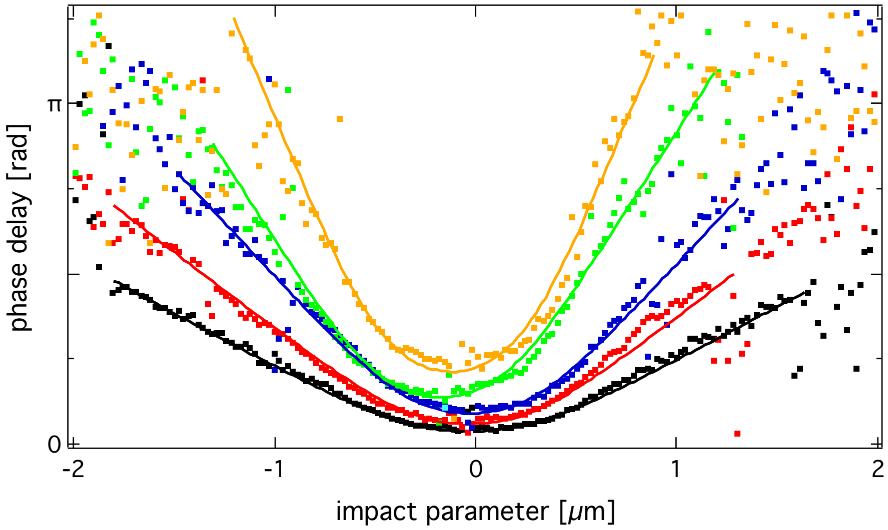

Figure 6.3: Line profiles of the phase delay (squares) between deflection signal and time-harmonic optical heating as well as the corresponding fit (solid lines) at 50 (black), 100 (red), 200 (blue), 400 (green) and 1000 kHz (orange).

6.2.2 Reference measurement for anisotropic thermal transport

Here, we show the reference experiment for the anisotropic thermal transport. We conduct this measurement in the isotropic medium PDMS to validate that photothermal deflection is capable of quantifying anisotropies in the thermal transport. The anisotropy of the thermal transport is determined in two different ways.

Least-square fitting of ellipses Contour lines are determined from the phase delay images (see fig. 6.4 (a)). The anisotropy is determined by fitting an ellipse to the experimental data and calculating the fraction of semi-major a and semi-minor axes b (see fig. 6.4 (b)).[161] For distances larger than 800 nm the fraction gives the expected result being close to one. The deviation for small impact parameters results from the fact that the interaction between light and refractive index profile is more complex than assumed by our simple ray optics model. The ray optics model is not expected to give perfect agreement for impact parameters smaller than the beam diameter. The phase delay for large impact parameters is well suited to detect anisotropies in the thermal transport.

Linear fitting to straight tails For large impact parameters, the phase delay increases proportionally to the distance of the nanoparticle. From the phase delay images (see fig. 6.5 (a)) line profiles are extracted between −60° and 60° with respect to the deflection direction at 5° increments (see fig. 6.5 (b)). Then linear functions are fitted to the line profiles for impact parameter from 800 to 1500 nm.

The fitted slopes are the inverse thermal diffusion length which is plotted in fig. 6.5 (c). The thermal diffusion lengths for the different direction have a statistical variation of about 2%.

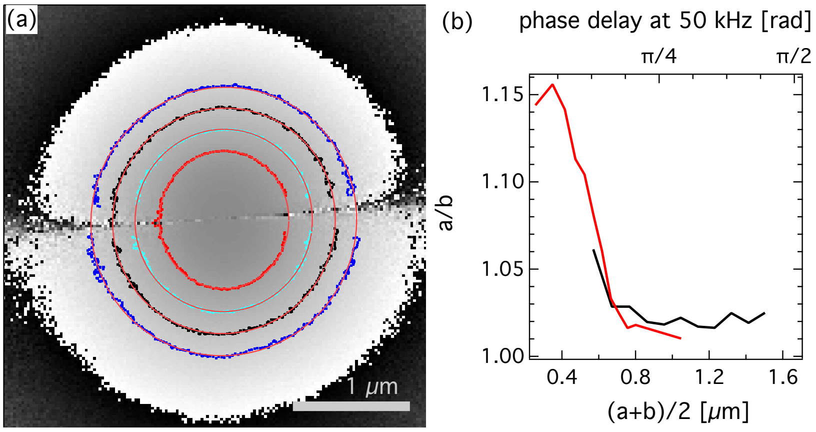

Figure 6.4: (a) Phase delay image at 200 kHz modulation frequency with contour lines at 0.4 (red), 0.6 (light blue), 0.8 (black) and 1.0 rad (blue) and the corresponding ellipse least-square fits (thin red lines). (b) The extracted fraction of semi-major a and semi-minor axes b are plotted against the average radius at 50 (black) and 200 kHz (red).

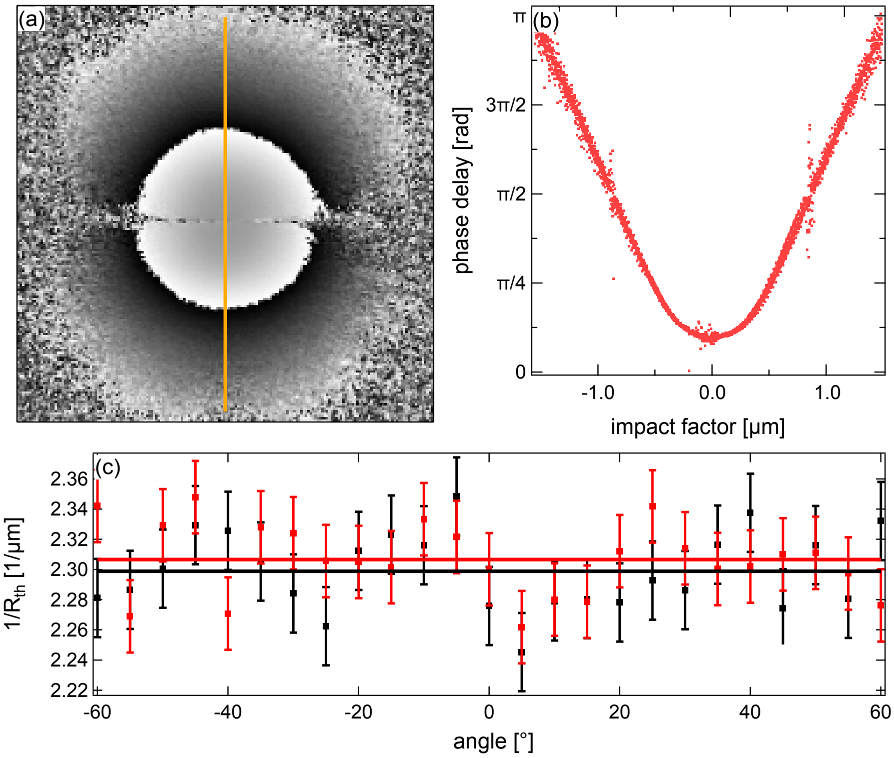

Figure 6.5: (a) Phase delay of the deflection signal with respect to the time-harmonic heating at 200 kHz. Measured deflection direction (orange line). (b) Extracted phase delays at angles between $-60°$ and $60°$ with respect to the deflection direction. (c) Slopes of the linear fits to the phase delays for the left part (black) and right part (red) of the line profiles of the phase delay. The solid lines show the average slope.

6.2.3 COMSOL calculation

The heat transport is calculated using COMSOL assuming an unidirectional anisotropic thermal transport with a heat capacity of $C_p = 2000\,\mathrm{J\,m^{-3}}\,K^{-1}$, a density of $\rho = 1000\,\mathrm{kg\,m^{-3}}$, thermal conductivity of $0.30\,\mathrm{W\,m^{-1}\,K^{-1}}$ along the extraordinary axis and $0.15\,\mathrm{W\,m^{-1}\,K^{-1}}$ along the ordinary axes.[102] The heat source is 30 nm in radius and harmonically modulated at 200 kHz. The calculation is performed for ten modulation cycles. Then the phase delay for each distance is determined using the last two cycles of the calculation. Using affine fits the thermal diffusion length is extracted. The thermal diffusion length is 653 nm along the extraordinary axis, 483 nm along the ordinary and 555 nm at a 45° angle with respect to the latter axes (see fig. 6.6). The anisotropy of the thermal diffusion length is 35%.

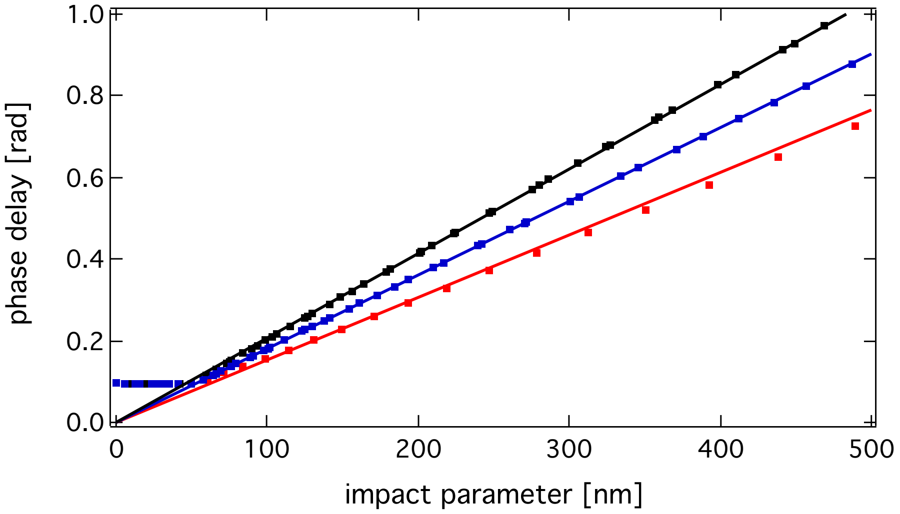

Figure 6.6: Calculated phase delay (squares) along the extraordinary (red), ordinary (black) and at a 45° angle with respect to the principal axes (blue) in 5CB at a modulation frequency of 200 kHz. The solid lines show the affine fits to extract the thermal diffusion length.

6.2.4 Deflection amplitude in 5CB

For small distances and large signal amplitudes, the photothermal deflection is mirror symmetric with respect to the horizontal line where no deflection is detected. Here, the phase transition is modulated (see fig. 6.7 (a)). This statement is supported by the comparison of the line profile in 5CB with the PDMS one (see fig. 6.7 (b)). The 5CB line profile is already damped for smaller distances which are caused by the nonlinearity of the refractive index if the phase transition is modulated.[101] For larger distances, the phase transition is not modulated anymore, and the deflections become anisotropic due to the anisotropic thermal conductivity.

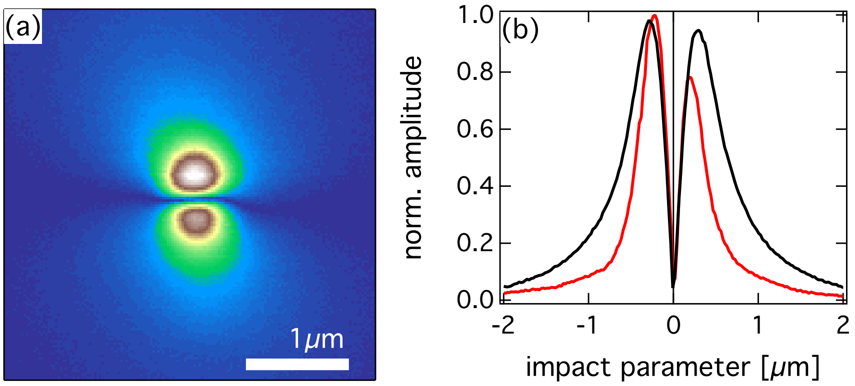

Figure 6.7: Photothermal deflection amplitude at modulation frequency 50 kHz. (a) Image of the deflection amplitude and (b) the corresponding deflection amplitude compared to PDMS

6.3 Supplementary Information for Section 4.3

6.3.1 Characterization of the Liquid Crystalline Domains

The orientation angle of the director Ψ_D, retardation β and twist angle ϕ of the liquid crystal sample are determined using the polarization contrast method described by Duran et al.[135] Therefore raster scanned polarization contrast images are recorded at different polarization angles like in fig. 6.8 (a). For each polarization an image is recorded with the analyzer being parallel and perpendicular to the polarizer. A fit of the intensity as a function of the polarization angle by eq. 3.9 and 3.10 for each pixel yields the parameters locally characterizing the liquid crystalline domains.[135] For the fit procedure $\phi = 0$ is assumed as only one glass cover slide is rubbed unidirectionally. The liquid crystal chamber is formed by a rubbed and an untreated PVA coated cover slip creating untwisted liquid crystalline domains. The results for the orientation of the director and retardation are shown in fig. 6.8 (b) and (c). The images show domains where the director is centred around $\Psi_D = 14°$ and the retardation around $\beta = 90°$ (see the histograms in fig. 6.8 (d) and (e), respectively). The orientations of the domains are given with respect to the coordinate frame of the polarizer. The results presented in section 4.3 were measured on the particle which is in the black box in fig. 6.8. The particle is not visible in the polarization contrast image as the probe laser is not focused on the particle.

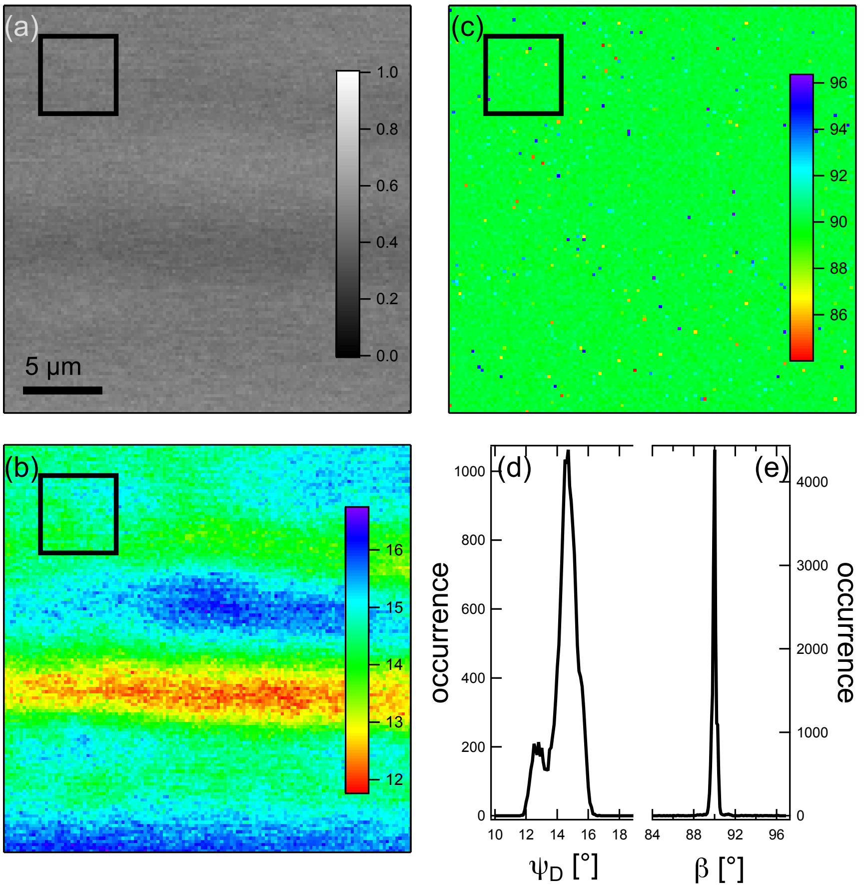

Figure 6.8: (a) The polarization contrast measurements yield (b) the orientation and (c) the retardation of the liquid crystalline sample. The dots in (c) are random errors of the retardation. From these images the histograms of (d) the orientation and (e) the retardation are calculated.

6.3.2 Incident Heating Power, absorbed Power and Particle Temperature

The incident heating power P_0 used in section 4.3 is the power of the heating laser which is measured in front of the focusing objective. See figure 3.1 (a) for sketch of the setup. Here die signals of the photodiode are recorded by the Adwin-Gold. Using this power and the beam waist ω_h, the peak intensity I_0 in the focus of the beam is calculated via $2P_0 = I\pi\omega_\mathrm{h}^2$.[159] The absorbed power $P_\mathrm{abs} = I_0\sigma_\mathrm{abs}$ is calculated from this intensity I_0 and absorption cross-section σ_abs at 532 nm. As the focusing objective is overfilled the incident heating power P_inc after the objective is lowered by approximately 50 %.[26] Taking this into account, the temperature on the surface of the particle ΔT_S is computed via the resulting steady state $1/r$ temperature profile

$$\Delta T_\mathrm{S} = T_\mathrm{S} - T_0 = \frac{P_0\sigma_\mathrm{abs}}{2\pi^2\kappa R\omega_h^2} \tag{6.1}$$

where $\sigma_\mathrm{abs} \approx 10^{-14}\,\mathrm{m}^2$ is the absorption cross-section of a $R = 30\,\mathrm{nm}$ sized gold nanoparticle at $\lambda_\mathrm{h} = 532\,\mathrm{nm}$ in 5CB, $\omega_\mathrm{h} = 270\,\mathrm{nm}$ is the beam waist and $\kappa = 0.15\,\mathrm{W\,m^{-1}K^{-1}}$ the average thermal conductivity of the liquid crystal 5CB.[102] This calculation yields a 10 K temperature increase of the particle per $10\,\mu\mathrm{W}$ incident heating power which is about five times larger than the value determined by the experiments in section 4.3. The primary reason for this deviation is likely the overestimation of I_0 due to the presence of aberrations which lower the heating laser intensity incident on the particle.[26] To quantify this contribution rigorous scattering calculations are necessary. ΔT_S will be further reduced due to the nearby glass interface[173] which has a seven times higher thermal conductivity than 5CB. Also, the nanoparticle is not necessarily in the focus of the heating laser beam, thus reducing the intensity further. All these effects lower the temperature reached on the nanoparticle's surface. Based on that consideration we estimate that $P_\mathrm{inc} = 10\,\mu\mathrm{W}$ correspond to $P_\mathrm{abs} = 260\,\mathrm{nW}$. This results to a surface temperature increase of $\Delta T = 1.1\,\mathrm{K}$.

6.3.3 Calculated Temperature Profiles

The numerical evaluation of the optical signal requires the numerical solution of eq. 4.20. It yields transient temperature profiles $T(r,t)$ from which the radius of the nematic-isotropic boundary $R_\mathrm{C}(t)$ is computed from the condition $T(R_\mathrm{C},t) = T_\mathrm{C}$. The calculation is performed using COMSOL Multiphysics into which the apparent heat capacity method[93] is implemented. The calculation of the switching on process starts at a constant temperature T_0 and a phase transition occurring at $T_\mathrm{C} - T_0 = 0.2\,\mathrm{K}$. At $t = 0$ the heat source is switched on and the temperature profile starts to build up. The steady state temperature of the nanoparticle is reached within a few hundred nanoseconds. Somewhat later, the stationary temperature is approached also further away from the particle. After approximately 10 ms the steady state temperature is established $3\,\mu\mathrm{m}$ away from the nanoparticle (see fig. 6.9 (a)). The resulting optical signal is plotted in fig. 4.13 (b).

The radius $R_\mathrm{C}(t)$ at which the phase transition occurs is visible as a kink in the transient temperature profile. At this position, thermal energy is used to change the phase from the nematic to the isotropic one. Afterward, the temperature is increased further. In general, the time interval required to establish the steady state temperature profile is considerably longer if a phase transition is present but its shape is not affected. The steady state $1/r$ temperature profile only depends on the thermal conductivity

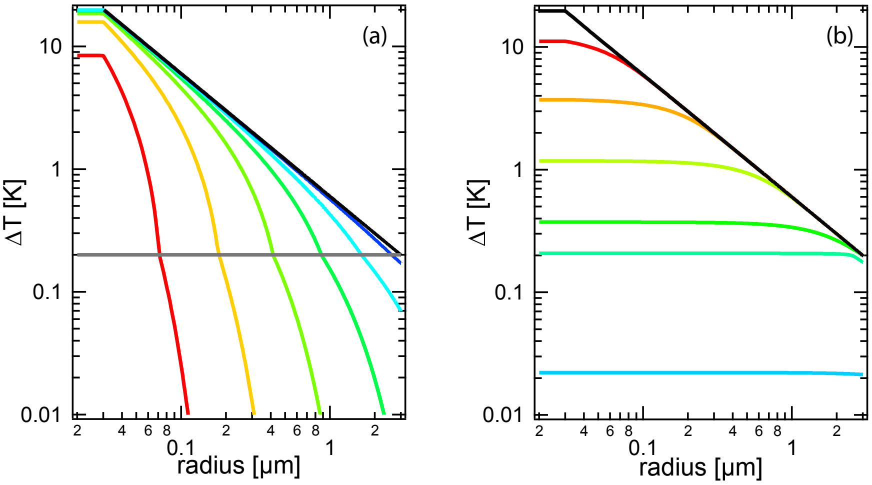

Figure 6.9: Numerically calculated transient temperature profiles for (a) the switching on and (b) the switching off process. (a) shows the transient temperature profiles from left to the right at 10 ns (red), 100 ns (orange), 1 μs (light green), 10 μs (green), 100 μs (green), 1 ms (light blue) and 10 ms (blue) after the switch-on process and (b) are same times for the switching off. The solid black lines show the temperature profile of a stationary point-like heat source where the surface temperature of a $R = 30\,\mathrm{nm}$ is increased by 20 K.

which is not assumed to change. Indeed, the change of the average thermal conductivity is negligibly small.[102]

For the calculation of the switching off process the calculation starts with an initial $1/r$ profile for a point-like heat source and the source term S is set to zero. As $T = T_C$ is reached latent heat has to be dissipated first. This has the effect that the temperature profile remains close to that temperature for a rather long time over a large volume. Strong temperature gradients are dissipated first (see fig. 6.9 (b)). The optical signal is computed via eq. 4.17 and also plotted in fig. 4.13 (c).

6.3.4 Analytical Model

The aim of the analytical model is to derive the changes of the times needed to reach 50% of the transmission after switching on or switching off the modulator as the absorbed power P_{abs} increases. From the optical signal the radius of the isotropic bubble R_C can be calculated. Take eq. 4.17 and equal the transmission $\mathfrak{T}$ to one half of the steady state case. The corresponding radius $R_{1/2}$ is computed by solving eq. 4.17 for

$$R_{1/2}(\Delta T) = d - \frac{\lambda}{\pi \Delta n} \arccos\left(\sqrt{\frac{\mathfrak{T}(\Delta T)}{2}}\right). \tag{6.2}$$

The radius corresponding to the steady state is computed via the steady state $1/r$ temperature profile. Here, we consider the switch-on process first. The time needed for the change of the transmission from zero to one half of the steady state is expected to be limited by the time it takes to melt the respective nematic volume $V_{1/2} = 4/3\pi R_{1/2}^3$.[174]

$$\Delta t = \frac{Q_L}{P_{\mathrm{abs}}} = \frac{\rho H_L V_{1/2}}{4\pi\kappa R \Delta T_S}. \tag{6.3}$$

Here, the time Δt to build up the temperature profile is determined by the quotient of the latent heat Q_{L} and the absorbed power P_{abs}. In this approach, the specific heat is neglected which is approximately of the same size depending on integration constants.[174] The curve is shown in fig. 4.13 (a) (red line) and scaled in the y-direction to fit the experimental data as this derivation is only qualitative.

Next, we consider the model for the switch-off process. The basis for the following will be Fourier's first law $\dot{\mathbf{q}} = -\kappa \nabla T$, where $\dot{\mathbf{q}}$ is the heat flux per time and surface area. If the equation is integrated over a closed surface O the dissipated power $\frac{\partial Q}{\partial t}$ is calculated. The integral form of Fourier's first law is

$$\frac{\partial Q}{\partial t} = -\kappa \oint_{O} \nabla T \cdot d\mathbf{A}. \tag{6.4}$$

∇ is the gradient operator in spherical coordinates. As the problem is spherically symmetric the derivatives with respect to the polar ϕ and the azimuthal angle θ vanish. As any closed surface around the point-like heat surface gives the dissipated power by the point-like heat source a sphere with the radius R' is taken. Therefore $\mathrm{d}\mathbf{A}$ becomes $\mathbf{e}_{\mathrm{r}}\mathrm{d}A$ where spherical coordinates are taken for the integration and consequently $dA = R'^2 \sin(\theta) d\phi\, d\theta$

$$\frac{\partial Q}{\partial t} = -\kappa \int_0^{\pi} \int_0^{2\pi} \frac{\partial T}{\partial R'} \mathbf{e}_{\mathrm{r}} \cdot \mathbf{e}_{\mathrm{r}} R'^2 \sin\theta \,\mathrm{d}\phi\, \mathrm{d}\theta. \tag{6.5}$$

The temperature gradient $\frac{\partial T}{\partial R'}$ is assumed to be constant on the whole integration surface and the gradient of the steady state is chosen. If this integration is performed and the difference quotient are plugged in one gets

$$\frac{\Delta Q}{\Delta t} = -\kappa 4\pi R'^2 \frac{\Delta T}{\Delta R'}. \tag{6.6}$$

For the gradient $\frac{\Delta T}{\Delta R'}$ the values for R_1 and $R_{1/2}$ are plugged in. And for the surface O the average radius $[R_1 + R_{1/2}]/2$ is taken. This leads to

$$\Delta t = -\frac{H_{\mathrm{L}}\rho(V_1 - V_{1/2})}{\kappa\pi(R_1 + R_{1/2})^2 \frac{T(R_1) - T(R_{1/2})}{R_1 - R_{1/2}}}. \tag{6.7}$$

The results are scaled in the y-direction and plotted in fig. 4.13 (a) (blue line). This equation gives the time needed to dissipate the latent heat of the isotropic to nematic phase transition of the volume $V_1 - V_{1/2}$. Equation 6.7 can also be viewed as the time interval Δt it takes for a point-like with the power P_{abs} to dissipate a certain thermal energy ΔQ. This time interval is only a lower bound for the switching off process as the specific heat has to be dissipated as well and the steady state gradient is always larger than the actual temperature gradient present (see fig. 6.9 (b)). But this approach should show the dependence of the switching off time with increasing absorbed power.

6.4 Author Contributions to the Peer Reviewed Journal Articles

The purpose of this section is to state the contributions of each author to the peer reviewed journal articles forming the main part of this dissertation.

Thermal diffusivity measured using a single plasmonic nanoparticle[160] André Heber designed and performed the photothermal lensing experiment as well as the data analysis. The laser flash measurement was performed by Felix Fahrnbauer and André Heber. The electromagnetics optics model was developed and implemented by Markus Selmke and modified by André Heber to match the requirements for the data analysis. The manuscript was drafted by André Heber and subsequently edited by all authors. All authors discussed the results. The study was conceived by Frank Cichos and Markus Selmke, and supervised by Frank Cichos.

Thermal Diffusivities Studied by Single Particle Photothermal Deflection Microscopy[180] André Heber designed, performed the experiment as well as the data analysis. The ray optics model was implemented by Markus Selmke and modified by André Heber to match the needs for the data analysis. The manuscript was drafted by André Heber and subsequently edited by all authors. All authors conceived the study and discussed the results. The study was supervised by Frank Cichos.

Metal Nanoparticle Based All-Optical Photothermal Light Modulator[145] André Heber designed, performed the experiment as well as the data analysis. The model required for the data analysis was developed by André Heber and Markus Selmke. Numerical calculation were performed by André Heber and Frank Cichos. The manuscript was drafted by Frank Cichos and André Heber subsequently edited by all authors. Frank Cichos and André Heber conceived the study. All authors discussed the results. The study was supervised by Frank Cichos.

Declaration

I hereby certify that this thesis was written by the author himself and that no means of help were used other than those mentioned in the text. All work and thoughts from other authors and sources have been duly acknowledged and clearly marked as such in the thesis.

I hereby name Andrea Kramer, Martin Fränzl and Prof. Frank Cichos as the only persons who assisted the author during the compilation of this thesis by careful reading and helpful comments. Markus Selmke and Prof. Dr. Frank Cichos contributed to the research and the publications that are the basis of this thesis. The contributions to the different sections in chapter 4 are given in detail in appendix 6.4.

Apart from the above mentioned individuals, no other person has been involved in the process of the compilation and work on the present thesis. Especially, no attempt has been made to make use of doctoral consulting. No other individuals have received payment of any kind by the author, neither direct nor indirect, for work which is connected with the contents of this thesis.

I further certify that this neither this thesis nor any derivative thereof has been submitted or presented to any other examination department for the purpose of achieving a PhD. Neither has it been presented to any other examination office and has not yet been published in its full form.

No earlier attempts to achieve a PhD degree have been made.

I acknowledge the doctoral regulations of the faculty of physics and geosciences (Promotionsordnung der Fakultät für Physik und Geowissenschaften) dated 24th August 2016 in their full sense.

(André Heber)

Acknowledgements

At this point, I would like to thank the people who made this work possible. First and foremost I thank Prof. Dr. Frank Cichos for giving me the opportunity to work on the topic and his stimulating ideas and discussions. I am grateful for his constructive critique, advice and guidance, the freedom to follow my idea and the creation of a pleasant working conditions.

I thank Dr. Markus Selmke whose work on the theory of photothermal microscopy was one foundation of the thesis and who helped me to get a deeper understanding of the physics involved in photothermal microscopy. I am grateful to Romy Schachoff improving the photothermal microscope and fighting together the immortal electronic oscillations. I also thank Prof. Dr. Klaus Kroy for fruitful discussions.

I thank the whole the whole mona group for providing a nice working climate and providing numerous cakes. I especially thank Marco Braun, Andreas Bregulla and Martin Fränzl for sharing the office. I thank Andrea Kramer for guiding me through the administrative jungle.

In addition, I thank Andrea Kramer and Martin Fränzl for carefully proof-reading of the manuscript.

I further thank the Free State of Saxony and the European Union and the SFB TRR 102 for funding as well as the Research Academy Leipzig and Graduate School BuildMoNa for financial support.

I thank my Family, especially Anett and Nora Böhme, for enriching my life and for supporting me all the way.

Bibliography

[1] J. S. Donner, G. Baffou, D. McCloskey, and R. Quidant. Plasmon-Assisted Optofluidics. *ACS Nano*, 5(7):5457–5462, 2011.

[2] E. Rousseau, A. Siria, G.e Jourdan, S. Volz, F. Comin, J. Chevrier, and J.-J. Greffet. Radiative heat transfer at the nanoscale. *Nat. Photon.*, 3(9):514–517, 2009.

[3] X. Zhang and L.-D. Zhao. Thermoelectric materials: Energy conversion between heat and electricity. *J. Materiomics*, 1(2):92–105, 2015.

[4] R. B. Wilson and D. G. Cahill. Limits to Fourier theory in high thermal conductivity single crystals. *Appl. Phys. Lett.*, 107(20):203112, 2015.

[5] W. J. Parker, R. J. Jenkins, C. P. Butler, and G. L. Abbott. Flash Method of Determining Thermal Diffusivity, Heat Capacity, and Thermal Conductivity. *J. Appl. Phys.*, 32(9):1679–1684, 1961.

[6] C. A. Paddock and G. L. Eesley. Transient thermoreflectance from thin metal films. *J. Appl. Phys.*, 60(1):285–290, 1986.

[7] O. M. Wilson, X. Hu, D. G. Cahill, and P. V. Braun. Colloidal metal particles as probes of nanoscale thermal transport in fluids. *Phys. Rev. B*, 66(22):224301, 2002.

[8] J. Huang, J. Park, W. Wang, C. J. Murphy, and D. G. Cahill. Ultrafast Thermal Analysis of Surface Functionalized Gold Nanorods in Aqueous Solution. *ACS Nano*, 7(1):589–597, 2013.

[9] J. Park and D. G. Cahill. Plasmonic Sensing of Heat Transport at Solid–Liquid Interfaces. *J. Phys. Chem. C*, 120(5):2814–2821, 2016.

[10] A. Majumdar. Scanning thermal microscopy. *Annu. Rev. Mater. Sci.*, 29(1):505–585, 1999.

[11] S. Gomes, A. Assy, and P.-O. Chapuis. Chapter 9 Scanning Thermal Microscopy. In *Thermometry at the Nanoscale: Techniques and Selected Applications*. The Royal Society of Chemistry, 2016.

[12] L. Shi, D. Li, C. Yu, W. Jang, D. Kim, Z. Yao, P. Kim, and A. Majumdar. Measuring Thermal and Thermoelectric Properties of One-Dimensional Nanostructures Using a Microfabricated Device. *J. Heat Transfer*, 125(5):881–888, 2003.

[13] J.-M. Yang, H. Yang, and L. Lin. Quantum dot nano thermometers reveal heterogeneous local thermogenesis in living cells. *ACS Nano*, 5(6):5067–5071, 2011.

[14] G. Baffou, H. Rigneault, D. Marguet, and L. Jullien. A critique of methods for temperature

imaging in single cells. *Nat. Meth.*, 11(9):899–901, 2014.

[15] K. Okabe, N. Inada, C. Gota, Y. Harada, T. Funatsu, and S. Uchiyama. Intracellular temperature mapping with a fluorescent polymeric thermometer and fluorescence lifetime imaging microscopy. *Nat. Commun.*, 3:705, 2012.

[16] C. Wang, R. Xu, W. Tian, X. Jiang, Z. Cui, M. Wang, H. Sun, K. Fang, and N. Gu. Determining intracellular temperature at single-cell level by a novel thermocouple method. *Cell. Res.*, 21(10):1517–1519, 2011.

[17] A. Henry and G. Chen. High Thermal Conductivity of Single Polyethylene Chains Using Molecular Dynamics Simulations. *Phys. Rev. Lett.*, 101(23):235502, 2008.

[18] A. S. Luyt, J. A. Molefi, and H. Krump. Thermal, mechanical and electrical properties of copper powder filled low-density and linear low-density polyethylene composites. *Polym. Degrad. Stabil.*, 91(7):1629–1636, 2006.

[19] S. Shen, A. Henry, J. Tong, R. Zheng, and G. Chen. Polyethylene nanofibres with very high thermal conductivities. *Nat. Nanotechnol.*, 5(4):251–255, 2010.

[20] T. Zhang and T. Luo. Role of Chain Morphology and Stiffness in Thermal Conductivity of Amorphous Polymers. *J. Phys. Chem. B*, 120(4):803–812, 2016.

[21] W. Kossack, A. Seidlitz, T. Thurn-Albrecht, and F. Kremer. Interface and Confinement Induced Order and Orientation in Thin Films of Poly(ε-caprolactone). *Macromolecules*, 49(9):3442–3451, 2016.

[22] J. Liu and R. Yang. Tuning the thermal conductivity of polymers with mechanical strains. *Phys. Rev. B*, 81(17):174122, 2010.

[23] S. Yu, S. Yang, and M. Cho. Analysis of thermal conductivity of polymeric nanocomposites under mechanical loading. *J. Appl. Phys.*, 114(21):213503, 2013.

[24] T. Giesa, M. Arslan, N. M. Pugno, and M. J. Buehler. Nanoconfinement of Spider Silk Fibrils Begets Superior Strength, Extensibility, and Toughness. *Nano Lett.*, 11(11):5038–5046, 2011.

[25] D. Schneider, N. Gomopoulos, C. Y. Koh, P. Papadopoulos, F. Kremer, E. L. Thomas, and G. Fytas. Nonlinear control of high-frequency phonons in spider silk. *Nat. Mater.*, 15(10):1079–1083, 2016.

[26] M. Selmke, M. Braun, and F. Cichos. Photothermal Single-Particle Microscopy: Detection of a Nanolens. *ACS Nano*, 6(3):2741–2749, 2012.

[27] M. Selmke, M. Braun, and F. Cichos. Nano-lens diffraction around a single heated nano particle. *Opt. Express*, 20(7):8055–8070, 2012.

[28] M. Selmke, M. Braun, and F. Cichos. Gaussian beam photothermal single particle microscopy. *J. Opt. Soc. Am. A*, 29(10):2237–2241, 2012.

[29] M. Selmke and F. Cichos. Photonic Rutherford scattering: A classical and quantum mechanical analogy in ray and wave optics. *Am. J. Phys.*, 81(6):405–413, 2013.

[30] M. Selmke and F. Cichos. Photothermal Single Particle Rutherford Scattering Microscopy. *Phys. Rev. Lett.*, 110(10):103901, 2013.

[31] A. Gaiduk, M. Yorulmaz, P. V. Ruijgrok, and M. Orrit. Room-Temperature Detection of a Single Molecule's Absorption by Photothermal Contrast. *Science*, 330(6002):353–356, 2010.

[32] L. Hou, S. Adhikari, Y. Tian, I. G. Scheblykin, and M. Orrit. Absorption and Quantum Yield of Single Conjugated Polymer Poly[2-methoxy-5-(2-ethylhexyloxy)-1,4-phenylenevinylene] (MEH-PPV) Molecules. *Nano Lett.*, 17(3):1575–1581, 2017.

[33] S. Berciaud, L. Cognet, and B. Lounis. Photothermal Absorption Spectroscopy of Individual Semiconductor Nanocrystals. *Nano Lett.*, 5(11):2160–2163, 2005.

[34] S. Berciaud, L. Cognet, and B. Lounis. Luminescence Decay and the Absorption Cross Section of Individual Single-Walled Carbon Nanotubes. *Phys. Rev. Lett.*, 101(7):077402, 2008.

[35] W.-S. Chang, B. A. Willingham, L. S. Slaughter, B. P. Khanal, L. Vigderman, E. R. Zubarev, and S. Link. Low absorption losses of strongly coupled surface plasmons in nanoparticle assemblies. *Proc. Natl. Acad. Sci. USA*, 108(50):19879–19884, 2011.

[36] S. Berciaud, L. Cognet, Philippe Tamarat, and B. Lounis. Observation of Intrinsic Size Effects in the Optical Response of Individual Gold Nanoparticles. *Nano Lett.*, 5(3):515–518, 2005.

[37] M. A. van Dijk, A. L. Tchebotareva, M. Orrit, M. Lippitz, S. Berciaud, D. Lasne, L. Cognet, and B. Lounis. Absorption and scattering microscopy of single metal nanoparticles. *Phys. Chem. Chem. Phys.*, 8(30):3486–3495, 2006.

[38] S. Berciaud, L. Cognet, Philippe Poulin, R. Bruce Weisman, and B. Lounis. Absorption Spectroscopy of Individual Single-Walled Carbon Nanotubes. *Nano Lett.*, 7(5):1203–1207, 2007.

[39] M. Yorulmaz, S. Nizzero, A. Hoggard, L.-Y. Wang, Y.-Y. Cai, M.-N. Su, W.-S. Chang, and S. Link. Single-Particle Absorption Spectroscopy by Photothermal Contrast. *Nano Lett.*, 15(5):3041–3047, 2015.

[40] L. Cognet, C. Tardin, D. Boyer, D. Choquet, P. Tamarat, and B. Lounis. Single metallic nanoparticle imaging for protein detection in cells. *Proc. Natl. Acad. Sci. USA*, 100(20):11350–11355, 2003.

[41] C. Leduc, S. Si, J. Gautier, M. Soto-Ribeiro, B. Wehrle-Haller, A. Gautreau, G. Giannone, L. Cognet, and B. Lounis. A Highly Specific Gold Nanoprobe for Live-Cell Single-Molecule Imaging. *Nano Lett.*, 13(4):1489–1494, 2013.

[42] D. Lasne, G. A. Blab, S. Berciaud, M. Heine, L. Groc, D. Choquet, L. Cognet, and B. Lounis. Single Nanoparticle Photothermal Tracking (SNaPT) of 5-nm Gold Beads in Live Cells. *Biophys. J.*, 91(12):4598–4604, 2006.

[43] D. Boyer, P. Tamarat, A. Maali, B. Lounis, and M. Orrit. Photothermal Imaging of Nanometer-Sized Metal Particles Among Scatterers. *Science*, 297(5584):1160–1163, 2002.

[44] R. Radünz, D. Rings, K. Kroy, and F. Cichos. Hot Brownian Particles and Photothermal Correlation Spectroscopy. *J. Phys. Chem. A*, 113(9):1674–1677, 2009.

[45] P. M. R. Paulo, A. Gaiduk, F. Kulzer, S. F. G. Krens, H. P. Spaink, T. Schmidt, and M. Orrit. Photothermal Correlation Spectroscopy of Gold Nanoparticles in Solution. *J. Phys. Chem. C*, 113(27):11451–11457, 2009.

[46] V. Octeau, L. Cognet, L. Duchesne, D. Lasne, N. Schaeffer, D. G. Fernig, and B. Lounis. Photothermal Absorption Correlation Spectroscopy. *ACS Nano*, 3(2):345–350, 2009.

[47] D. Rings, R. Schachoff, M. Selmke, F. Cichos, and K. Kroy. Hot Brownian Motion. *Phys. Rev. Lett.*, 105(9):090604, 2010.

[48] M. Selmke, R. Schachoff, M. Braun, and F. Cichos. Twin-focus photothermal correlation spectroscopy. *RSC Adv.*, 3(2):394–400, 2013.

[49] P. Zhao, N. Li, and D. Astruc. State of the art in gold nanoparticle synthesis. *Coord. Chem. Rev.*, 257(3–4):638 – 665, 2013.

[50] F. Schulz, T. Homolka, N. G. Bastús, V. Puntes, H. Weller, and T. Vossmeyer. Little Adjustments Significantly Improve the Turkevich Synthesis of Gold Nanoparticles. *Langmuir*, 30(35):10779–10784, 2014.

[51] Kenji Setoura, Daniel Werner, and Shuichi Hashimoto. Optical scattering spectral thermometry and refractometry of a single gold nanoparticle under cw laser excitation. *J. Phys. Chem. C*, 116(29):15458–15466, 2012.

[52] K. Setoura, Y. Okada, D. Werner, and S. Hashimoto. Observation of Nanoscale Cooling Effects by Substrates and the Surrounding Media for Single Gold Nanoparticles under CW-Laser Illumination. *ACS Nano*, 7(9):7874–7885, 2013.

[53] S. Berciaud, L. Cognet, G. A. Blab, and B. Lounis. Photothermal Heterodyne Imaging of Individual Nonfluorescent Nanoclusters and Nanocrystals. *Phys. Rev. Lett.*, 93(25):257402, 2004.

[54] S. Berciaud, D. Lasne, G. A. Blab, L. Cognet, and B. Lounis. Photothermal heterodyne imaging of individual metallic nanoparticles: Theory versus experiment. *Phys. Rev. B*, 73(4):045424, 2006.

[55] S. A. Maier. *Plasmonics: Fundamentals and Applications*. Springer Science & Business Media, 2007.

[56] U. Kreibig and M. Vollmer. *Optical properties of metal clusters*, volume 25. Springer Science & Business Media, 1995.

[57] A. Vial, A.-S. Grimault, D. Macías, D. Barchiesi, and M. L. de la Chapelle. Improved analytical fit of gold dispersion: Application to the modeling of extinction spectra with a finite-difference time-domain method. *Phys. Rev. B*, 71(8):085416, 2005.

[58] R. L. Olmon, B. Slovick, T. W. Johnson, D. Shelton, S.-H. Oh, G. D. Boreman, and M. B. Raschke. Optical dielectric function of gold. *Phys. Rev. B*, 86(23):235147, 2012.

[59] P. B. Johnson and R. W. Christy. Optical Constants of the Noble Metals. *Phys. Rev. B*, 6(12):4370–4379, 1972.

[60] L. B. Scaffardi and J. O. Tocho. Size dependence of refractive index of gold nanoparticles. *Nanotechnology*, 17(5):1309–1315, 2006.

[61] X. Wang, K.-P. Chen, M. Zhao, and D. D. Nolte. Refractive index and dielectric constant evolution of ultra-thin gold from clusters to films. *Opt. Express*, 18(24):24859–24867, 2010.

[62] V. Juvé, M. F. Cardinal, A. Lombardi, A. Crut, P. Maioli, J. Pérez-Juste, L. M. Liz-Marzán, N. Del Fatti, and F. Vallée. Size-Dependent Surface Plasmon Resonance Broadening in Nonspherical Nanoparticles: Single Gold Nanorods. *Nano Lett.*, 13(5):2234–2240, 2013.

[63] M. M. Alvarez, J. T. Khoury, T. G. Schaaff, M. N. Shafigullin, I. Vezmar, and R. L. Whetten. Optical Absorption Spectra of Nanocrystal Gold Molecules. *J. Phys. Chem. B*, 101(19):3706–3712, 1997.

[64] C. F. Bohren and D. R. Huffman. *Absorption and Scattering of Light by Small Particles*. John Wiley & Sons, 1983.

[65] S. Tretyakov. Maximizing Absorption and Scattering by Dipole Particles. *Plasmonics*, 9(4):935–944, 2014.

[66] D. J. Griffith. *Introduction to Electrodynamics*. Pearson, 2013.

[67] K. Lindfors, T. Kalkbrenner, P. Stoller, and V. Sandoghdar. Detection and Spectroscopy of Gold Nanoparticles Using Supercontinuum White Light Confocal Microscopy. *Phys. Rev. Lett.*, 93(3):037401, 2004.

[68] D. Cole, G. Young, A. Weigel, A. Sebesta, and P. Kukura. Label-Free Single-Molecule Imaging with Numerical-Aperture-Shaped Interferometric Scattering Microscopy. *ACS Phot.*, 4(2):211–216, 2017.

[69] P. Kukura, H. Ewers, C. Muller, A. Renn, A. Helenius, and V. Sandoghdar. High-speed nanoscopic tracking of the position and orientation of a single virus. *Nat. Meth.*, 6(12):923–927, 2009.

[70] M. Piliarik and V. Sandoghdar. Direct optical sensing of single unlabelled proteins and super-resolution imaging of their binding sites. *Nat. Commun.*, 5:4495, 2014.

[71] M. Liebel, J. T. Hugall, and N. F. van Hulst. Ultrasensitive Label-Free Nanosensing and High-Speed Tracking of Single Proteins. *Nano Lett.*, 17(2):1277–1281, 2017.

[72] G. V. Hartland. Optical Studies of Dynamics in Noble Metal Nanostructures. *Chem. Rev.*, 111(6):3858–3887, 2011.

[73] V. Myroshnychenko, J. Rodriguez-Fernandez, I. Pastoriza-Santos, A. M. Funston, C. Novo, P. Mulvaney, L. M. Liz-Marzan, and F. J. Garcia de Abajo. Modelling the optical response of gold nanoparticles. *Chem. Soc. Rev.*, 37(9):1792–1805, 2008.

[74] G. Gouesbet and G. Gréhan. *Generalized Lorenz-Mie Theories*. Springer, 2017.

[75] G. Gouesbet, J. A. Lock, and G. Gréhan. Generalized Lorenz–Mie theories and description of electromagnetic arbitrary shaped beams: Localized approximations and localized beam models, a review. *J. Quant. Spec. & Radia. Transfer*, 112(1):1–27, 2011.

[76] S. Link and M. A. El-Sayed. Spectral Properties and Relaxation Dynamics of Surface Plasmon Electronic Oscillations in Gold and Silver Nanodots and Nanorods. *J. Phys. Chem. B*, 103(40):8410–8426, 1999.

[77] A. L. Tchebotareva, P. V. Ruijgrok, P. Zijlstra, and M. Orrit. Probing the acoustic vibrations of single metal nanoparticles by ultrashort laser pulses. *Laser. Photon. Rev.*, 4(5):581–597, 2010.

[78] P. V. Ruijgrok, P. Zijlstra, A. L. Tchebotareva, and M. Orrit. Damping of Acoustic Vibrations of Single Gold Nanoparticles Optically Trapped in Water. *Nano Lett.*, 12(2):1063–1069, 2012.

[79] C. Kittel. *Introduction to Solid State Physics*. Wiley, 1995.

[80] A. Kupiainen. *New Trends in Mathematical Physics*, chapter On the Derivation of Fourier's Law. Springer, 2009.

[81] C. W. Chang, D. Okawa, H. Garcia, A. Majumdar, and A. Zettl. Breakdown of Fourier's Law in Nanotube Thermal Conductors. *Phys. Rev. Lett.*, 101(7):075903, 2008.

[82] H. Zhang, C. Hua, D. Ding, and A. J. Minnich. Length Dependent Thermal Conductivity

Measurements Yield Phonon Mean Free Path Spectra in Nanostructures. *Sci. Rep.*, 5:9121, 2015.

[83] J. A. Johnson, A. A. Maznev, J. Cuffe, J. K. Eliason, A. J. Minnich, Timothy Kehoe, C. M. Sotomayor-Torres, G. Chen, and Keith A. Nelson. Direct Measurement of Room-Temperature Nondiffusive Thermal Transport Over Micron Distances in a Silicon Membrane. *Phys. Rev. Lett.*, 110(2):025901, 2013.

[84] T.-K. Hsiao, H.-K. Chang, S.-C. Liou, M.-W. Chu, S.-C. Lee, and C.-W. Chang. Observation of room-temperature ballistic thermal conduction persisting over 8.3 μm in SiGe nanowires. *Nat. Nanotechnol.*, 8(7):534–538, 2013.

[85] G. Baffou and H. Rigneault. Femtosecond-pulsed optical heating of gold nanoparticles. *Phys. Rev. B*, 84(3):035415, 2011.

[86] P. Berto, M. S. A. Mohamed, H. Rigneault, and G. Baffou. Time-harmonic optical heating of plasmonic nanoparticles. *Phys. Rev. B*, 90(3):035439, 2014.

[87] J. E. Mark, editor. *Polymer Data Handbook*. Oxford University Press, 1999.

[88] A. Jain and A. J. H. McGaughey. Thermal transport by phonons and electrons in aluminum, silver, and gold from first principles. *Phys. Rev. B*, 93(8):081206, 2016.

[89] Z. Ge, D. G. Cahill, and P. V. Braun. Thermal Conductance of Hydrophilic and Hydrophobic Interfaces. *Phys. Rev. Lett.*, 96(18):186101, 2006.

[90] H. S. Carslaw and J. C. Jaeger. *Conduction of Heat in Solids*. Oxford University Press, 1959.

[91] A. Salazar. Energy propagation of thermal waves. *Eur. J. Phys.*, 27(6):1349–1355, 2006.

[92] R. J. Marczak and M. Denda. Alternative Forms of Fundamental Solutions for 3-D Anisotropic Heat Transfer. *Mecánica Computacional*, 29:5639–5654, 2010.

[93] H. Hu and S. A. Argyropoulos. Mathematical modelling of solidification and melting: a review. *Modell. Simul. Mater. Sci. Eng.*, 4(4):371–396, 1996.

[94] D. Li, Y. Wu, P. Kim, L. Shi, P. Yang, and A. Majumdar. Thermal conductivity of individual silicon nanowires. *Appl. Phys. Lett.*, 83(14):2934–2936, 2003.

[95] D. G. Cahill. Thermal conductivity measurement from 30 to 750 K: the 3ω method. *Rev. Sci. Instrum.*, 61(2):802–808, 1990.

[96] S. Doiron and A. Haché. Time evolution of reflective thermal lenses and measurement of thermal diffusivity in bulk solids. *Appl. Opt.*, 43(21):4250–4253, 2004.

[97] M. Maldovan. Narrow Low-Frequency Spectrum and Heat Management by Thermocrystals. *Phys. Rev. Lett.*, 110(2):025902, 2013.

[98] P. G. De Gennes and J. Prost. *The Physics of Liquid Crystals*. Oxford University Press, 1993.

[99] D. Sharma. Non-isothermal kinetics of melting and nematic to isotropic phase transitions of 5CB liquid crystal. *J. Therm. Anal. Calorim.*, 102(2):627–632, 2010.

[100] S. Ishihara. How far has the molecular alignment of liquid crystals been elucidated? *J. Disp. Technol.*, 1(1):30–40, 2005.

[101] R. G. Horn. Refractive indices and order parameters of two liquid crystals. *J. Phys. France*, 39(1):105–109, 1978.

[102] M. Marinelli, F. Mercuri, U. Zammit, and F. Scudieri. Thermal conductivity and thermal diffusivity of the cyanobiphenyl nCB homologous series. *Phys. Rev. E*, 58(5):5860–5866, 1998.

[103] G. Vertogen and W. H. De Jeu. *Thermotropic LIquid Crystals, Fundamentals*. Springer, 1988.

[104] G. S. Iannacchione and D. Finotello. Specific heat dependence on orientational order at cylindrically confined liquid crystal phase transitions. *Phys. Rev. E*, 50(6):4780–4795, 1994.

[105] C. G. A. Hoelen and F. F. M. de Mul. A new theoretical approach to photoacoustic signal generation. *J. Acoust. Soc. Am.*, 106(2):695–706, 1999.

[106] S. E. Bialkowsky. *Photothermal Spectroscopy Methods for Chemical Analysis*. Wiley, 1995.

[107] X. Yang, E. W. Stein, S. Ashkenazi, and L. V. Wang. Nanoparticles for photoacoustic imaging. *Wiley Interdiscip. Rev. Nanomed. Nanobiotechnol.*, 1(4):360–368, 2009.

[108] A. Gaiduk, P. V. Ruijgrok, M. Yorulmaz, and M. Orrit. Detection limits in photothermal microscopy. *Chem. Sci.*, 1(3):343–350, 2010.

[109] J. P. Gordon, R. C. C. Leite, R. S. Moore, S. P. S. Porto, and J. R. Whinnery. Long-Transient Effects in Lasers with Inserted Liquid Samples. *J. Appl. Phys.*, 36(1):3–8, 1965.

[110] S. Chong, W. Min, and X. S. Xie. Ground-State Depletion Microscopy: Detection Sensitivity of Single-Molecule Optical Absorption at Room Temperature. *J. Phys. Chem. Lett.*, 1(23):3316–3322, 2010.

[111] P. Kukura, M. Celebrano, A. Renn, and V. Sandoghdar. Single-Molecule Sensitivity in Optical Absorption at Room Temperature. *J. Phys. Chem. Lett.*, 1(23):3323–3327, 2010.

[112] R. Maceiczyk, H. Shimizu, D. Müller, T. Kitamori, and A. deMello. A Photothermal Spectrometer for Fast and Background-Free Detection of Individual Nanoparticles in Flow. *Anal. Chem.*, 89(3):1994–1999, 2017.

[113] N. A. Turko, A. Peled, and N. T. Shaked. Wide-field interferometric phase microscopy with molecular specificity using plasmonic nanoparticles. *J. Biomed. Opt.*, 18(11):111414, 2013.

[114] E. Absil, G. Tessier, M. Gross, M. Atlan, N. Warnasooriya, S. Suck, M. Coppey-Moisan, and D. Fournier. Photothermal heterodyne holography of gold nanoparticles. *Opt. Express*, 18(2):780–786, 2010.

[115] G. Baffou, P. Berto, E. Bermúdez-Ureña, R. Quidant, S. Monneret, J. Polleux, and H. Rigneault. Photoinduced Heating of Nanoparticle Arrays. *ACS Nano*, 7(8):6478–6488, 2013.

[116] M. C. Skala, M. J. Crow, A. Wax, and J. A. Izatt. Photothermal Optical Coherence Tomography of Epidermal Growth Factor Receptor in Live Cells Using Immunotargeted Gold Nanospheres. *Nano Lett.*, 8(10):3461–3467, 2008.

[117] C. Pache, N. L. Bocchio, A. Bouwens, M. Villiger, C. Berclaz, J. Goulley, M. I. Gibson, C. Santschi, and T. Lasser. Fast three-dimensional imaging of gold nanoparticles in living cells with photothermal optical lock-in Optical Coherence Microscopy. *Opt. Express*, 20(19):21385–21399, 2012.

[118] M. Selmke. *Photothermal Single Particle Detection in Theory & Experiments*. PhD thesis, Universität Leipzig, 2013.

[119] M. Selmke and F. Cichos. The physics of the photothermal detection of single absorbing nano-objects: A review. *arXiv:1510.08669*, 2015.

[120] O. Peña and U. Pal. Scattering of electromagnetic radiation by a multilayered sphere. *Comp. Phys. Commun.*, 180(11):2348–2354, 2009.

[121] T. Wriedt. A Review of Elastic Light Scattering Theories. *Part. Part. Syst. Charact.*, 15(2):67–74, 1998.

[122] J. Evans and M. Rosenquist. “F=ma” optics. *Am. J. Phys.*, 54(10):876–883, 1986.

[123] E. S. Koh, J. McDonald, I. B. Tsvetkova, and B. Dragnea. Measurement of Nanoparticle Adlayer Properties by Photothermal Microscopy. *J. Phys. Chem. Lett.*, 6(18):3621–3625, 2015.

[124] P. Zijlstra, P. M. R. Paulo, and M. Orrit. Optical detection of single non-absorbing molecules using the surface plasmon resonance of a gold nanorod. *Nat. Nanotechnol.*, 7(6):379–382, 2012.

[125] W.-S. Chang and S. Link. Enhancing the Sensitivity of Single-Particle Photothermal Imaging with Thermotropic Liquid Crystals. *J. Phys. Chem. Lett.*, 3(10):1393–1399, 2012.

[126] A. N. G. Parra-Vasquez, L. Oudjedi, L. Cognet, and B. Lounis. Nanoscale Thermotropic Phase Transitions Enhancing Photothermal Microscopy Signals. *J. Phys. Chem. Lett.*, 3(10):1400–1403, 2012.

[127] A. Mërtiri, T. Jeys, V. Liberman, M. K. Hong, J. Mertz, H. Altug, and S. Erramilli. Mid-infrared photothermal heterodyne spectroscopy in a liquid crystal using a quantum cascade laser. *Appl. Phys. Lett.*, 101(4):044101, 2012.

[128] A. Mërtiri, H. Altug, M. K. Hong, P. Mehta, J. Mertz, L. D. Ziegler, and S. Erramilli. Nonlinear Midinfrared Photothermal Spectroscopy Using Zharov Splitting and Quantum Cascade Lasers. *ACS Phot.*, 1(8):696–702, 2014.

[129] L. Hou. *Photothermal Studies of Single Molecules and Gold Nanoparticles: Vapor Nanobubbles and Conjugated Polymers*. PhD thesis, Universiteit Leiden, 2016.

[130] T. X. Ding, L. Hou, H. van der Meer, A. P. Alivisatos, and M. Orrit. Hundreds-fold Sensitivity Enhancement of Photothermal Microscopy in Near-Critical Xenon. *J. Phys. Chem. Lett.*, 7(13):2524–2529, 2016.

[131] L. Hou, M. Yorulmaz, N. R. Verhart, and M. Orrit. Explosive Formation and Dynamics of Vapor Nanobubbles around a Continuously Heated Gold Nanosphere. *New J. Phys.*, 17:013050, 2015.

[132] D. A. Nedosekin, E. I. Galanzha, E. Dervishi, A. S. Biris, and V. P. Zharov. Super-Resolution Nonlinear Photothermal Microscopy. *Small*, 10(1):135–142, 2014.

[133] M. L. Meade. *Lock-in amplifiers: principles and applications*. Peter Peregrinus, 1983.

[134] E. Fällman and O. Axner. Design for fully steerable dual-trap optical tweezers. *Appl. Opt.*, 36(10):2107–2113, 1997.

[135] V. Durán, J. Lancis, E. Tajahuerce, and Z. Jaroszewicz. Cell parameter determination of a twisted-nematic liquid crystal display by single-wavelength polarimetry. *J. Appl. Phys.*, 97(4):043101, 2005.

[136] D. G. Cahill, W. K. Ford, K. E. Goodson, G. D. Mahan, A. Majumdar, H. J. Maris, R. Merlin,

and S. R. Phillpot. Nanoscale thermal transport. *J. Appl. Phys.*, 93(2):793–818, 2003.

[137] S. Dilhaire, G. Pernot, G. Calbris, J. M. Rampnoux, and S. Grauby. Heterodyne picosecond thermoreflectance applied to nanoscale thermal metrology. *J. Appl. Phys.*, 110(11):114314, 2011.

[138] O. O. Dada, P. E. Feist, and N. J. Dovichi. Thermal diffusivity imaging with the thermal lens microscope. *Appl. Opt.*, 50(34):6336–6342, 2011.

[139] L. Rodriguez, J. F. Cárdenas-García, and C. Costa Vera. Measurement of thermal diffusivities of silver nanoparticle colloidal suspensions by means of a frequency-resolved thermal lensing approach. *Opt. Lett.*, 39(12):3406–3409, 2014.

[140] M. Iwaki, A. H. Iwane, K. Ikezaki, and T. Yanagida. Local Heat Activation of Single Myosins Based on Optical Trapping of Gold Nanoparticles. *Nano Lett.*, 15(4):2456–2461, 2015.

[141] M. Harada, M. Shibata, T. Kitamori, and T. Sawada. Application of coaxial beam photothermal microscopy to the analysis of a single biological cell in water. *Anal. Chim. Acta*, 299(3):343–347, 1995.

[142] M. Selmke, A. Heber, M. Braun, and F. Cichos. Photothermal single particle microscopy using a single laser beam. *Appl. Phys. Lett.*, 105(2):013511, 2014.

[143] M. Selmke and F. Cichos. Energy Redistribution Signatures in Transmission Microscopy of Rayleigh- and Mie-particles. *J. Opt. Soc. Am. A*, 31(11):2370–2384, 2014.

[144] P. Ben-Abdallah, R. Messina, S.-A. Biehs, M. Tschikin, K. Joulain, and C. Henkel. Heat Superdiffusion in Plasmonic Nanostructure Networks. *Phys. Rev. Lett.*, 111:174301, 2013.

[145] A. Heber, M. Selmke, and F. Cichos. Metal Nanoparticle Based All-Optical Photothermal Light Modulator. *ACS Nano*, 8(2):1893–1898, 2014.

[146] M. Orrit. Single-Molecule Chemistry is More than Superresolved Fluorescence Microscopy. *Angew. Chem. Int. Ed.*, 54(28):8004–8005, 2015.

[147] A. P. Demchenko. *Introduction to Fluorescence Sensing*. Springer Science & Business Media, 2015.

[148] P. Billaud, S. Marhaba, N. Grillet, E. Cottancin, C. Bonnet, J. Lermé, J.-L. Vialle, M. Broyer, and M. Pellarin. Absolute optical extinction measurements of single nano-objects by spatial modulation spectroscopy using a white lamp. *Rev. Sci. Instrum.*, 81(4):043101, 2010.

[149] J. Hwang, M. M. Fejer, and W. E. Moerner. Scanning interferometric microscopy for the detection of ultrasmall phase shifts in condensed matter. *Phys. Rev. A*, 73(2):021802, 2006.

[150] I. Tijunelyte, E. Guenin, N. Lidgi-Guigui, F. Colas, J. Ibrahim, T. Toury, and M. Lamy de la Chapelle. Nanoplasmonics tuned click chemistry. *Nanoscale*, 8(13):7105–7112, 2016.

[151] K. M. Haas and B. J. Lear. Billion-fold rate enhancement of urethane polymerization via the photothermal effect of plasmonic gold nanoparticles. *Chem. Sci.*, 6(11):6462–6467, 2015.

[152] M. Fedoruk, M. Meixner, S. Carretero-Palacios, T. Lohmüller, and J. Feldmann. Nanolithography by Plasmonic Heating and Optical Manipulation of Gold Nanoparticles. *ACS Nano*, 7(9):7648–7653, 2013.

[153] L. Cao, D. N. Barsic, A. R. Guichard, and M. L. Brongersma. Plasmon-Assisted Local Temperature Control to Pattern Individual Semiconductor Nanowires and Carbon Nanotubes. *Nano*

Lett., 7(11):3523–3527, 2007.

[154] N. Tabatabaei, A. Mandelis, and B. T. Amaechi. Thermophotonic radar imaging: An emissivity-normalized modality with advantages over phase lock-in thermography. *Appl. Phys. Lett.*, 98(16):163706, 2011.

[155] B. van Grinsven, K. Eersels, M. Peeters, P. Losada-Pérez, T. Vandenryt, T. J. Cleij, and P. Wagner. The Heat-Transfer Method: A Versatile Low-Cost, Label-Free, Fast, and User-Friendly Readout Platform for Biosensor Applications. *ACS Appl. Mater. Interfaces*, 6(16):13309–13318, 2014.

[156] G. Baffou, P. Bon, J. Savatier, J. Polleux, M. Zhu, M. Merlin, H. Rigneault, and S. Monneret. Thermal Imaging of Nanostructures by Quantitative Optical Phase Analysis. *ACS Nano*, 6(3):2452–2458, 2012.

[157] S. C. Nguyen, Q. Zhang, K. Manthiram, X. Ye, J. P. Lomont, Ch. B. Harris, H. Weller, and A. P. Alivisatos. Study of Heat Transfer Dynamics from Gold Nanorods to the Environment via Time-Resolved Infrared Spectroscopy. *ACS Nano*, 10(2):2144–2151, 2016.

[158] A. Mandelis, L. Nicolaides, and Y. Chen. Structure and the Reflectionless/Refractionless Nature of Parabolic Diffusion-Wave Fields. *Phys. Rev. Lett.*, 87(2):020801, 2001.

[159] B. E. A. Saleh and M. C. Teich. *Fundamental of Photonics*. John Wiley & Sons, 1991.

[160] A. Heber, M. Selmke, and F. Cichos. Thermal diffusivity measured using a single plasmonic nanoparticle. *Phys. Chem. Chem. Phys.*, 17(32):20868–20872, 2015.

[161] A. Fitzgibbon, M. Pilu, and R. B. Fisher. Direct least square fitting of ellipses. *IEEE Trans. Pattern Anal. Mach. Intell.*, 21(5):476–480, 1999.

[162] M. Marklund and J. Lundin. Quantum vacuum experiments using high intensity lasers. *Eur. J. Phys. D*, 55(2):319–326, 2009.

[163] D. Pacifici, H. J. Lezec, and H. A. Atwater. All-optical modulation by plasmonic excitation of CdSe quantum dots. *Nat. Photon.*, 1(7):402–406, 2007.

[164] C. Min, P. Wang, C. Chen, Y. Deng, Y. Lu, H. Ming, T. Ning, Y. Zhou, and G. Yang. All-optical switching in subwavelength metallic grating structure containing nonlinear optical materials. *Opt. Lett.*, 33(8):869–871, 2008.

[165] V. R. Almeida, C. A. Barrios, R. R. Panepucci, and M. Lipson. All-optical control of light on a silicon chip. *Nature*, 431(7012):1081–1084, 2004.

[166] T. Gao, P. S. Eldridge, T. C. H. Liew, S. I. Tsintzos, G. Stavrinidis, G. Deligeorgis, Z. Hatzopoulos, and P. G. Savvidis. Polariton condensate transistor switch. *Phys. Rev. B*, 85(23):235102, 2012.

[167] D. Ballarini, M. De Giorgi, E. Cancellieri, R. Houdré, E. Giacobino, R. Cingolani, A. Bramati, G. Gigli, and D. Sanvitto. All-optical polariton transistor. *Nat. Commun.*, 4:1778, 2013.

[168] J. Hwang, M. Pototschnig, R. Lettow, G. Zumofen, A. Renn, S. Gotzinger, and V. Sandoghdar. A single-molecule optical transistor. *Nature*, 460(7251):76–80, 2009.

[169] S. F. Preble, Q. Xu, B. S. Schmidt, and M. Lipson. Ultrafast all-optical modulation on a silicon chip. *Opt. Lett.*, 30(21):2891–2893, 2005.

[170] I.-C. Khoo. *Liquid Crystals: Physical Properties and Nonlinear Optical Phenomena*, vol-

ume 64. John Wiley & Sons, 2007.

[171] J. Shan, W. Shi, L. Y. Liu, Y. R. Shen, and L. Xu. Optical Control of Surface Anchoring and Reorientation of Liquid Crystals via a Plasmon-Enhanced Local Field. *Phys. Rev. Lett.*, 109(14):147801, 2012.

[172] P. Zijlstra and M. Orrit. Single metal nanoparticles: optical detection, spectroscopy and applications. *Rep. Prog. Phys.*, 74(10):106401, 2011.

[173] G. Baffou, R. Quidant, and C. Girard. Thermoplasmonics modeling: A Green's function approach. *Phys. Rev. B*, 82(16):165424, 2010.

[174] A. Govorov, W. Zhang, T. Skeini, H. Richardson, J. Lee, and N. Kotov. Gold nanoparticle ensembles as heaters and actuators: melting and collective plasmon resonances. *Nanoscale Res. Lett.*, 1(1):84–90, 2006.

[175] X. Xie, K. Yang, D. Li, T.-H. Tsai, J. Shin, P. V. Braun, and D. G. Cahill. High and low thermal conductivity of amorphous macromolecules. *Phys. Rev. B*, 95(3):035406, 2017.

[176] J. Miyazaki, H. Tsurui, K. Kawasumi, and T. Kobayashi. Sensitivity enhancement of photothermal microscopy with radially segmented balanced detection. *Opt. Lett.*, 40(4):479–482, 2015.

[177] M. J. Booth, M. A. A. Neil, R. Juškaitis, and T. Wilson. Adaptive aberration correction in a confocal microscope. *Proc. Natl. Acad. Sci. USA*, 99(9):5788–5792, 2002.

[178] M. J. Booth. Wavefront sensorless adaptive optics for large aberrations. *Opt. Lett.*, 32(1):5–7, 2007.

[179] C. Starr. The Copper Oxide Rectifier. *J. Appl. Phys.*, 7(1):15–19, 1936.

[180] A. Heber, M. Selmke, and F. Cichos. Thermal Diffusivities Studied by Single Particle Photothermal Deflection Microscopy. *ACS Phot.*, 4(3):681–687, 2017.